Modélisation numérique de l'endommagement dans les matériaux nanostructurés obtenus par déformation plastique sévère

Pouya Tajdary

HESAM UNIVERSITÉ

Arts et Métiers Sciences et Technologies

ÉCOLE DOCTORALE SCIENCES ET MÉTIERS DE L'INGÉNIEUR
Laboratoire PIMM - Campus de Paris

THÈSE

présentée par : **Pouya TAJDARY**
soutenue : **19 septembre 2022**

pour obtenir le grade de : **Docteur d'HESAM Université**

préparée à : **École Nationale Supérieure d'Arts et Métiers**

Spécialité : **Génie mécanique et matériaux**

Numerical simulation of damage in nanostructured materials obtained by severe plastic deformation

THÈSE dirigée par :
M. Chedly BRAHAM

et co-encadrée par :
M. Léo MORIN

Jury

M. Jean-Baptiste LEBLOND	Professeur, Sorbonne Université	Président
M. Andrzej BACZMAŃSKI	Professor, AGH UST	Rapporteur
M. Manuel FRANCOIS	Professeur, UTT	Rapporteur
M. Gonzalo GONZALEZ	Professor, UNAM	Examinateur
M. Joseph PAUX	Maître de Conférences, URCA	Examinateur
M. Chedly BRAHAM	Maître de Conférences HDR, ENSAM	Examinateur
M. Léo MORIN	Maître de Conférences, CNAM	Examinateur

THÈSE

ACKNOWLEDGMENTS

Finishing my thesis wouldn't be possible without the remarkable guidance and precious advises of my directors Chedly Braham and Léo Morin. Léo particularly for his splendid enthusiasm in research, his commitment in work and his patience with me. Not to forget his generous kindness and his unique charisma ! Having him in this project was reassuring for me as I knew who to turn to when I was stuck with numerical or modelling problems. And I thank Chedly for his unselfish sharing of his vast experience with me. With Léo, we were constantly amazed by the way Chedly could find solutions for the problems we were facing ; usualy by looking from outside the box and giving simple but very efficient ideas that certainly come from his great insight developed in many years. I hugely profited from his knowledge in material science and experimentation during this project. I thank both of them greatly and I owe them my success.

This work includes some collaborations between Ecole Nationale d'Arts et Métiers ParisTech and Universidad Nacional Autónoma de México. In particular, the experimental campaign related to material preparation, performing RCS process and corresponding tensile tests have been performed by colleagues from UNAM (PAPIIT IN102321 project). In this context, I would like to acknowledge the contribution from Pr. Gonzalo Gonzalez (and his students) and I thank him for his great work and also for the discussions we've had about this project.

Additionally, fruitful discussions with Dirk Mohr and Maysam B. Gorji of ETH Zurich on the deep drawing experiments they performed are deeply appreciated. I particularly thank Dr. Gorji for providing data from their experiments and simulations.

Sharing one's work with his colleagues and other members of the scientific community is a privilege. It was a great pleasure for me to have the opportunity to have my PhD thesis read and analysed by the members of the jury of my thesis. They are the experts of the different scientific domains that I worked on during my thesis and it was a great honor to have their exhaustive opinion on my work and

to be given my diploma by them. Here I warmly thank Pr. Andrzej Baczmański, Pr. Manuel François, Pr. Gonzalo Gonzalez, Pr. Jean-baptiste Leblond and Dr. Joseph Paux.

My mother Kianoosh, my father Khosro and my sister Pariya have always supported me no matter what and they have been there for me in every important point of my life and I thank them greatly for that. Also it was a pleasure and great joy to have my girlfriend Eulalie beside me in this challenge. She was the comfort I needed during the tough moments.

I spent 3 great years in PIMM laboratory and I enjoyed having worked with great people. I felt welcome there and I made amazing friends. I won't forget our Friday nights and all our adventures together. I particularly cherish and thank all members of the Manet building and specially my dearest friends Lucas, Antoine and Sidonie.

ABSTRACT

Nanostructured materials obtained notably through severe plastic deformation (SPD), alternatively called bulk ultrafine grained materials (UFG), are an emerging class of advanced materials that bring new possibilities in terms of functional and structural properties by combining high strength and ductility. The combination of ultrafine grain size and high dislocation densities permits to improve paradoxically both the strength and the ductility in metals, in contrast with conventional forming methods such as rolling or drawing. Materials obtained by intense plastic deformation processing thus appear very attractive for advanced structural applications. Simulation of SPD process is quite challenging as it involves excessive plastic deformation and nonlinearity due to contact conditions. Many studies have been done on modelling the intensive plastic deformation during SPD processes. However, an important aspect of these processes, namely, damage is generally neglected. Many physical and phenomenological damage models have been developed but none have been implemented in a severe case such of SPD processes. In this thesis, we try to implement recent microstructural models based on dislocation density evolution in SPD processes and by implementing damage evolution laws during the simulation of these processes. A computational framework will be developed in order to predict the evolution of microstructure and damage during SPD. This permits to improve the understanding of strength-ductility trade-off in SPD and optimize the processing conditions in order to minimize the damage and enhance the properties of the processed material.

RÉSUMÉ

Les matériaux nanostructurés obtenus notamment par déformation plastique sévère (SPD), également appelés matériaux à grains ultrafins, constituent une classe émergente de matériaux avancés qui offrent de nouvelles possibilités en termes de propriétés fonctionnelles et structurelles en combinant résistance et ductilité élevées. La combinaison d'une taille de grain ultrafine et de densités de dislocations élevées permet d'améliorer paradoxalement à la fois la résistance et la ductilité des métaux, contrairement aux méthodes de formage conventionnelles telles que le laminage ou l'étirage. Les matériaux obtenus par un processus de déformation plastique sévère semblent donc très intéressants pour les applications structurelles avancées. La simulation du processus SPD est assez difficile car cela implique des déformations plastiques importantes et des non-linéarités liées aux conditions de contact. De nombreuses études ont été réalisées sur la modélisation des processus SPD. Néanmoins, l'endommagement, qui un aspect important dans ces procédés, est généralement non pris en compte. De nombreux modèles d'endommagement physiques et phénoménologiques ont été développés mais aucun n'a été implémenté dans un cas sévère tel que les processus SPD. Dans cette thèse, nous essayons d'implémenter des modèles microstructuraux récents basés sur l'évolution de densités de dislocations dans les processus SPD et en implémentant des lois d'évolution de l'endommagement pendant la simulation de ces processus. Un cadre de calcul sera développé afin de prédire l'évolution de la microstructure et de l'endommagement pendant les procédés SPD. Cela permet d'améliorer la compréhension du compromis résistance-ductilité dans les procédés SPD et d'optimiser les conditions de traitement afin de minimiser l'endommagement et d'améliorer les propriétés du matériau traité.

Table of Contents

List of Tables

List of Figures

INTRODUCTION

The need for enhanced materials is an important axis of research in the industry. “Better” materials mean lighter structures that are more resistant to failure in a variety of environments. Moreover, the use of advanced lightweight materials can lead to important decrease in fuel consumption and has an impact to carbon emission reduction. Additionally, improving the functionality and life span of materials and facilitation of their recycling, would further help conserve the nature by decreasing waste and manufacturing energy.

Scientists have always challenged themselves to improve the properties of materials, or come up with new materials that have advantageous properties. Since the industrial revolution, metals and alloys were greatly used in the industry. Researchers have continuously tried to develop advanced alloys for various applications. In order to achieve this goal, enriched knowledge of the fundamentals of metallurgy and material microstructure is needed. Scientific advances in material science and engineering and development of advanced microscopic methods have opened new horizons to the understanding of the microstructure of materials and the mechanisms that control their deformation. Many phenomenological and physical theories enable us to predict the behavior of materials under different conditions. All these advances have helped accelerate development of new materials and optimisation of industrial processes, leading to cutting edge applications that were not possible without these new properties. From lightweight strong implants that are compatible with human body to parts used in space rockets that withstand great pressure and high temperature, all are made of advanced metals that are possible due to advances in our understanding of their microstructure and behaviour.

Metals are in everlasting contradiction in terms of ductility and strength. Ductility enables a material to deform and take the desired shape without occurrence of failure. Reasonably, ductile materials tend to be less strong and once used in an structure, they won’t have the necessary strength and resistance to avoid deformation and this would lead to the failure depending on the application.

This trade-off between strength and ductility has been an issue with material development research since forever!

To oppose this trade-off (have more ductility and more strength at the same time), researchers developed many different approaches which generally concern modification of the microstructure of the metals. In pure metals and alloys, these approaches include: cold working, solution and precipitation hardening, transformation hardening, etc. These approaches aim at increasing the strength of the material but usually lead to a decrease in ductility.

Lately, new approaches have been introduced to further oppose the strength-ductility trade-off. Advanced understanding of microstructural mechanism has led to the manufacturing of materials with much better properties. Two examples of these materials are Transformation Induced Plasticity (TRIP) and Twinning Induced Plasticity (TWIP) steels that have very interesting properties in terms of both ductility and strength. Another important advancement in material properties that is also the topic of this project, is the manufacturing of nanostructured materials. These materials have incredible properties that lead to numerous applications in transport, aeronautics, energy and bio-mechanical sectors. The ultrafine grain structure present in these materials has led to very high strength without much sacrificing the ductility.

Currently two approaches exist in fabrication of these nanostructured materials. The first one is the so-called bottom-top approach, in which polycrystals are assembled using for instance atom deposition or inter gas condensation; this leads to very small samples usually containing too much porosity. The second approach is a top-down approach in which severe plastic deformation (SPD) is applied to bulk coarse grained materials, leading to important grain refinement without changing the initial configuration. Hence the possibility to repeat each pass several times allows achieving more grain refinement. Several SPD processes exist and each concern a particular sample shape. Recently, new SPD processes have been developed that produces nanostructured sheet metals with interesting properties that can be used in automobile and aeronautic sectors.

Despite the development of numerous SPD techniques, these processes however, have not yet been commercialised and exist only at a laboratory scale. More investigations should yet be made in order to increase the size of processed samples and the speed of productions, in order to industrialize the SPD processes. One important challenge for achieving this goal is the optimisation of the SPD processes. Recent advances in computational mechanics has led to vast application of mechanical simulations in

research. Consequently, nowadays process optimisation techniques are performed in the framework of numerical simulation in order to reduce material and equipment costs. Optimisation of these processes requires several components:

- A modelling of the material behavior based on the physical mechanics at the microscale is necessary to predict the overall mechanical properties.
- A computational framework that could perform simulation of SPD processes and permits the prediction of material properties and possible degradation of materials.

Firstly, advanced material constitutive laws should be developed and implemented in order to evaluate the material behavior during SPD processes. Indeed, since several passes of a SPD process could lead to plastic strain of order 10, a proper simulation of this behavior would require implementing a suitable material model. Secondly, it has been observed that damage and degradation could happen during SPD processes. Indeed in order to optimise the material properties, a maximum number of SPD passes should be performed without damaging the material. As a result, a relevant simulation of these processes should also take into account degradation of the material during each pass.

Last but not least, research has shown that the materials obtained by SPD processes exhibit excellent strength and superplasticity. Interestingly, in some cases, increasing the number of passes of SPD leads to an increase in both ductility and strength. These properties are in direct contradiction to the previously mentioned strength ductility trade-off. As a material's performance is tied to hardening and softening mechanisms in the microstructure, a proper modelling of these mechanisms could lead to a better understanding of this strength ductility paradox. As a result, a combination of hardening and softening behaviors tied to grain refinement, dislocation density evolution and damage, could enhance the understanding of nanostructured materials obtained by SPD.

The present thesis aims to tackle the issue of the simulation of SPD and analyse the evolution of microstructure as well as ductile damage in these processes, in order to improve the understanding of the material behavior, and create a framework for optimisation of these processes by reducing damage and fracture. This thesis is organized in four chapters:

- In Chapter 1, a bibliography review is presented. This chapter summarizes the basics of (i) severe plastic deformation processing, (ii) dislocation-based plasticity model for grain refinement and

(iii) ductile damage modelling.

- In Chapter 2, shear ductile damage is investigated in deep-drawing using a micromechanical model including void shape effects. This "conventional plastic deformation process" is first studied in order to assess the ability of the local approach of ductile failure to predict crack initiation in a case of moderate plastic strains.

- In Chapter 3, a case of severe plastic deformation processing, using repetitive corrugation and straightening (RCS), is considered. The evolution of damage and the residual stress distribution are analyzed in two aluminum alloys, for only one pass of the process.

- Finally, several passes of RCS are investigated in Chapter 4. A micromechanical model including ductile damage evolution and dislocation-based hardening modelling is developed. Using this model, numerical tensile tests are performed after the simulation of the RCS process is order to model the strength-ductility modifications induced by the process.

Chapter 1

Bibliography

1.1 Resumé en français

Dans ce chapitre, une revue des travaux qui abordent les sujets traités dans cette thèse est présentée. Un bref historique des sujets qui motivent ce projet est donné pour mieux définir les objectifs et la nouveauté de ce projet, notamment en termes de modélisation du comportement des matériaux. Ce chapitre est organisé de la façon suivante :

Dans la Section 1.3, le traitement par déformation plastique sévère (SPD) est présenté ainsi que certaines applications pertinentes pour ce travail. L'accent est mis sur un processus appelé "corrugation et aplatissement répétitifs" (RCS) qui sera considéré dans cette thèse. Dans la Section 1.4, des travaux récents portant sur la modélisation de l'écrouissage basée sur l'évolution de densités de dislocations sont introduits. En particulier, un modéle phénoménologique d'écrouissage basé sur une structure cellulaire de dislocations sera présenté et sera utilisé dans les simulations de cette thèse afin de définir le comportement des matériaux pendant la SPD. Dans la Section 1.5, nous détaillerons lec mécanismes d'endommagement ductile présents lors de déformations plastiques. De plus, dans cette section, une brève revue des différents modèles d'endommagement ductile sera donnée et un modèle micromécanique basé sur les effets de forme des vides qui est adapté aux processus étudiés dans cette thèse est présenté.

1.1.1 Mise en œuvre des matériaux par déformation plastique sévère

Les matériaux nanostructurés traités par déformation plastique sévère (SPD) présentent un intérêt considérable pour les applications structurelles en raison de leurs propriétés mécaniques améliorées,

notamment une résistance élevée, une bonne ductilité, une grande ténacité et une superplasticité à des taux de déformation élevés et à basse température, contrairement aux matériaux à gros grains qui sont intrinsèquement limités par le compromis résistance-ductilité.

Le traitement par déformation plastique sévère (SPD) correspond à diverses procédures expérimentales de mise en forme des métaux qui ont été développées pour induire une déformation intense et un affinement des grains. Au cours du procédé SPD, le matériau est soumis à une importante déformation plastique sans que sa géométrie initiale ne soit beaucoup modifiée, ce qui permet de lui appliquer plusieurs passes. Malgré les lacunes actuelles en termes d'industrialisation des procédés SPD dues à la petite taille des échantillons, cette méthode est prometteuse pour produire des matériaux nanostructurés pour des applications structurelles. Les procédés SPD les plus courants sont l'ECAP [61], le HTP [18], l'ARB [56] et le RCS [54]. Voir Figure 1.1 pour une représentation schématique de ces procédés.

Dans cette thèse, nous nous concentrons sur le procédé RCS car c'est un procédé de mise en forme très prometteur pour la production de tôles nanostructurées à grande échelle dans un cadre continu et discontinu [54]. Au cours du processus RCS, la pièce est déformée par une matrice ondulée à motifs multiples de forme particulière ; ensuite, une matrice plate déforme le matériau pour lui redonner sa forme initiale. Chaque passe du procédé RCS conduit à une déformation plastique importante. De nombreuses études sur l'aluminium pur [100, 109], les alliages d'aluminium [17, 29, 35, 49, 82], cuivre [117] et alliages de magnésium [93] ont montré une augmentation significative de la résistance mecanique du matériau après chaque passage du processus. Cette tendance se poursuit généralement jusqu'à ce que le matériau se dégrade par différents mécanismes d'endommagement qui sont liés à la croissance des vides à l'intérieur du matériau [44].

L'étude des matériaux traités par SPD est généralement complétée par des simulations numériques du processus. Dans le cas du SPD, ces études numériques permettent (i) de représenter des champs mécaniques qui ne sont pas facilement accessibles par des mesures expérimentales, telles que les distributions 3D des contraintes [49, 93, 100], (ii) d'étudier l'effet des paramètres du procédé tels que la forme des outils [93, 100], et (iii) de fournir des lignes directrices pour optimiser le procédé. Une des lacunes actuelles dans la simulation numérique du RCS est l'absence de mécanismes physiques dans la modélisation des matériaux. En particulier, un couplage entre l'évolution de l'endommagement ductile et les lois de durcissement avancées basées sur les mécanismes physiques de la déformation est nécessaire pour simuler avec précision les changements microstructuraux pendant les procédés SPD.

1.1.2 Modélisation du durcissement basée sur l'évolution de la densité des dislocations

Il est généralement admis dans les matériaux traités par SPD que les dislocations sont le principal mécanisme qui contribue au durcissement. Au cours des procédés SPD, la déformation élevée s'accompagne d'une création et d'un déplacement important de dislocations. Les observations expérimentales montrent que les métaux traités par SPD présentent des zones hétérogènes avec des densités de dislocations très élevées et très faibles ; les dislocations forment des structures cellulaires qui sont composées de parois et d'intérieurs de cellules. Dans cette hypothèse, les parois cellulaires correspondent aux zones à hautes densités de dislocations et l'intérieur des cellules correpond aux zones de plus faibles densités de dislocations. En conséquence, il est admis que les prcédes SPD conduisent à la création d'une "structure composite à deux phases" dans les métaux [86, 99].

Il est intéressant de noter que l'accumulation de dislocations dans les parois cellulaires entraîne une forte désorientation des parois cellulaires qui augmente avec la déformation plastique induite [32]. L'augmentation de la désorientation transforme les parois cellulaires en joint de sous-grains et finalement en joint de grains individuels [65]. Ce mécanisme explique l'importante capacité de affinement des grains par SPD et la formation de grains ultrafins [46, 121].

Plusieurs tentatives ont été faites pour prédire l'écrouissage sur la base des mécanismes de production et d'annihilation des dislocations. La première tentative la plus célèbre celle du modèle à un paramètre développé par Mecking and Kocks [81]. À partir des observations expérimentales de la structure des dislocations dans les métaux, un modèle à deux paramètres a été proposé par Mughrabi [86] sur la base de la description des densités de dislocations dans les parois et les intérieurs des cellules. Dans ce modèle, la structure cellulaire des dislocations est supposée créer un composite de zones à faible et à forte densité de dislocation.

Estrin et al. [33] a étendu l'approche de Mughrabi [86] en dérivant des équations constitutives qui rendent compte de l'évolution des dislocations dans les parois et l'intérieur des cellules. Ce modèle est basé sur l'hypothèse composite de microstructure utilisant deux phases distinctes. Ce modèle a été utilisé avec succès dans plusieurs applications de SPD et de procédés d'usinage et les résultats prédits correspondent très bien aux mesures expérimentales et il permet de tenir compte approximativement du affinement de la taille des grains. [5, 63, 80].

1.1.3 Endommagement ductile

La rupture ductile des métaux est généralement due à la nucléation, à la croissance et à la coalescence successives de micro-vides [13, 15, 97]. La Figure 1.11 montre schématiquement les différentes étapes de l'évolution des dommages dans les métaux.

Si la rupture ductile est généralement pilotée par la triaxialité, des travaux récents ont montré que la rupture ductile peut également survenir en présence de cisaillement [7, 27, 28, 39, 45, 51, 103]. Dans ces cas, la croissance des vides est limitée et l'adoucissement macroscopique est attribué aux changements de forme et d'orientation des vides, notamment l'aplatissement des vides soumis au cisaillement.

La modélisation la plus avancée de la rupture ductile est basée sur l'approche locale, en adoptant une démarche micromécanique. Les modèles dévelopés dans ce contexte sont basés sur une description locale des mécanismes physiques de la rupture ductile, en suivant principalement les travaux précurseurs de Gurson [47]. Ce modèle est composé d'un critère de plasticité macroscopique et d'une règle d'écoulement qui tient compte de la présence de vides par la porosité.

Dans l'ensemble, cette classe de modèles fournit de bonnes prédictions lorsque la triaxialité est élevée et dans ce cas, l'endommagement est principalement dû à la croissance des vides. Cependant, le modèle de Gurson sous-estime l'apparition de l'endommagement en présence de cisaillement. Dans ce travail, une approche alternative pour la simulation de l'endommagement sous chargements complexes (lors de procédés d'emboutissage par exemple) sera considérée, basée sur une description micromécanique de l'effet de la croissance des vides, de la rotation et de l'élongation des vides. En effet, il a été démontré récemment que la rupture ductile sous des charges dominées par le cisaillement est essentiellement due à des changements importants de la forme des vides [84, 91]. Par conséquent, nous nous concentrerons principalement sur le modèle de Madou-Leblond incorporant des effets de forme des vides [73–76], dans lequel les demi-axes et l'orientation des vides peuvent évoluer, afin de simuler la rupture ductile en cisaillement.

1.2 Introduction

In this chapter, a review of the works that address the topics pursued in this thesis is presented. A brief history of the subjects that motivate this project is given to better define the objectives

and novelty of this project, especially in terms of modelling of of material behavior. This chapter is organized as follows:

In the Section 1.3, processing by severe plastic deformation (SPD) is introduced along with some applications that are relevant to this work. At first, a history of SPD processes is given and different processes are introduced. The emphasis is placed on a process called repetitive corrugation and straightening (RCS) which will be considered in this thesis. Moreover, a summary of the experimental characterisation techniques and numerical simulations relevant for SPD processing is presented to illustrate the properties of the final materials obtained by RCS. In Section 1.4, first, a brief description of microstructural evolution during plastic deformation of metals and different stages of strain hardening is presented. Next, the latest investigations in the literature for modelling of the hardening based on dislocation density evolution is introduced. Later, a phenomenological model based on cellular structure of dislocations will be presented that will be used in the simulations of this thesis in order to define the hardening behavior of materials during SPD. In Section 1.5, analytical and experimental investigations that have been developed in the literature to understand the underlying mechanisms of ductile damage and predict its evolution will be discussed. Also in this section, a brief review of different ductile damage models is given and a micromechanical model based on void shape effects that is suitable for the processes studied in this thesis is presented.

1.3 Processing by severe plastic deformation

1.3.1 Introduction

Nanostructured materials processed by severe plastic deformation (SPD) are of considerable interest in structural applications because of their improved mechanical properties including high strength, good ductility, high toughness, and superplasticity at high strain rates and low temperatures, in contrast with coarse-grained materials which are limited by the strength-ductility trade-off [2, 127].

Processing by severe plastic deformation (SPD) refers to various experimental procedures of metal forming that have been developed to induce intense straining and grain refinement. During SPD process, the material is subjected to significant plastic deformation without much change in its initial geometry and thus allowing several passes to be applied on it. Despite current shortcomings in industrialization of the SPD processes due to small size of samples, this is a promising way of pro-

ducing nanostructured materials for structural applications [55]. The most common SPD processes are equal channel angular pressing (ECAP) [61], high torsion pressing (HTP) [18], accumulative roll bonding (ARB) [56] and repetitive corrugation and straightening (RCS)[1] [54]. Each of these processes requires a specific workpiece; ECAP concerns rectangular or cylindrical bars, HTP deals with flat disk specimen while ARB and RCS are suitable for producing sheet metals. See Figure 1.1 for schematic representation of these processes.

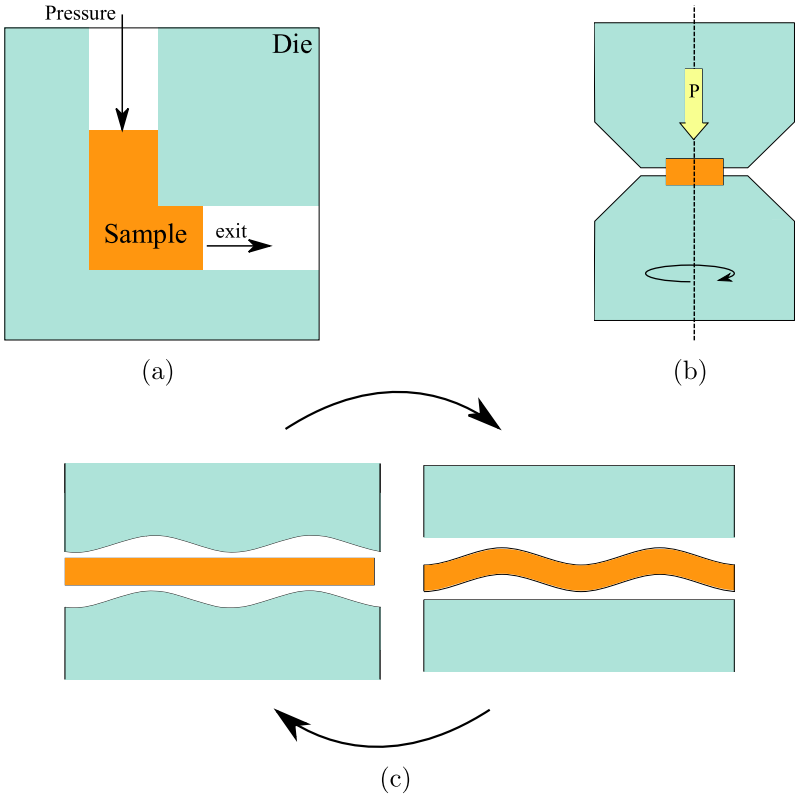

Figure 1.1: Examples of processing by SPD: (a) Equal channel angular pressing (ECAP), (b) High torsion pressing (HTP) and (c) Repetitive corrugation and straightening (RCS).

Processing by SPD leads to significant evolution of microstructure. The evolution starts with apparition of cellular structure of dislocation and high dislocation density walls are formed (see Figure 1.2 for images taken by transmission electron microscope (TEM) of dislocation cell structure). As plastic deformation increases, cell walls become subgrain boundaries and later during severe plastic deformation, high-angle grain boundaries.

[1]RCS encompasses several processing techniques including Constrained Groove Pressing (CGP) [108] and Constrained Studded Pressing (CSP) [117].

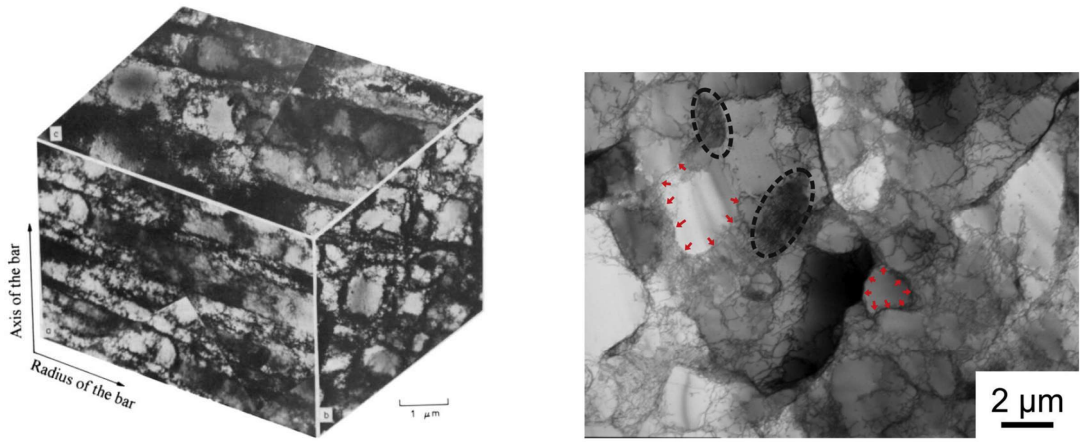

(a) (b)

Figure 1.2: (a) 3D TEM image of the structure of dislocations after severe torsion of copper sample [124] and (b) TEM image of highly pure Al showing dislocation cell structure and some cell walls are shown by red arrows [22].

Figure 1.3 schematically represents this evolution which leads to grain refinement. In Figure 1.4, maps of local crystal structure and orientation of the initial and processed microstructure of high purity aluminium by electron backscatter diffraction (EBSD) technique is shown. After 8 passes of ECAP, the initially coarse grains are refined to submicron dimensions. This huge grain refinement leads to very particular properties in materials processed by SPD. For example in Figure 1.5a, the stress-strain curves of SUS 316L samples extracted from the bulk material processed by several passes of ECAP is presented. According to this figure, increasing the number of passes has led to very important enhancement of material strength. Similar enhancement is observed in Figure 1.5b, where Wohler curve of a material processed by ECAP shows improvement of fatigue limit.

1.3.2 Repetitive Corrugation and Straightening

In this thesis, we focus on RCS because it is a very promising metal forming process for production of large-scale nanostructured *sheet metals* in a continuous and discontinuous setting [54]. During RCS process, the workpiece is deformed by a multi-pattern corrugation die of particular shape; then, a straightening die deforms the material to almost its initial shape. Each pass of RCS leads to important plastic deformation and the heterogeneity and severity of the deformation are a function of the shape of the patterns in the multi-pattern corrugation die (an example of a multi-pattern corrugation die is given in Figure 1.6). Numerous studies on pure aluminum [100, 109], aluminum alloys [17, 29, 35, 49, 82],

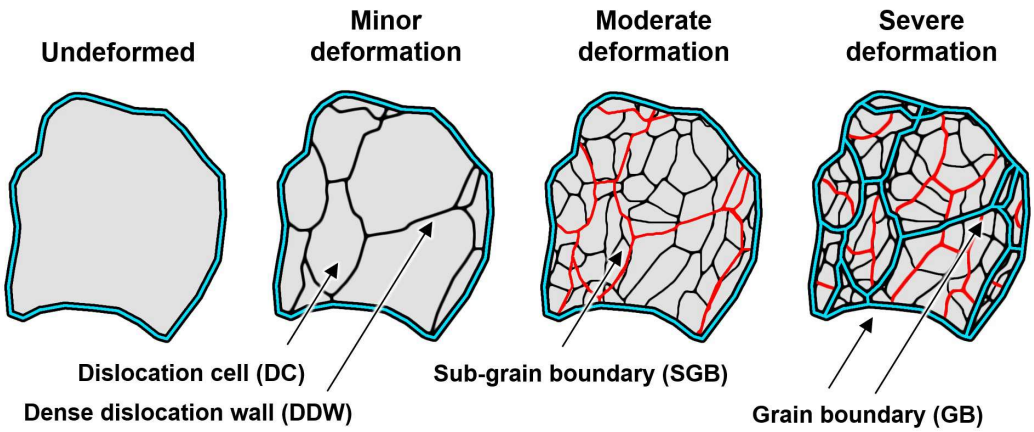

(a)

Figure 1.3: Schematic of grain refinement and cellular microstrucutre at high strains [70].

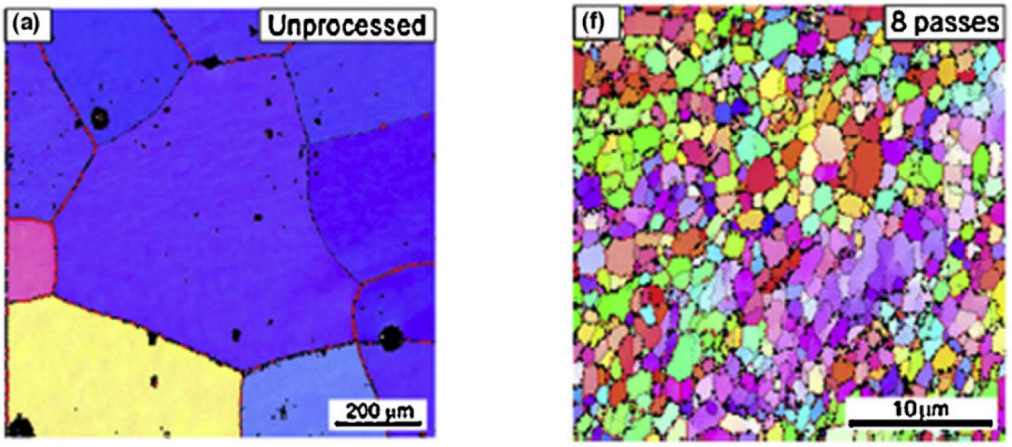

(a) (b)

Figure 1.4: Grain refinement by ECAP. (a) As-received microstructure and (b) after 8 passes of ECAP [55].

copper [117] and magnesium alloys [93] have shown a significant increase in material yield and ultimate strength after each pass of the process. This trend usually continues until the material degrades by different damage mechanisms which are related, in metal forming, to void growth inside the material or microcracks on the surface [44]. Dynamic recovery can also impede grain refinement after certain amount of deformation [115]. The heterogeneity in grain refinement may be resolved by defining several processing routes by rotating the workpiece by 90 degrees or turning it upside down after each pass [35].

In practice, discontinuous RCS process used in laboratory development stage is composed of two

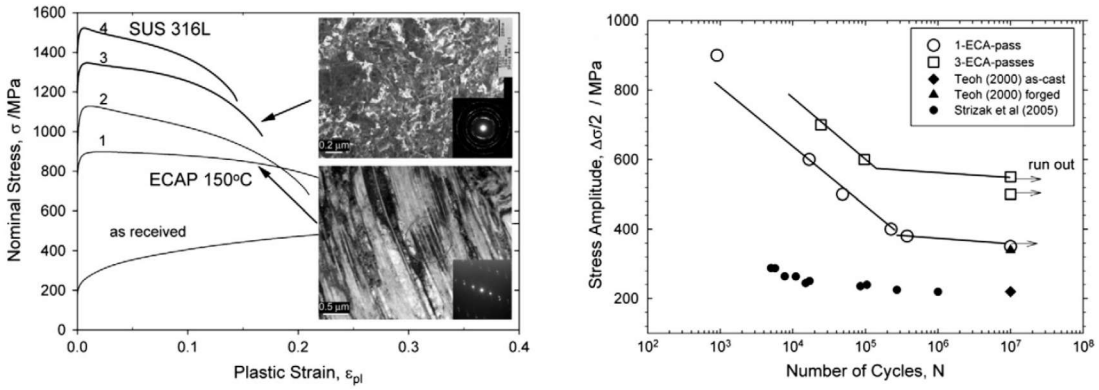

(a) (b)

Figure 1.5: Material properties after processing by SPD. (a) Stress strain curves after 0-4 passes of ECAP and (b) Wohler curve for unprocessed and processed by ECAP [34].

corrugation dies, represented in Figure 1.6, and two straightening dies which deform a sheet metal blank sequentially. First, the corrugation dies deform the blank sheet to a corrugated shape whose morphology is governed by the shape of the die. Then, the straightening dies deform the corrugated sheet to straight blank sheet (the steps of the RCS process are represented in Figure 1.7 for two patterns). This two-step process (corrugation then strengthening) is called a full RCS pass. Interestingly, since the specimen keeps its initial configuration at the end of a full pass, it is possible to repeat this process several times in order to reach higher plastic strain, which ultimately would lead to grain refinement. This process thus belongs to both forming processing and SPD-like processing. An important feature of the process is the presence of a large number of corrugation *patterns*, which are spatially repeated in order to produce plastic strains in a large domain.

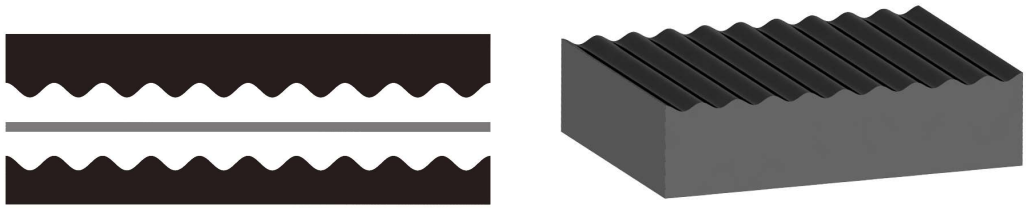

(a) (b)

Figure 1.6: Description of the corrugation dies in discontinuous RCS processing. (a) 2D representation of the two dies acting on the sheet metal blank and (b) 3D representation of the lower die.

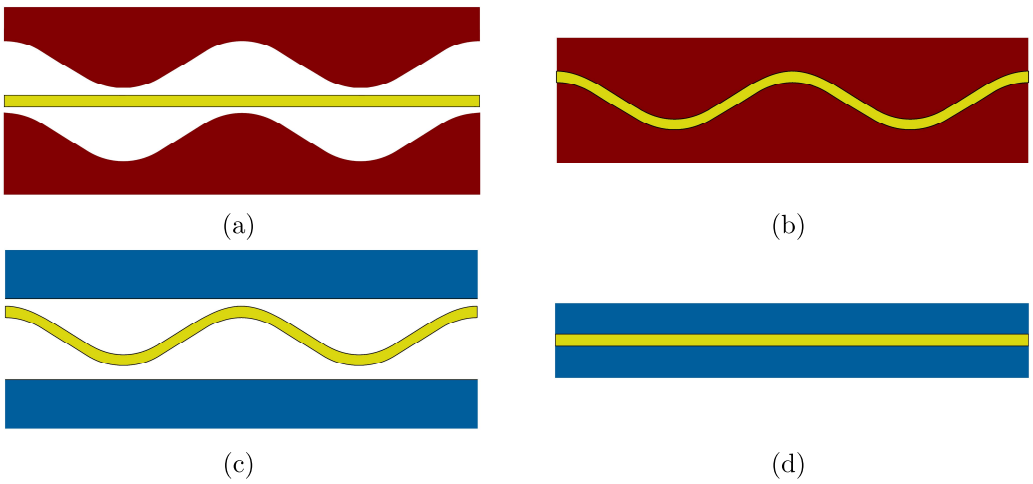

Figure 1.7: Description of one pass in RCS processing for two patterns. (a) Before corrugation, (b) At the end of corrugation, (c) Before straightening and (d) At the end of straightening.

1.3.3 Numerical modelling of RCS

The study of materials processed by SPD is generally supplemented by numerical simulations of the process. In the case of RCS, these numerical studies permit to (i) access mechanical variables that are not easily accessible by experimental measurements, such as 3D distributions of stress [49, 93, 100], (ii) study the effect of the process parameters such as the die shape [93, 100], and (iii) provide guidelines to optimize the process. In these studies, several experimental measurements and observations such as XRD, microhardness, SEM, TEM, EBSD and tensile test are generally used to validate the numerical simulations. Predictive simulations of RCS is thus of interest in order to facilitate the development of this process in industrial conditions which requires an optimization of the processing conditions. This optimization concerns notably the material behavior after processing such as strength, ductility and fracture properties.

A current lack in the numerical simulation of RCS is the absence of a “physical” description of the local mechanisms in the material modelling. In particular, a coupling between ductile damage evolution and advanced hardening laws based on the underlying mechanisms is necessary in order to simulate accurately the microstructural changes during SPD.

1.4 Modelling of hardening based on dislocation density evolution

It is generally accepted in materials processed by SPD that dislocations are the main mechanism that contributes to hardening mainly due to relatively low temperature during the process and high plastic deformation, particularly in the case of metals with FCC structure that have more slip planes [122]. During SPD, high strain is accompanied with massive nucleation and movement of dislocations. Experimental observations show that metals processed by SPD have heterogeneous areas with very high and very low densities of dislocation; dislocation distribution is in the form of a *cellular* structure that is composed of cell walls and interiors. In this assumption, cell walls correspond to the areas with high dislocation density and inside these walls, cell interiors have relatively lower dislocation density. Accordingly, it is admitted that SPD leads to creation of a "2-phase composite structure" in metals [86, 99].

Interestingly, accumulation of dislocations in cell walls leads to high misorientation of the cell walls that increases with the induced plastic deformation [32]. The increase in misorientation turns cell walls into subgrain boundaries and eventually, grain boundaries [65]. This mechanism explains the important capability of grain refinement by SPD and the formation of ultrafine grains [46, 121].

1.4.1 Stages of strain hardening

1.4.1.1 Moderate plastic deformation

During work hardening of metals, several stages can be distinguished. In a single crystal, plasticity starts with single-slip of dislocations which corresponds to stage I work hardening. This is not however the case for polycrystals as many slip activities in several grains happen at the same time [90]. As a result, this is stage II which is the dominating mechanism at the start of hardening in polycrystals and it is characterised by the occurrence of multi-slip. According to Figure 1.8, this stage is characterized by high hardening rate due to activation of secondary slip systems, and the appearance of forest dislocations. In this case, generally the stress-strain curve increases linearly with plastic strain.

As the dislocation density increases with plastic deformation, the "distance" between neighboring dislocations decreases and a mechanism of annihilation of dislocations on different slip planes happens. This temperature and strain rate dependent phenomenon is called dynamic recovery and corresponds to stage III hardening [101]. It is also responsible for softening in the stress-strain curve that happens

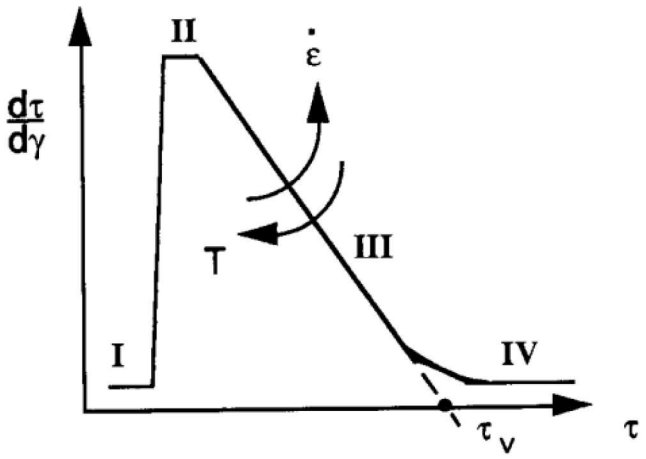

Figure 1.8: Example of a shear stress v.s. shear strain curve showing stages of work hardening in a single crystal. It should be noted that for polycrystals, stage I is almost negligible [90].

after the stage II hardening, and strain hardening rate starts to decrease (see Figure 1.8). Furthermore, due to dynamic recovery in stage III, the rate of dislocation density production also reduces.

Experimental evidence shows that the increase in dislocation density leads to creation of "hard" and "soft" zones inside the grains, representative of a cellular structure composed of cell walls (see Figure 1.2). These hard and soft zones are characterized by large and small density of dislocations. With an increase of the strain, cell walls start to shrink. The increase in total dislocation density and at the same time the shrinkage of cell walls is more dominant in stage II and slows down in stage III [33].

1.4.1.2 Severe plastic deformation

When high strains are reached, the decrease in strain hardening rate reaches a saturation level at a relatively small value which is the characteristic of stage IV hardening (see Figure 1.9b). This stage is marked by smaller dislocation density production rate and the end of cell wall shrinkage. Finally, the saturation of strain hardening ends in stage V with an gradual decrease in strain hardening rate to zero. Additionally, in this stage, the dislocation density growth rate disappears [132].

1.4.2 Strain hardening models based on dislocation density

Several attempts have been done to predict the strain hardening based on dislocation mechanisms. These models consider the mechanism of production and annihilation of dislocations. The

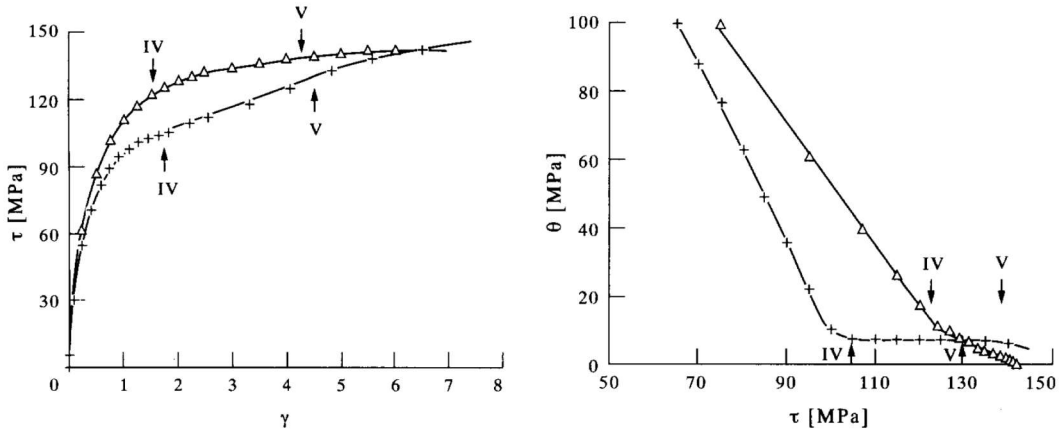

Figure 1.9: Hardening behavior of polycrystal Cu during torsion (+) and straight rolling (△) at room temperature. (a) Shear stress τ vs shear strain γ and (b) Hardening rate $\theta = d\tau/d\gamma$ vs shear stress τ [132].

most recognized first attempt was a simple one-parameter model developed by Mecking and Kocks [81]. This phenomenological model provides the evolution of average dislocation density as an ordinary differential equation with respect to plastic strain and is given in the following way:

$$\frac{d\rho}{Md\varepsilon} = k_1\sqrt{\rho} - k_2\rho. \tag{1.1}$$

Here ρ is the average dislocation density, ε is the equivalent strain, and k_1 and k_2 are constant parameters for production and annihilation of dislocations. Also in this equation M is Taylor's factor for polycrystals. This equation was very successful for prediction of strain hardening in polycrystals in stages II and III [6, 31]. However due to the complex structure of dislocations in stages IV and V, it fails to provide accurate predictions for strain hardening at high strains. Based on the experimental observations of dislocation structure in metals, a two-parameter model was proposed by Mughrabi [86] based on the description of dislocation densities in cell walls and cell interiors. In this model, the cellular structure of dislocations is assumed to create a composite of low and high dislocation density zones. This model makes it possible to capture the stages IV and V of strain hardening for high strains [90]. Using a continuum mechanics framework based on dislocation cell patterns, Estrin et al. [33] extended Mughrabi [86]'s approach by deriving constitutive equations that account for evolution of dislocations in cell walls and interior. This model is again based on the composite assumption of microstructure using two distinct phases. Hence, as a rule of mixture, the overall resolved shear stress in the material is given by a contribution from the resolved shear stress in the two phases (τ_w for cell

walls and τ_i for cell interior) according to the following relation:

$$\tau^r = v_w \tau_w^r + v_i \tau_i^r. \tag{1.2}$$

In this equation, v_w is the volume fraction of cell walls and $v_i = 1 - v_w$ is the volume fraction of cell interior. Based on experimental observations, the authors propose a phenomenological equation that corresponds to the shrinkage of cell walls during the deformation of microstructure in high strains. This model has been successfully used in several applications of SPD and machining processes and the predicted results are in very good match with experimental measurements and it permits to approximately account for grain size refinement [5, 63, 80, 133]. A brief presentation of the most important equations of this model is presented hereafter.

1.4.3 Dislocation density based composite model for strain hardening during SPD

As just explained, Estrin et al. [33]'s model is suitable for prediction of strain hardening in high strains as in SPD where hardening stages IV and V are considered. In this model the composite microstructure is evolved by a contribution of cell walls and cell interior dislocations according to Eq. 1.2. Hardening in each phase is then governed by the evolution dislocation density.

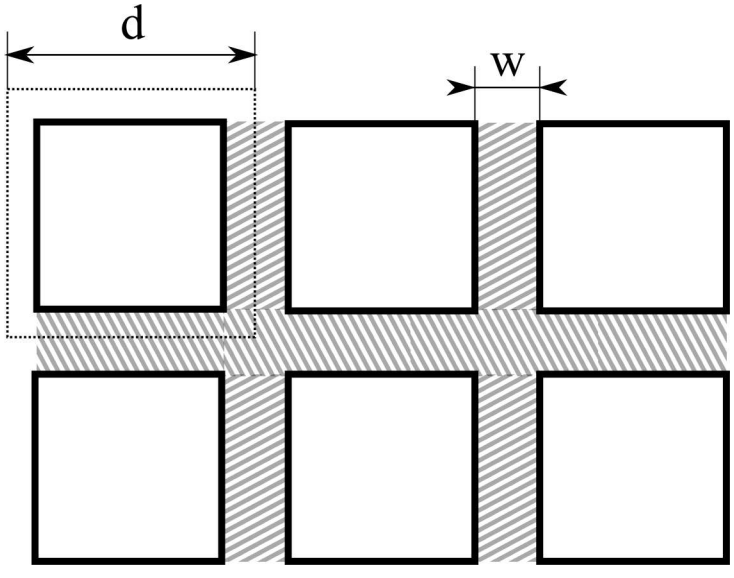

(a)

Figure 1.10: A schematic of cellular structure of dislocations composed of cell walls (dashed part) and cell interiors.

Accordingly, the resolved shear stress in each phase is given by

$$\tau_w^r = \alpha G b \sqrt{\rho_w} \left(\frac{\dot{\gamma}_w^r}{\dot{\gamma}_0} \right)^{\frac{1}{m}} \tag{1.3}$$

and

$$\tau_i^r = \alpha G b \sqrt{\rho_i} \left(\frac{\dot{\gamma}_i^r}{\dot{\gamma}_0} \right)^{\frac{1}{m}} . \tag{1.4}$$

In these equations $\dot{\gamma}_w^r$ and $\dot{\gamma}_i^r$ are the resolved shear strain rates in walls and interiors and $\dot{\gamma}_0$ is the reference strain rate. $\alpha \approx 0.25$ is a constant parameter and material parameters G and b are shear modulus and Burgers vector respectively. Also, m is a hardening exponent controlling the strain rate and temperature dependency of hardening.

The evolution of dislocation densities in this model is accounted by three different factors: generation, annihilation and migration of dislocation from cell interiors to cell walls. The evolution of dislocation densities in the cell interior is described by the following equation

$$\dot{\rho}_i = \alpha^* \frac{2\sqrt{\rho}_w}{3b\sqrt{3}} \dot{\gamma}_w - \beta^* \frac{4\dot{\gamma}_i}{bd\sqrt{v_i}} - k_0 \left(\frac{\dot{\gamma}_i}{\dot{\gamma}_0} \right)^{-1/n} \dot{\gamma}_i \rho_i. \tag{1.5}$$

The first term in this equation is the contribution of Frank-Read sources in the generation of dislocations in the cell interior, where α^* is the "fraction" of effective Frank-Read sources. The second term corresponds to the "loss" of a fraction β^* of dislocations in the cell interior due to migration of dislocation into cell walls. Here the parameter d is the cell size which is inversely proportional to the square root of total dislocation density. The third term of this equation is the contribution of dynamic recovery process in cell interior due to annihilation of dislocations, particularly by cross-slip which is an important mechanism in stage III hardening. In this equation n is the rate sensitivity exponent of dynamic recovery which is inversely proportional to the temperature.

For the evolution of dislocation density in cell walls, a similar equation is proposed in the model

$$\dot{\rho_w} = 4\beta^* \frac{\sqrt{v_i}}{bdv_w} \dot{\gamma}_i + 2\beta^* \frac{v_i \sqrt{\rho_w}}{\sqrt{3} v_w b} \dot{\gamma}_i - k_0 \left(\frac{\dot{\gamma}_w}{\dot{\gamma}_0} \right)^{-1/n} \dot{\gamma}_w \rho_w. \tag{1.6}$$

In this equation, the first term is the contribution from the dislocations migrated from cell interior to the cell walls. The second term describes the dislocations generated by activated Frank-Read sources from the dislocations migrated to cell walls and the third term is also dislocation density loss due to dynamic recovery.

The total dislocation density in the material is given by the dislocation densities in both cell walls and cell interior as

$$\rho_t = v_w \rho_w + v_i \rho_i, \tag{1.7}$$

where we recall that v_w is the volume fraction of cell walls and v_i is the volume fraction of cell interiors. The increase in dislocation density, the evolution of the cellular structure and the increase in misorientation in cell walls will eventually lead to grain refinement during SPD processes. Using Holt's equation, the average cell size (which corresponds to the average grain size) is given by the following relation

$$d = \frac{K}{\sqrt{\rho_t}}, \tag{1.8}$$

where K is a parameter assumed to be constant in this model (it could be slightly dependant on resolved shear strain [53, 65]). Lastly, motivated by experimental observation on metals, the volume fraction of cell walls is assumed to decrease with evolution of resolved shear strain according to the following empirical expression

$$v_w = v_{inf} + (v_0 - v_{inf}) \exp\left(\frac{-\gamma^r}{\Gamma^r}\right). \tag{1.9}$$

In this equation, v_{inf} and v_0 are max and saturation values of volume fraction of walls, γ^r is the overall resolved shear strain of the dislocation cell and the parameter Γ_r controls the shrinkage rate. For more details about formulation of this model, see Estrin et al. [33]. Recently, there have been some modifications in the governing equations of the model which are reported in the literature. These modification try to take into account different mechanisms in order to improve the predictions of the model such as, misorientation angle effect [32], geometrically necessary dislocation density [121], back pressure influence [80] and 3D extension of cellular model [123].

1.5 Ductile damage

1.5.1 Introduction

The ductile failure of metals is generally due to the successive nucleation, growth and coalescence of micro-voids [13, 15, 97]. It is now commonly accepted that void nucleation can occur either by

decohesion at second-phase particles–matrix interface or by particle cracking. Once voids are nucleated, plastic flow will promote the growth of these voids, which is accelerated by the stress triaxiality. Important void growth is usually followed by void coalescence which can take place in a variety of modes, the most dominant one being coalescence by internal necking [11]. Figure 1.11 schematically shows different stages of evolution of damage in metals.

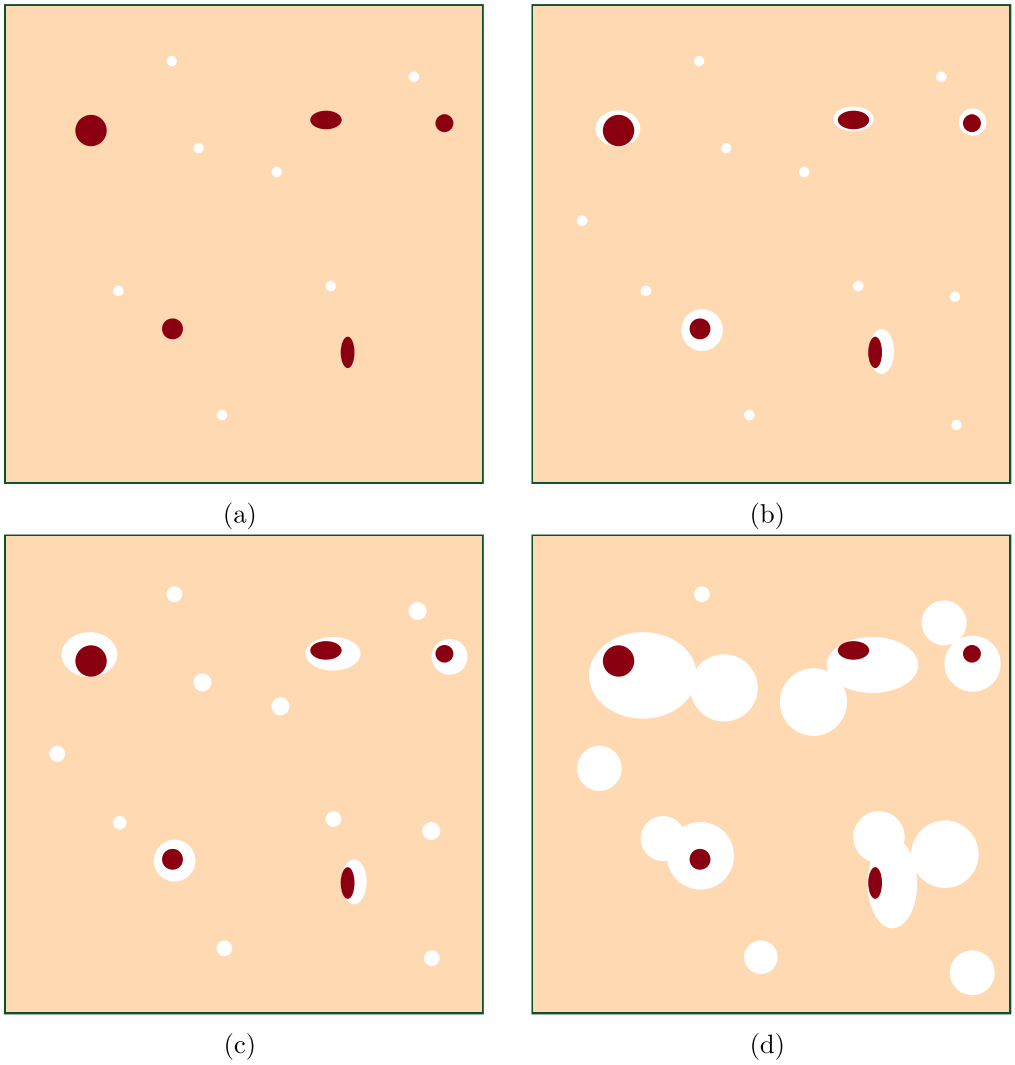

Figure 1.11: Different mechanisms of ductile damage. (a) As-recieved material, (b) Nucleation from inclusions or precipitates, (c) Growth of the microvoids and (d) Coalescence.

Several experimental methods permit to observe the presence and evolution of damage in materials. For instance, tomography/laminography method by synchrotron radiation is used in- and ex-situ to follow evolution of porosity during experimental tests [112, 116] (see Figure 1.12). Also advanced

acoustic emission methods can give access to global degradation of material [25, 78]. Moreover, observations by scanning electron microscope (SEM) are frequently used to observe fracture surfaces or particle cracking in the microstructure [25, 64]. For instance, the presence of dimples in the fracture surface permits to characterize ductile damage [97]. The shape and orientation of the dimples are of particular interest as they can be a indicator of ductile damage by tensile necking or by shear.

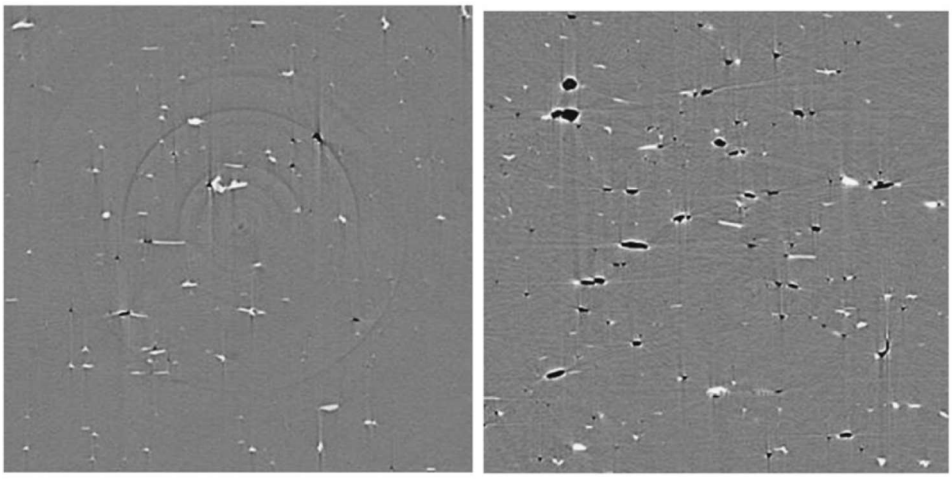

(a) (b)

Figure 1.12: X-ray microtomography observation of damage evolution. In this figure, porosity is shown in black and precipitates in white. (a) As-received and (b) After deformation [116].

Indeed, recent experimental works have shown that ductile failure can also occur under combined tension and shear, and notably with shear-dominated loadings [7, 27, 28, 39, 45, 51, 103]. In such cases, void growth is limited and the macroscopic softening is attributed to changes of the void shape and orientation, notably the flattening of voids subjected to shear.

In the context of metal forming, Kotkunde et al. [64] performed deep drawing experiments on titanium alloy under different process conditions. They distinguished two types of failure in their experiments: either by formation of shear cracks or by tensile necking (also observed by Gorji and Mohr [44]). SEM observations of crack surface in shear crack case showed the presence of elongated uni-directional dimples, where equi-axed shallow dimples were observed in the case of tensile failure (Figure 1.13). Similar deduction was also made by Torki and Benzerga [118] for shear and tension dominated loadings. These results show the importance of void shapes in understanding the underlying mechanisms of damage in plastic deformation processing.

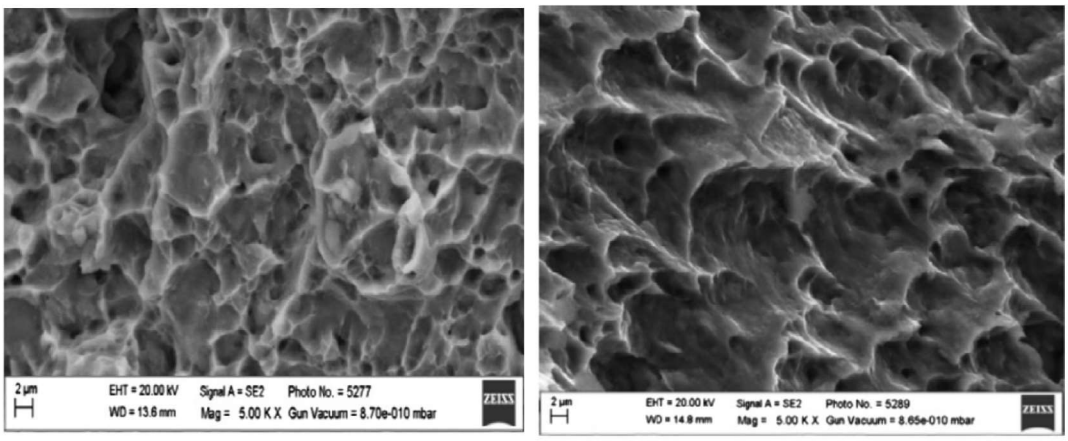

Figure 1.13: SEM fractugraphy images of cracks formed during deep drawing experiment on Ti-6Al-4V alloy. (a) Shallow equiaxed dimples as evidence of ductile tensile failure located on the bottom part of the cup (neck region) and (b) Unidirectional elongated dimples as evidence of ductile shear failure located at the upper area of the wall [64].

1.5.2 Modelling of ductile damage

The modelling of ductile damage is based on either uncoupled fracture criteria, such as the Hosford–Coulomb fracture model (see e.g. [44, 87, 135]), or coupled damage models. In the first approach, the damage parameter does not affect the material behavior, whereas in the second approach damage is coupled with elastic and/or plastic properties [114]. In the coupled damage approach, which is generally referred to as the local approach of fracture, the modelling of ductile failure is essentially based on a detailed description of the local rupture process zone [16]. Within this framework, two main approaches permit to describe ductile damage evolution.

1.5.2.1 Models based on continuum damage mechanics

Continuum damage mechanics (CDM) models are based on a thermodynamical framework following Lemaitre [71]'s pioneering work. In this approach, damage is taken into account through a phenomenological internal damage state variable (which can be scalar or tensorial), which affects both the elastic behavior and the plastic flow. This class of models is referred to as phenomenological as their development is essentially based on macroscopic considerations. The evolution of the damage variable is driven by the elastic energy release rate, in which the effect of triaxiality is accounted for. The thermodynamical consistency of CDM models together with their numerous extensions (such as

damage anisotropy, plastic compressibility, kinematic hardening, strain rate effects, etc.) make this approach attractive, from a numerical point of view, for the simulation of ductile damage [20, 106].

In terms of numerical simulation of damage evolution during sheet metal forming, most of the works have considered continuum damage mechanics (see e.g. [4, 105–107, 110, 113, 134]). The advantages of this class of thermodynamically-consistent models are that they can easily account for initial and induced anisotropies, cyclic effects, mixed hardening, through the use of advanced yield functions and plastic potentials. However, due to the intrinsic phenomenological nature of this approach, it is not guaranteed that the calibration of a set of parameters for a given loading path would lead to accurate predictions for other types of loading, since the damage parameter is not based on a physical mechanism.

1.5.2.2 Models based on micromechanics

Micromechanical type models are based on a local description of the physical mechanisms of ductile failure, following mainly Gurson [47]'s seminal work[2]. Gurson's model is based on the limit-analysis of a hollow sphere (with a rigid-plastic matrix) subjected to conditions of homogeneous boundary strain rate. This model is composed of a macroscopic yield criterion and flow rule which accounts for the presence of voids through the porosity. It is supplemented by an evolution equation for the porosity, which acts as a damage parameter in this model (although it can decrease in compression). Accordingly, the Gurson yield criterion, later modified by Tvergaard and Needleman [120] to take into account the nucleation and coalescence of microvoids, is given as follows

$$\Phi = \frac{\sigma_{eq}^2}{\bar{\sigma}^2} + 2qf^* \cosh\left[\frac{3\sigma_m}{2\sigma}\right] - 1 - (qf^*)^2, \tag{1.10}$$

where σ_{eq} and σ_m are the macroscopic equivalent and the mean stresses respectively, $\bar{\sigma}$ is the yield stress of the matrix and q is the "Tvergaard parameter" which is a heuristic modification to improve the comparison with micromechanical simulations. Additionally, f^*, a fictitious porosity parameter taking into account the rapid softening due to coalescence of voids, is given by

$$f^* = \begin{cases} f & \text{if} \quad f \leq f_c \\ f_c + \delta[f - f_c] & \text{if} \quad f > f_c, \end{cases} \tag{1.11}$$

[2]It must be noted that Gurson's model is also thermodynamically consistent as it belongs to the class of generalized standard materials if the porosity is discretized with a time-explicit scheme [30].

where f is the volume fraction of the voids and f_c and $\delta > 1$ are parameters. According to the normality condition, the plastic strain rate tensor $\boldsymbol{D}^p$ can be calculated from the yield function by the following relation:

$$\boldsymbol{D}^p = \dot{\lambda}\frac{\partial \Phi}{\partial \boldsymbol{\sigma}}(\boldsymbol{\sigma}, \bar{\sigma}, f) \quad , \quad \dot{\lambda}\begin{cases} = 0 & \text{if} \quad \Phi(\boldsymbol{\sigma}, f, \bar{\sigma}) < 0 \\ \geq 0 & \text{if} \quad \Phi(\boldsymbol{\sigma}, f, \bar{\sigma}) = 0 \ , \end{cases} \tag{1.12}$$

with $\dot{\lambda}$ being the plastic multiplier. The rate of growth of the void volume fraction is obtained from the trace of the plastic strain rate by considering the incompressibbility of the matrix

$$\dot{f}_g = (1 - f)\mathrm{tr}(\boldsymbol{D}^p). \tag{1.13}$$

Gurson assumed that the plastic dissipation energy in the hollowed cell is equal to the plastic dissipation energy in some fictitious "equivalent material" with the same volume fraction of porosity f. As a result, the hardening of the material is described by:

$$\boldsymbol{\sigma} : \boldsymbol{D}^p = (1 - f)\bar{\sigma}\dot{\bar{\varepsilon}}. \tag{1.14}$$

In this equation, the yield stress $\bar{\sigma}$ is a non-linear function of the equivalent strain $\bar{\varepsilon}$. Additionally, the strain-controlled model of nucleation rate of microvoids is given by

$$\dot{f}_{\mathrm{n}} = \frac{f_N}{s_N\sqrt{2\pi}}\exp\left[-\frac{1}{2}\left(\frac{\bar{\varepsilon} - \varepsilon_N}{s_N}\right)^2\right] \times \dot{\bar{\varepsilon}} \tag{1.15}$$

with f_n, ε_N and s_N being the model parameters [24]. Finally, the rate of the total void volume fraction $\dot{f}$ is calculated by including the contributions from both void growth and void nucleation:

$$\dot{f} = \dot{f}_g + \dot{f}_n \tag{1.16}$$

Since GTN model is limited to the description of void growth in isotropic solids, numerous extensions have permitted to account for more realistic situations including plastic anisotropy [12], void shape effects [73], kinematic hardening [85], coalescence [14], shear damage [88], etc. This approach has met, in both its original and improved forms, considerable success in the reproduction of experimental tests of failure of ductile materials [15, 97].

Nonetheless, only a few works have considered micromechanical Gurson-type models to predict failure during sheet metal forming processes [19, 59, 125, 131]. Overall, this class of models provides

good predictions when the triaxiality is high since in that case damage is mainly driven by void growth. However Gurson's model underestimates damage occurrence in presence of shear, and in that case it requires refinements to account for damage in shear, such as the incorporation of 'shear damage' as done by Ying et al. [131] in the simulation of punch tests, using Nahshon and Hutchinson [88]'s phenomenological modification of Gurson's model. However, Nahshon and Hutchinson [88]'s model predicts an increase of the porosity in pure shear which is in contradiction with micromechanical cell calculations [84]. Therefore, the accurate simulation of sheet metal forming using a micromechanical model which incorporates void growth and shear effects remains a challenge.

1.5.3 Ductile damage based on Gurson's model including void shape effects

In this work, an alternative approach for the simulation of damage under complex strain paths during sheet metal forming will be considered, based on a micromechanical description of the effect of *void growth* together with *void rotation and elongation*. Indeed, it has been shown recently that ductile failure under shear-dominated loadings is essentially due to important changes of the shape of the voids [84, 91]. Therefore, we will mainly focus on the Madou-Leblond model of plastic porous solids incorporating void shape effects [73–76], in which the voids' semi-axes and orientation can evolve, in order to simulate shear-dominated failure involved in forming processes. This model has permitted to reproduce micromechanical cell calculations in shear-dominated loadings as well as experiments on butterfly specimens with shear [83, 84] using a heuristic coalescence modelling.

1.5.4 The Madou-Leblond model for ductile materials

We briefly recall the main equations defining the Madou-Leblond model along with its extension by Morin et al. [84]. The reader is referred to Madou and Leblond [73, 74, 75] and Madou et al. [76] for a detailed description of all model developments.

1.5.4.1 Primitive form of the model

The Madou-Leblond model (which will be denoted by ML hereafter) which is an extension of Gurson's model including void shape effects, permitting to describe the evolution of cavities during shear-dominated loading supposedly responsible for shear damage. In this model, the elementary cell Ω is ellipsoidal and contains a confocal ellipsoidal cavity ω of semi-axes $a > b > c$ oriented along the

(local) unit vectors $\boldsymbol{e}_x$, $\boldsymbol{e}_y$, $\boldsymbol{e}_z$. The cavity surface is characterized by the quadratic form $\mathcal{P}$ defined by

$$\mathcal{P}(\boldsymbol{u}) \equiv \frac{(\boldsymbol{u}.\boldsymbol{e}_x)^2}{a^2} + \frac{(\boldsymbol{u}.\boldsymbol{e}_y)^2}{b^2} + \frac{(\boldsymbol{u}.\boldsymbol{e}_z)^2}{c^2}. \tag{1.17}$$

The matrix $\boldsymbol{P} \equiv (P_{ij})$ of the quadratic form $\mathcal{P}$ is expressed in the fixed frame ($\boldsymbol{e}_1$, $\boldsymbol{e}_2$, $\boldsymbol{e}_3$) of the observer and permits to describe the orientation and semi-axes ratios of the ellipsoidal cavity; indeed its diagonalization provides the semi-axes and the local unit vectors $\boldsymbol{e}_x$, $\boldsymbol{e}_y$, $\boldsymbol{e}_z$ defining the orientation. Another important parameter in this model is the porosity f which is defined as

$$f = \frac{\mathrm{vol}(\omega)}{\mathrm{vol}(\Omega)}. \tag{1.18}$$

The matrix is supposed to be rigid-perfectly plastic and obeys a von Mises criterion with a yield stress σ_0. A mixed analytical-numerical limit-analysis has been performed on this elementary ellipsoidal cell and led to the macroscopic yield criterion

$$\Phi(\boldsymbol{\sigma}, \boldsymbol{P}, f, \sigma_0) = \frac{\mathcal{Q}(\boldsymbol{\sigma})}{\sigma_0^2} + 2(1+g)(f+g)\cosh\left[\frac{\mathcal{L}(\boldsymbol{\sigma})}{\sigma_0}\right] - (1+g)^2 - (f+g)^2 \leq 0. \tag{1.19}$$

In equation (1.19):

- $\mathcal{Q}(\boldsymbol{\sigma})$ is a quadratic form of the components of the Cauchy stress tensor $\boldsymbol{\sigma}$ defined by

$$\mathcal{Q}(\boldsymbol{\sigma}) = \boldsymbol{\sigma} : \mathbb{Q} : \boldsymbol{\sigma}, \tag{1.20}$$

  where $\mathbb{Q}(\boldsymbol{P}, f)$ is a fourth-order tensor which is related to classical Willis's bound for non-linear composites (see [74]);

- $\mathcal{L}(\boldsymbol{\sigma})$ is a linear form of the diagonal components of $\boldsymbol{\sigma}$ in the basis ($\boldsymbol{e}_x$, $\boldsymbol{e}_y$, $\boldsymbol{e}_z$) defined by

$$\mathcal{L}(\boldsymbol{\sigma}) = \kappa \boldsymbol{H} : \boldsymbol{\sigma}, \tag{1.21}$$

  where $\kappa(\boldsymbol{P}, f)$ is a scalar and $\boldsymbol{H}(\boldsymbol{P}, f)$ a second-order tensor of unit trace;

- $g(\boldsymbol{P}, f)$ is the so-called 'second' porosity. It is related to the volume fraction of a fictitious prolate spheroidal void obtained by rotating the completely flat ellipsoid confocal to the ellipsoidal cavity ω about its major axis. This parameter is null in the case of prolate voids, non-zero in the case of oblate voids, and reduces to the classical 'crack density' of Budiansky in the case of penny-shape cracks. It naturally arises in the limit-analysis procedure of the ellipsoidal void and permits to account for the effect of a penny-crack (having a null porosity) on the yield surface [74].

The details and expressions of all model parameters are given in Madou and Leblond [73, 74].

The macroscopic yield criterion is then complemented by a macroscopic flow rule which is classically deduced from the normality property (since the normality of the flow rule is preserved during up-scaling):

$$\boldsymbol{D}^p = \dot{\lambda}\left[2\frac{\boldsymbol{Q}:\boldsymbol{\sigma}}{\sigma_0^2} + \frac{2}{\sigma_0}(1+g)(f+g)\,\kappa\boldsymbol{H}\sinh\left(\frac{\kappa\boldsymbol{H}:\boldsymbol{\sigma}}{\sigma_0}\right)\right] \quad , \quad \dot{\lambda}\begin{cases} = 0 & \text{if} \quad \Phi(\boldsymbol{\sigma},\boldsymbol{P},f,\sigma_0) < 0 \\ \geq 0 & \text{if} \quad \Phi(\boldsymbol{\sigma},\boldsymbol{P},f,\sigma_0) = 0, \end{cases} \tag{1.22}$$

where $\boldsymbol{D}^p$ is the Eulerian plastic strain rate and $\dot{\lambda}$ the plastic multiplier.

The evolution equation of the porosity, corresponding to void growth, is deduced from the incompressibility of the matrix

$$\dot{f}_g = (1-f)\mathrm{tr}(\boldsymbol{D}^p). \tag{1.23}$$

Finally, the evolution equation of the matrix $\boldsymbol{P}$ (characterizing the shape and orientation of the ellipsoidal voids) is given by

$$\dot{\boldsymbol{P}} = -\boldsymbol{P}.(\boldsymbol{D}^v + \boldsymbol{\Omega}^v) - (\boldsymbol{D}^v + \boldsymbol{\Omega}^v)^T.\boldsymbol{P} \tag{1.24}$$

where $\boldsymbol{D}^v$ and $\boldsymbol{\Omega}^v$ are respectively the strain-rate and rotation-rate tensors of the cavity. These rates are given by:

$$\begin{cases} \boldsymbol{D}^v &= \mathbb{L} : \boldsymbol{D}^p \\ \boldsymbol{\Omega}^v &= \boldsymbol{\Omega} + \mathbb{R} : \boldsymbol{D}^p, \end{cases} \tag{1.25}$$

where $\boldsymbol{\Omega}$ is the rotation-rate tensor of the material (antisymmetric part of the velocity gradient). The tensors $\mathbb{L}(\boldsymbol{P},f)$ and $\mathbb{R}(\boldsymbol{P},f)$ are fourth-order 'localization tensors', as the tensor $\mathbb{L}$ relates the (local) void strain-rate $\boldsymbol{D}^v$ to the macroscopic strain-rate $\boldsymbol{D}$, and the tensor $\mathbb{R}$ relates the (local) void rotation-rate $\boldsymbol{\Omega}^v$ to the macroscopic rotate-rate $\boldsymbol{\Omega}$. They are based on plastic corrections of the elastic formula provided by Ponte Castañeda and Zaidman [98] in the elastic case, determined by numerical analyses. The details and expressions of these tensors can be found in Madou et al. [76].

1.5.4.2 Extensions of the model

The primitive ML model has been completed by Morin et al. [83, 84] using several (heuristic) extensions that allow the model to be applicable for practical materials and situations. This includes notably Tvergaard's parameter, coalescence modelling, strain hardening, nucleation and bounds on the semi-axes.

First the "Tvergaard parameter" has been in both the yield criterion (1.19) and the flow rule (1.22), in order to account for more realistic shapes of the elementary cell [119]. In the ML model, this is done by replacing the term $(f+g)$ by $q(f+g)$, where q is a (heuristic) coefficient which is usually slightly larger than unity. Furthermore, it has been shown in Gologanu [40] that this parameter should depend on the void shape. Thus, following Gologanu [40] and Morin et al. [84], this parameter is given by

$$q = (1-k)q^{\text{prol}} + kq^{\text{obl}}, \quad k = \sqrt{\frac{b^2-c^2}{a^2-c^2}}, \quad \left\{ \begin{array}{lcl} q^{\text{prol}} & = & 1+(q^{\text{sph}}-1)\left[\dfrac{2a/c}{1+(a/c)^2}\right]^{3/2} \\ q^{\text{obl}} & = & 1+(q^{\text{sph}}-1)\left[\dfrac{2a/c}{1+(a/c)^2}\right], \end{array} \right. \tag{1.26}$$

where q^{sph} is Tvergaard [119]'s original value of q for spherical voids, and q^{prol} and q^{obl} those of Gologanu [40] for prolate and oblate voids.

Since ductile tearing is ultimately due to void coalescence, a simple (phenomenological) model of coalescence is generally considered. This consists in replacing the porosity f by some larger fictitious one f^*, once some 'critical value' f_c has been reached. Since in the ML model the relevant parameter in the criterion (leading to softening) is no longer f but $f+g$, Tvergaard and Needleman [120]'s modification applies to $f+g$:

$$(f+g)^* = \left\{ \begin{array}{ll} f+g & \text{if} \quad f+g \leq (f+g)_c \\ (f+g)_c + \delta[(f+g)-(f+g)_c] & \text{if} \quad f+g > (f+g)_c, \end{array} \right. \tag{1.27}$$

where $(f+g)_c$ and $\delta > 1$ are parameters. This model is heuristic and has permitted to capture the onset of coalescence in the cases of (i) unit-cell calculations in shear [84] and (ii) a butterfly specimen subjected to shear-dominated loadings [83].

The ML model is based on limit-analysis which assumes that the matrix is rigid-perfectly plastic, excluding by essence strain hardening effects. However it can be accounted for approximately by following Gurson [47]'s approximate approach[3]. The (constant) yield limit σ_0 in the criterion (1.19) is replaced by some 'average yield stress' $\bar{\sigma}$ given by:

$$\bar{\sigma} \equiv \sigma(\bar{\varepsilon}), \tag{1.28}$$

where $\sigma(\varepsilon)$ is the function providing the yield limit as a function of the local accumulated plastic strain ε, and $\bar{\varepsilon}$ represents some 'average equivalent strain' in the sound matrix. The evolution of $\bar{\varepsilon}$ is then

[3]It could also be possible to use Morin et al. [85]'s explicit approach based on sequential limit-analysis.

deduced by assuming that the plastic dissipation on the ML model

$$\boldsymbol{\sigma} : \boldsymbol{D}^p \tag{1.29}$$

is equal to the plastic dissipation in some fictitious porous 'equivalent' material which has the same porosity f. In this equivalent material, the plastic dissipation is thus taken as

$$(1-f)\bar{\sigma}\dot{\bar{\varepsilon}}. \tag{1.30}$$

The evolution equation of $\bar{\varepsilon}$ is then given by

$$\dot{\bar{\varepsilon}} = \frac{\boldsymbol{\sigma} : \boldsymbol{D}^p}{(1-f)\bar{\sigma}}. \tag{1.31}$$

Finally, void nucleation can be accounted for by considering the strain-controlled model of Chu and Needleman [24]. The nucleation rate is given by

$$\dot{f}_{\mathrm{n}} = \frac{f_N}{s_N\sqrt{2\pi}} \exp\left[-\frac{1}{2}\left(\frac{\bar{\varepsilon}-\varepsilon_N}{s_N}\right)^2\right] \times \dot{\bar{\varepsilon}}, \tag{1.32}$$

where f_N, ε_N and s_N are respectively the volume fraction, average nucleation strain and standard deviation. The evolution equation of the porosity thus reads

$$\dot{f} = \dot{f}_{\mathrm{g}} + \dot{f}_{\mathrm{n}}. \tag{1.33}$$

1.5.4.3 Scalar damage parameter characterizing failure

In the model ML, softening is due to both the porosity and void shape effects (through the second porosity). A damage parameter d, tied to both f and g, characterizing the progressive degradation of the material will be defined for post-treatment.

If we assume that the material is entirely failed ($\boldsymbol{\sigma} = \mathbf{0}$), we can obtain from the yield criterion (1.19):

$$2q(1+g)(f+g)^* - (1+g)^2 - q^2(f+g)^{*2} = -\left(1+g-q(f+g)^*\right)^2 = 0. \tag{1.34}$$

It follows that $q(f+g)^* = 1+g$. The damage parameter d can thus be defined by

$$d = \frac{q(f+g)^*}{1+g}, \tag{1.35}$$

the values $d=0$ and $d=1$ corresponding to absence of damage and total damage, respectively. This parameter, which does not play any role in the constitutive equations, permits the evaluation, as a post-treatment of the results, of the location and importance of damage in a structure.

1.6 Conclusion

This chapter presented a review of the literature on the three subjects that will be analysed in this thesis. More particularly, a review of applications of SPD processes and the characterization of processed materials was given, with a focus on the RCS process which is mainly used in this thesis. This was pursued by a review of the microsturactural analysis performed on the materials deformed up to very high strains and the approaches taken in order to model the material behavior during SPD by considering the evolution of dislocation density. Finally, a brief review of ductile damage analysis and the analytical models developed for predicting the evolution of damage was discussed and some micromechanical models based on growth and evolution of voids were presented. This literature review establishes a foundation for the numerical framework and analytical model that are developed in this thesis.

Chapter 2

Analysis of shear damage: A case of conventional plastic deformation process

2.1 Resumé en francais

Dans ce chapitre nous analyserons l'évolution de l'endommagement par cisaillement en emboutissage qui est considéré comme un processus de déformation plastique conventionnel. Un modèle numérique dans le code de calculs par éléments finis ABAQUS est développé pour effectuer des simulations en utilisant le modèle Madou and Leblond [74] (ML) qui inclut les effets de forme des vides. Les résultats expérimentaux issus des travaux de Gorji and Mohr [44] sur un procédé d'emboutissage profond ont été choisis comme référence pour nos simulations. Ces résultats ont été choisis principalement parce qu'ils abordent deux cas différents conduisant à des fissures, soit de cisaillement soit de striction selon la triaxialité des contraintes. Cette démarche est intéressante car elle permet d'étudier le potentiel du modèle ML notamment à faible triaxialité de contrainte. Ce chapitre est organisé de la façon suivante :

Dans un premier temps, nous présenterons brièvement la procédure expérimentale introduite dans le travail de Gorji and Mohr [44]. Ensuite, le cadre numérique dans ABAQUS est présenté ainsi qu'une brève explication de l'application numérique du modèle ML dans ABAQUS en utilisant une routine UMAT. Une identification des paramètres des matériaux basée sur des essais de traction numériques et expérimentaux sera présentée. Les paramètres identifiés seront ensuite utilisés pour effectuer des simulations numériques d'emboutissage en utilisant les modèles d'endommagement ML et GTN, et les résultats seront discutés et comparés.

2.1.1 Procédure expérimentale

Nous considérons les expériences d'emboutissage réalisées par Gorji and Mohr [44] (voir également Gorji et al. [43] et Pack et al. [94]). Le type de rupture est illustré à la Figure 2.3 pour diverses conditions de traitement. Trois comportements différents ont été observés, en fonction des conditions expérimentales :

- *Pas de rupture, qui se produit pour de petits flans.*
- *Fissure de striction, qui est le type de rupture le plus typique dans la pratique. (voir Figure 2.2).*
- *Fissure de cisaillement, qui peut se produire au niveau du profil de la matrice, lorsque le matériau se déplace sur le coin de la matrice (voir Figure 2.2).*

Dans ces expériences, le matériau considéré est un alliage d'aluminium 6016-T4 largement utilisé dans les applications automobiles en raison de sa ductilité et de sa capacité de durcissement par vieillissement.

2.1.2 Modèle numérique

Un modèle 3D par éléments finis du procédé d'emboutissage profond a été réalisé à l'aide du code commercial ABAQUS/Standard. En raison de la symétrie du procédé, seul le $1/8^e$ de l'échantillon est considéré (voir Figure 2.4). Par ailleurs, le modèle ML a été implémenté numériquement dans le code d'éléments finis Abaqus par une procédure UMAT (voir Morin et al. [84] et Leblond [66]) avec plusieurs modifications ad-hoc :

- *Éviter les effets de contact entre les demi-axes ellipsoïdaux.*
- *Éviter que la matrice $\boldsymbol{P}$ soit mal-définie en fixant un rapport maximal pour les demi-axes.*
- *Supprimer les éléments en cas d'adoucissement rapide pour éviter tout problème de convergence numérique.*

2.1.3 Identification des paramètres du modèle

Afin de mettre en œuvre le modèle ML et d'effectuer des simulations numériques des essais expérimentaux présentés dans la Section 2.3, nous avons besoin (i) d'un ensemble de paramètres qui

régissent le modèle d'évolution des dommages et (ii) de calibrer les paramètres du modèle.

Nous supposons que le comportement de l'alliage d'aluminium 6016-T4 est isotrope et que l'écrouissage du matériau suit une loi de Swift-Voce dont les paramètres sont fournis dans le Tableau 2.2.

Pour effectuer la calibration, un modèle FEM représentant l'essai de traction expérimental a été utilisé et différents jeux de paramètres ont été considérés pour simuler l'essai de traction. Pour la calibration des paramètres liés à l'endommagement, la porosité initiale et les paramètres de nucléation ont été calibrés par Thuillier et al. [116] et nous avons adopté leurs résultats sur le même matériau pour calibrer les paramètres de notre modèle. Les paramètres de coalescence sont calibrés en ajustant les prédictions du modèle avec l'évolution de la fraction volumique des vides fournie par Thuillier et al. [116]. Un résumé de tous les paramètres de l'endommagement est donné dans le Tableau 2.3. Dans la Figure 2.5, la comparaison entre les courbes de contrainte-déformation expérimentales et numériques est présentée et les résultats montrent une bonne correspondance entre la simulation et l'expérience avant et après le striction.

2.1.4 Résultats

Selon la Figure 2.3, pour une force de maintien du flan donnée, le type de défaillance dépend de la taille du flan carré. Par conséquent, dans un premier temps, nous effectuons des simulations numériques pour étudier l'effet de la taille du flan.

En résumé, le modèle ML permet de reproduire des 'fissures de striction' pour les grands flans et des 'fissures de cisaillement' pour les petits flancs. L'évolution des paramètres internes du modèle ML a permis de mettre en évidence l'importance des effets de la forme des vides sur la rupture finale. Lorsque la triaxialité est faible, la porosité diminue mais les rapports entre les demi-axes des vides augmentent ce qui conduit à un certain adoucissement : en effet, dans ce modèle, l'adoucissement peut être induit par des effets de forme des vides à travers la seconde porosité. Enfin, la comparaison avec le GTN montre sa difficulté à simuler avec précision la rupture car il surestime généralement la ductilité en ne tenant pas compte des effets de forme des vides, en particulier à faible triaxialité.

Ces résultats sont particulièrement encourageants pour la simulation de l'évolution de l'endommagement lors des procédés de mise en forme tels que la déformation plastique sévère dans laquelle l'échantillon subit une importante déformation en cisaillement.

2.2 Introduction

In this chapter, we will analyse the evolution of shear damage in deep drawing which is considered as a conventional plastic deformation process. A numerical framework in ABAQUS finite element software is developed to perform simulations using the Madou and Leblond [74] (ML) model which includes void shape effects and was previously introduced in Chapter 1. Experimental results from the work of Gorji and Mohr [44] on a deep drawing process have been chosen as the reference for our simulations. These results have been chosen mainly because they address two different cases leading to shear and necking cracks depending on the stress triaxiality. This is an interesting process as it permits investigating ML model's potential notably at low stress triaxiality. This chapter is organized as follows:

As a first step, we will briefly present the experimental procedure introduced in the work of Gorji and Mohr [44]. Then, the numerical framework in ABAQUS is presented along with a brief explanation of the numerical application of ML model in ABAQUS using a UMAT subroutine. An identification of material parameters based on numerical and experimental tensile tests will be presented. The parameters identified will then be used to perform numerical simulations on the deep drawing numerical set-up using both ML and GTN damage models and the results are discussed and compared.

2.3 Experimental procedure

We consider the deep drawing experiments performed by Gorji and Mohr [44] (see also Gorji et al. [43] and Pack et al. [94]). The deep drawing experiments have permitted to characterize the out-of-plane shear fracture. The schematic of the experimental set-up is represented in Figure 2.1: it is composed of a cylindrical punch with a 75 mm diameter and 5 mm edge radius and a 77 mm diameter die with 3 mm edge radius. The metal blank has a square shape (of size $L \times L$) and a thickness of 1 mm. A double-sided greased blank is drawn at a speed of 1 mm/s until rupture occurs.

Three different behaviors have been observed, depending on the blank's layout and blank holder force:

- *No failure*, which happens for small layouts.
- *Bottom crack*, which is the most typical type of failure in practice. A crack occurs on the side

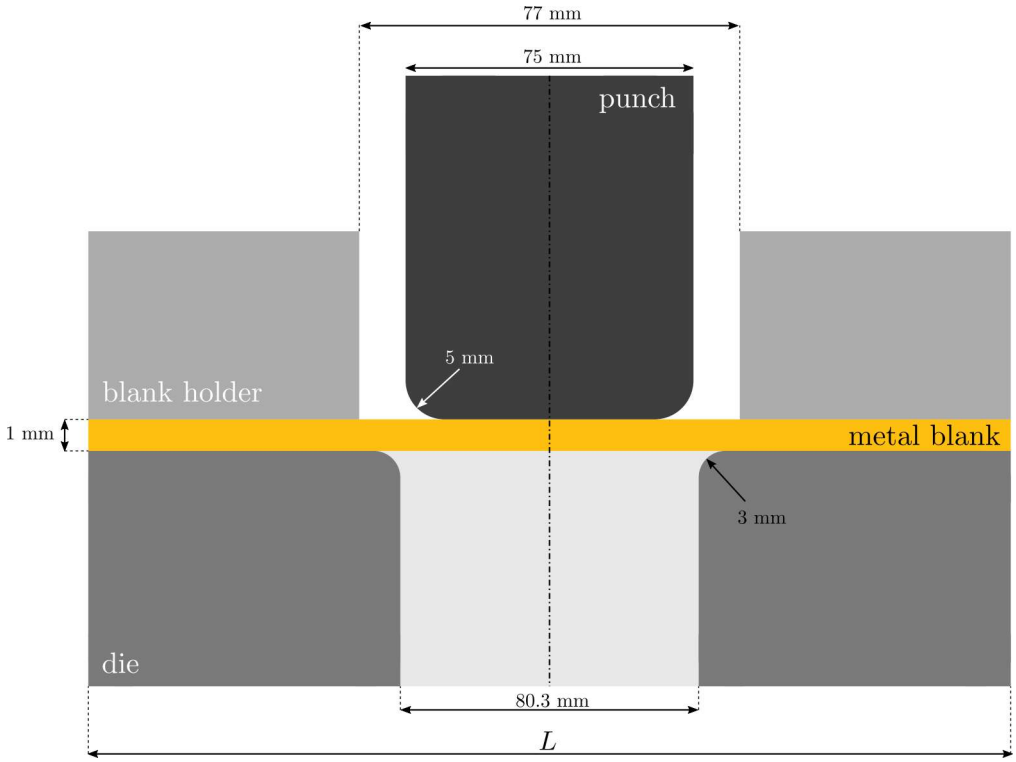

Figure 2.1: Set-up of the deep drawing experiments.

wall, near the punch-side of the workpiece (see Figure 2.2).

- *Shear crack*, which may occur at the die profile, when the material is traveling over the corner of the die (see Figure 2.2).

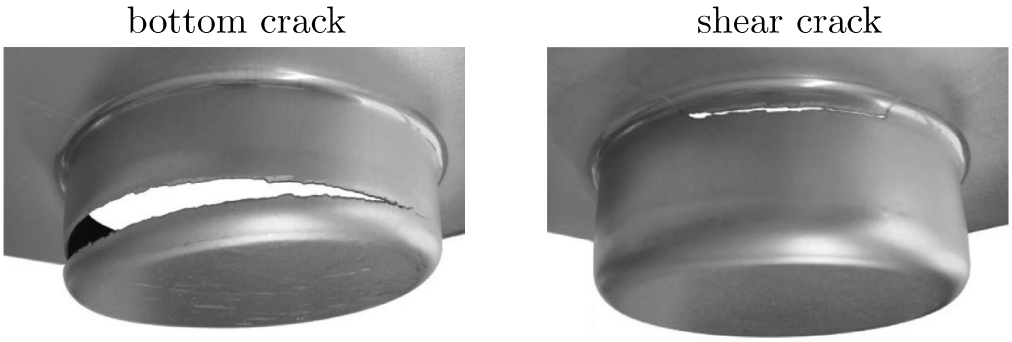

Figure 2.2: Location of cracks observed experimentally in deep drawing experiments (after [43]). In the case of a blank-holder force of 200 kN, a shear crack appears for a blank size L between 133 mm and 150 mm while a bottom crack occurs for a blank size L above 150 mm.

It has been observed by Gorji et al. [43] that bottom cracks appear for large metal blanks while shear

cracks appear for small metal blanks. For a blank-holder force of 200 kN, shear cracks occur for a blank size L between 133 mm and 150 mm while bottom cracks occur for a blank size L above 150 mm. The type of failure is shown in Figure 2.3 for various processing conditions. In the case of the shear crack, it has been observed by Gorji et al. [43] that the fracture surface is *slanted*. This confirms that this failure mode is due to a shear-dominated loading because slant cracks are generally related to shear band localization [13].

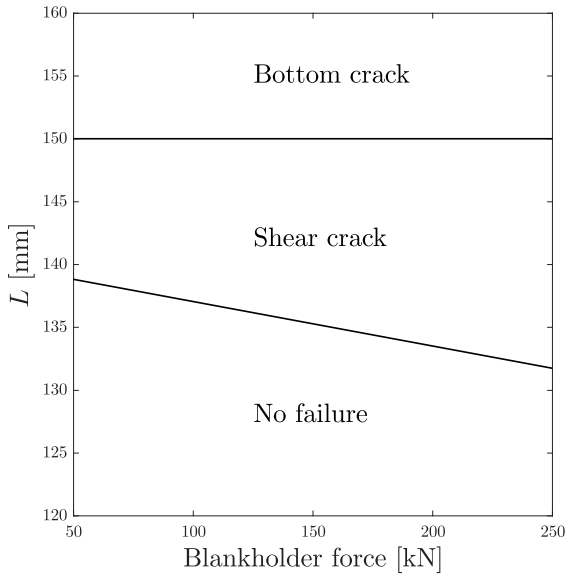

Figure 2.3: Type of failure observed during deep drawing depending on the processing conditions [41].

In these experiments, the material considered is an aluminum alloy 6016-T4 which is a heat treatable Al–Mg–Si alloy widely used in automotive applications due to its good formability and age-hardening capacity. Its chemical composition is given in Table 2.1 [116].

Table 2.1: Chemical composition of the Al-6016-T4 alloy.

Element	Mg	Si	Ti	Fe	Cr	Others (Cu, Zn)	Al
wt%	0.25-0.6	1.0-1.5	max 0.15	max 0.5	max 0.1	max 0.2	balance

2.4 Numerical model

2.4.1 Deep drawing FEM model in ABAQUS

A 3D finite element model of the deep drawing process has been made using the commercial code ABAQUS/Standard. Due to the symmetry of the process, only $1/8^{th}$ of the specimen is considered (see Figure 2.4). The sheet metal is modelled as a 3D deformable part and the mesh is composed of 29575 elements and 36276 nodes; we use selectively subintegrated 8-node trilinear brick (C3D8 elements in ABAQUS) which are suitable for quasi-incompressible plasticity as they permit to overcome volumetric locking. The mesh contains 6 elements in the sheet thickness. The punch, blank-holder and die are modeled as rigid 3D shells and are meshed with 2266, 1978 and 2380 R3D4 elements respectively. Contact conditions are considered between the sheet and the rigid parts: the friction is accounted for by a Coulomb friction model in which the frictional force is related to the normal pressure applied on the surface. A value of 0.015 for the friction coefficient was used in the simulations as the blank during the experimental process was completely greased on both sides.

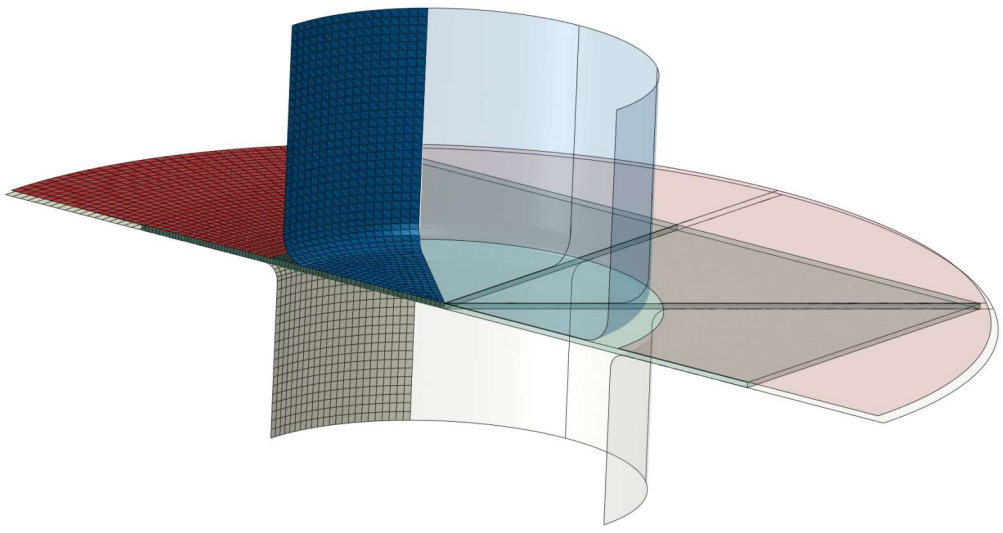

Figure 2.4: Mesh considered for the deep drawing simulations. Half of the experimental model is shown as transparent parts and only $1/8^{th}$ of the model is meshed. For illustrative purposes, the distributions of the mechanical quantities will be represented on the whole specimen using symmetry.

2.4.2 Numerical implementation of ML model

The ML model has been implemented numerically in the finite element code Abaqus through a UMAT procedure (see Morin et al. [84] and Leblond [66]). Several ad-hoc modifications have been added to the previous constitutive equations to avoid numerical issues:

- *Contact effects.* Since the ellipsoidal shape can evolve during straining, the semi-axes a, b and c can decrease. In order to avoid negative values after their evolution, contact conditions have been incorporated heuristically. Minimum (positive) values $a_{\min}$, $b_{\min}$ and $c_{\min}$ are prescribed. Then, if at some stage of the calculation the value of a semi-axis, say c, becomes smaller than its minimal value $c_{\min}$, it is replaced by $c_{\min}$. In turns the porosity is adjusted to match the new value (updated) of the semi-axis.

- *Maximal ratio a/c.* As in the previous case, several numerical issues may occur when the ratio a/c is too large, because in that case the matrix $\boldsymbol{P}$ is ill-defined which leads to numerical problems in the calculation of the eigenvalues. Then, if at some stage of the calculation the ratio a/c becomes larger than a limiting value $(a/c)_{\max}$, it is replaced by $(a/c)_{\max}$. (As before, the porosity is adjusted to match the new value (updated) of the semi-axis).

- *Element deletion.* In practice, softening can become abrupt when the damage parameter reaches high values, typically when $d \geq 0.3$. In absence of void shape effects (i.e. $g = 0$) and using $q = 1.5$, this value would correspond to $f^* = 0.2$ so damage is already very important. Therefore, it is of interest to 'delete' elements that can be considered as (almost) totally damaged. Indeed in practice when such high values are reached, fracture occurs almost instantaneously. Thus, when the damage parameter d becomes larger than a critical value, d_F, the stress is imposed to become nil, that is $\boldsymbol{\sigma} = \mathbf{0}$, which corresponds to element deletion.

- *Void growth porosity.* In order to unravel the effect each damage mechanisms upon the failure, we will also consider as post-treatments, the 'nucleated porosity' $f_{\rm n}$ and the 'void growth porosity' $f_{\rm g}$ which are defined from their respective rates (1.32) and (1.23) by

$$f_{\rm n} = \int_0^t \dot{f}_{\rm n}(\tau)\mathrm{d}\tau; \quad f_{\rm g} = \int_0^t \dot{f}_{\rm g}(\tau)\mathrm{d}\tau = f - f_{\rm n} - f_0. \tag{2.1}$$

It is interesting to note that in the case of void collapse (if $\boldsymbol{D}^p < 0$), the so-called 'void growth porosity' f_{g} can be negative but it must verify

$$f_{\mathrm{g}} \geq -f_0 - f_{\mathrm{n}} \tag{2.2}$$

since the total porosity f cannot be negative.

2.4.3 Comments

The ML model contains numerous parameters which in fact depend solely on a small set of initial parameters:

- Initial volume fraction: f_0;
- Initial void shape and orientation of the cavity: $\boldsymbol{P}_0$;
- Coalescence parameters: $(f+g)_c$ and δ;
- Nucleation parameters: ε_N, s_N and f_N.

Once these parameters are known, the yield criterion is fully determined. The porosity f is then evolved using equation (1.33), and the quadratic form is evolved using equation (1.24). If we assume that the voids are initially spherical (which is the case in most practical situations), the matrix $\boldsymbol{P}_0$ is a multiple of the identify matrix, and the remaining parameters to calibrate (f_0, $(f+g)_c$, δ, ε_N, s_N and f_N) correspond to the same parameters that are initially required for GTN model. Therefore, if voids are initially spherical, the calibration of ML can be done exactly as for GTN model, and void shape effects are an *emergent feature* of the model.

2.5 Model parameter identification

In order to implement the ML model and perform numerical simulations of the experimental tests presented in Section 2.3, we need (i) a set of parameters that govern the damage evolution model and (ii) the hardening behavior of AA6016-T4. In this section, we detail the procedure of identification of these parameters.

2.5.1 Material hardening behavior

First, since 6016-T4 aluminum alloy exhibits a very small anisotropy [21, 42, 94], we assume that its behavior is isotropic and the hardening behavior of the material is assumed to follow a Swift-Voce law:

$$\sigma(\varepsilon) = \omega A \left(\bar{\varepsilon}_p + \varepsilon_0\right)^n + (1-\omega)\left(k_0 + Q\left(1 - e^{-\beta\bar{\varepsilon}_p}\right)\right), \tag{2.3}$$

where the parameters ω, A, n, ε_0, k_0, Q and β have been calibrated by Gorji and Mohr [44] and are provided in Table 2.2. In equation (2.3), $\bar{\varepsilon}_p$ is the accumulated plastic strain.

Table 2.2: Swift-Voce hardening law parameters for the AA6016-T4.[44]

Material	ω	A [MPa]	n	ε_0	k_0 [MPa]	Q [MPa]	β
AA6016-T4	0.739	286.15	0.229	0.0161	160.1	464.5	9.89

2.5.2 Identification of damage parameters

In order to perform the calibration, a FEM model representing the experimental tensile test was used and different sets of parameters have been considered to simulate the tensile test. These sets were based on possible ranges of parameters found in the literature, notably for AA6016-T4. The set that showed the closest similitude with the experimental stress-strain curve was chosen (by a least square method). In a second step, fine-tuning of this set of parameters was performed in a try and error way to identify the possible values.

The most difficult part concerns the calibration of the parameters related to damage (initial porosity, initial shape of voids, nucleation parameters and coalescence parameters). For the same aluminium alloy AA6016-T4, the initial porosity and nucleation parameters have been calibrated by Thuillier et al. [116] using X-ray micro-tomography during interrupted tensile tests. Thus, we have adopted their results on the same material to calibrate the parameters of our model. In several test samples, the initial volume fraction was found to vary in-between 4.64×10^{-4} and 5.98×10^{-4}; therefore we have considered the value $f_0 = 5\times10^{-4}$. Furthermore, in the initial state, voids can be considered as spherical so that the initial matrix $\boldsymbol{P}_0$ is a multiple of the identity matrix; we thus consider that $(P_0)_{ij} = \delta_{ij}$ (where δ_{ij} is Kronecker symbol). A value $q = 1.5$ was classically considered for the Tvergaard parameter. Then, the experimental evolution of the void volume fraction as a function of the strain (in a tensile test) has permitted to calibrate the nucleation parameters (see Thuillier et al. [116]): $f_N = 0.018$, $\varepsilon_N = 0.9$

and $s_N = 0.4$. The coalescence parameters are calibrated by fitting the model's predictions with the evolution of void volume fraction provided by Thuillier et al. [116]: this leads to $(f+g)_c = 0.002$ and $\delta = 6$. Finally, a value $d_F = 0.3$ was chosen for the element deletion (in order to avoid numerical instabilities during total fracture). A summary of all the damage parameters is given in Table 2.3.

Table 2.3: Parameters for the model ML in the case of the AA6016-T4.

	q	f_0	$(f+g)_c$	δ	f_N	ε_N	s_N	d_F	$(P_0)_{ij}$
AA6016	1.5	0.0005	0.002	6	0.018	0.9	0.4	0.3	δ_{ij}

It must be noted that the critical value $(f+g)_c$ that has been calibrated *seems* small, although it is in the range of actual values from the literature for GTN model [10]. Furthermore, it has been shown by Springmann and Kuna [111] that, in the case of GTN model, several sets of parameters (f_0, f_c) can lead to nearly similar predictions of a tensile test. They notably show that an increase of f_0 of one order of magnitude requires that f_c is also increased by one order of magnitude. Therefore, since we considered a very small value for the initial porosity $f_0 = 5 \times 10^{-4}$, it is not surprising that the critical value is 'small'. Nonetheless, the ratio $(f+g)_c/f_0$ (which is equal to 4) and the value of δ are in agreement with previous numerical studies of shear-dominated fracture using the model ML [83, 84].

In Figure 2.5, the comparison between the experimental and numerical stress-strain curves is presented. Here we have compared the stress-strain curves calculated by FEM implementation of ML and GTN models in a tensile test with experimental results. Damage parameters can effect the behavior of the material after necking and the rate of softening. This corresponds to the rate of coalescence and growth of voids in the necking area as the triaxiality increases after necking. The results show good match between simulation and experiment before and after necking.

2.6 Results

2.6.1 Blank size effect

According to Figure 2.3, for a given blank-holder force, the type of failure depends on the size of the square blank. Therefore, as a first step we perform numerical simulations of damage to study the blank size effect.

Process conditions The deep-drawing process will be considered for a blank-holder force $F = 200$

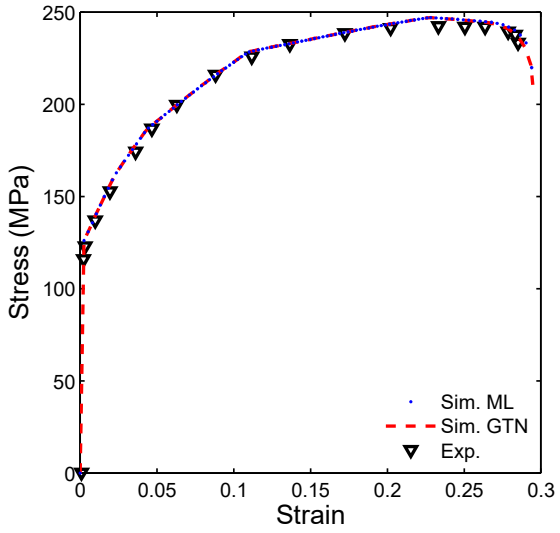

Figure 2.5: Experimental and numerical stress-strain curves by ML and GTN models of the aluminum alloy 6016-T4 used in the deep drawing experiments.

kN. For this force, it was observed experimentally that the cracking model depends on the blank size. Hence, several blank sizes, ranging from 130 mm to 152 mm, will be considered in the numerical simulations to study the cracking mode. We will then present detailed results in only two cases which lead to different damage mechanisms. We consider (i) a large blank size $L = 152$ mm for which a *bottom crack* occurs and (ii) a small blank size $L = 140$ mm, for which a *shear crack* occurs.

Quantities investigated Several quantities will be studied in order to investigate the damage occurrence during deep drawing: (i) the distribution of the damage parameter d and the porosity f in the whole specimen at several snapshots and (ii) the evolution of several internal parameters (f, f_{n}, f_{g}, g, d, and semi-axes ratios) and the triaxiality (T) in the element that fails first.

2.6.1.1 Bottom crack case

We begin with the simulation of a bottom crack during deep drawing with a blank-holder force $F = 200$ kN. For this force, bottom cracks are simulated numerically for blank sizes roughly higher than 145 mm, which is in agreement with the experimental observations (see Fig. 2.3).

In the case $L = 152$ mm which is considered hereafter, the numerical simulation ends at a displacement of about 20 mm, due to a numerical instability: the very final stage of the fracture process

becomes unstable and the final softening is brutal, the slope of the force-displacement curve becoming vertical. Hence, the bottom crack simulated numerically occurs for a punch displacement which is in agreement with the experimental value (of about 20.5 mm).

The distribution of the damage parameter d is represented for several punch displacements (16 mm, 18 mm and 20 mm which corresponds to final step of the calculation) and is compared to the fractured specimen in Figure 2.6. The location of the crack at the bottom of the specimen (through the damage parameter d) is globally well reproduced by the ML model during the simulation, by comparison to the photograph of the quasi-fractured specimen (Figure 2.6).

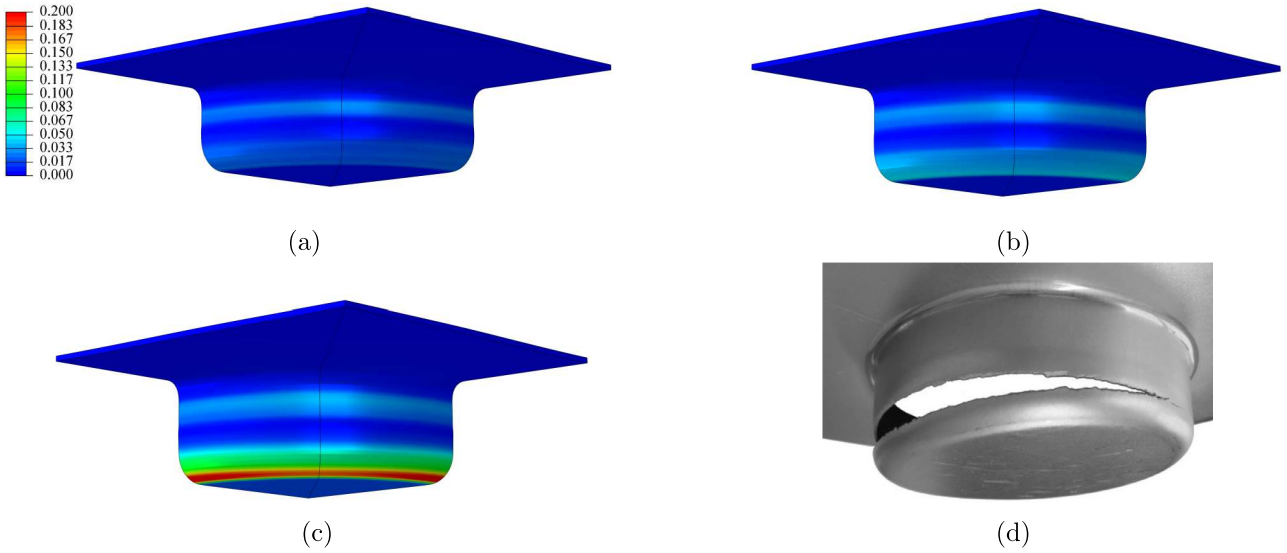

Figure 2.6: Location of the bottom crack during deep drawing with a blank size $L = 152$ mm. (a) Distribution of the damage parameter d for a punch displacement of 16 mm, (b) Distribution of the damage parameter d for a punch displacement of 18 mm, (c) Distribution of the damage parameter d for a punch displacement of 20 mm (final step of the simulation) and (d) Photograph of the quasi-fractured specimen (after Gorji and Mohr [44]).

In addition, the distribution of the porosity f is represented in Figures 2.7 for two punch displacements (16 mm and 20 mm). The distribution of the porosity is very similar to that of the damage parameter in terms of pattern. However, the maximal value of the porosity reaches 0.02 while it was roughly 0.2 for the damage parameter (for a punch displacements of 20 mm). Therefore, according to the definition of the damage parameter d (see equation (1.35)), the difference between the values of d and f can be attributed by two factors, void shape effects (through the second porosity g) and/or coalescence (through the term $(f + g)^*$).

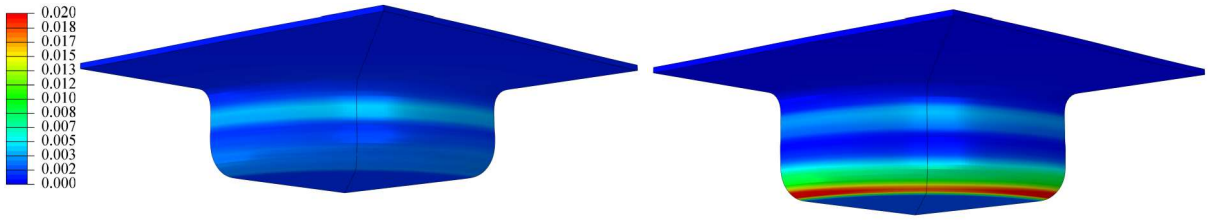

(a) (b)

Figure 2.7: Distribution of the porosity f in the simulation of a bottom crack during deep drawing with a blank size $L = 152$ mm. (a) Punch displacement of 16 mm and (b) Punch displacement of 20 mm.

In order to investigate the role of each mechanism in the final failure, the evolution of the total porosity f, second porosity g, nucleated porosity f_{n} (defined by equation (2.1)), void growth porosity f_{g} (defined by equation (2.1)), stress triaxiality T and semi-axis ratios a/c and b/c are represented (versus the punch displacement) in Figure 2.8 in the element that fails first. Prior to the coalescence occurrence (for a punch displacement before 13 mm), it is interesting to note that both f_{g}, f_{n} and g increase, with similar rates. Therefore, it can be considered that the onset of coalescence is equitably triggered by void growth, void nucleation and void shape effects. The importance of void growth and nucleation on ductile failure during deep drawing with large blanks is actually expected as it was shown in previous works that Gurson's model (for spherical voids) permits to reproduce the location of bottom cracks (see e.g. [60]). However, it is still interesting to note that in this case, the triaxiality in this element is roughly constant before localization with a value $T \sim 0.6$: this corresponds to a bi-axial stress state. This is confirmed by the evolution of the semi-axis a/c and b/c, as the major and middle axes are almost the same during the evolution so that the cavity is close to an oblate spheroidal void. The maximal value for the semi-axes ratio is of about $a/c \sim 1.7$ which can be considered as *moderate* void shape effects.

It is important to note that, after coalescence, the evolution of the internal parameters should be interpreted carefully [84]. Indeed, once coalescence begins, the quantity $(f + g)$ is replaced by $(f + g)^*$ (using the heuristic model of [120]) in the criterion and the plastic flow rule. Hence, the criterion and plastic flow are modified, which in turns increases (notably) the void growth rate. This explains that the porosity f starts increasing rapidly. Interestingly, the second porosity g also increases rapidly, although void shape effects seem to decrease as the ratios a/c and b/c decrease after a punch displacement of 15 mm.

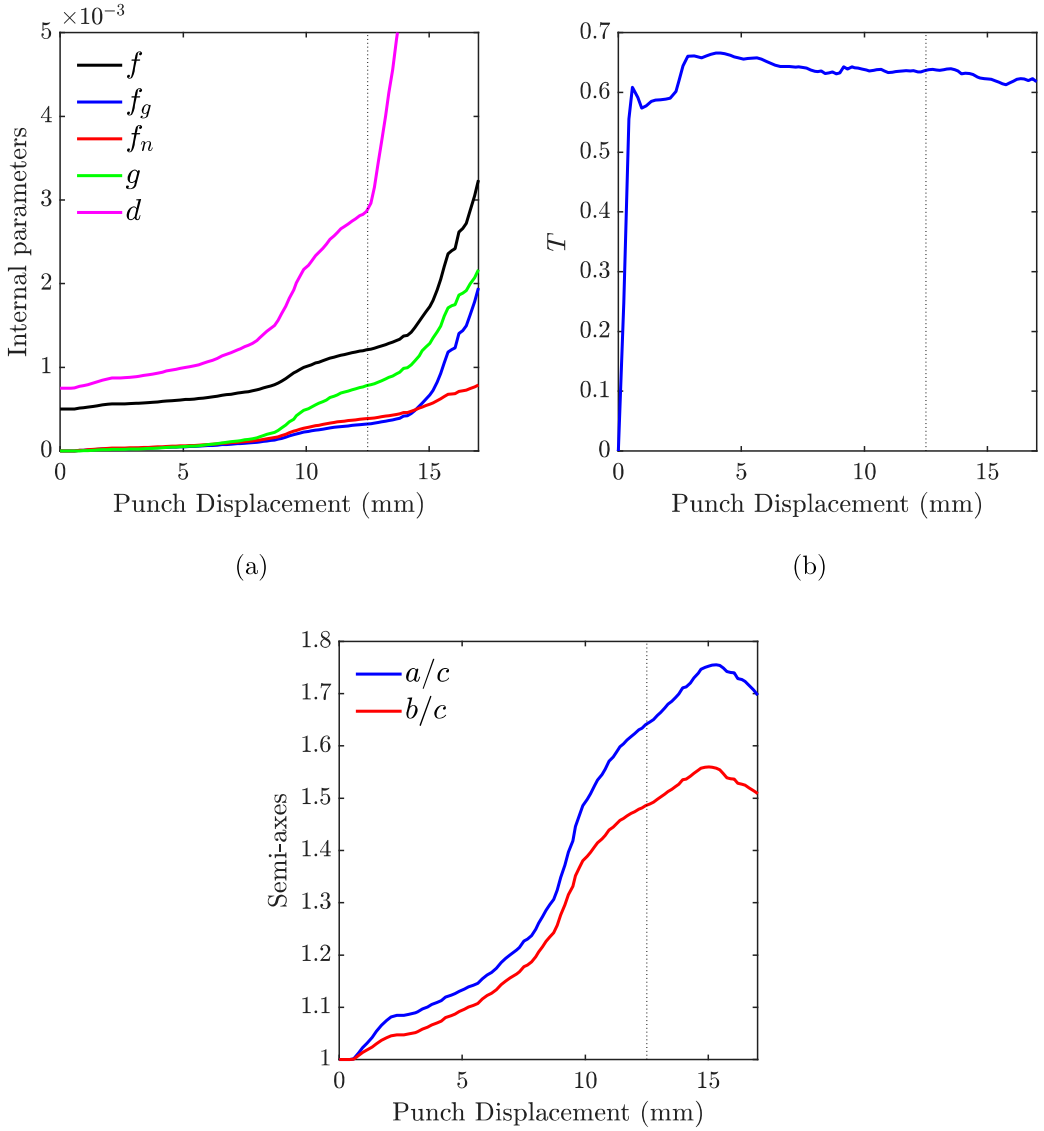

Figure 2.8: Evolution of internal parameters in the element that fails first in the simulation of bottom crack during deep drawing (with a blank size $L = 152$ mm). (a) Damage parameter d, total porosity f, second porosity g, nucleated void f_{n} and porosity due to void growth f_{g}, (b) Stress triaxiality T and (c) Semi-axes a/c and b/c. The onset of coalescence is represented by a dotted vertical line.

2.6.1.2 Shear crack case

We continue with the simulation of a shear crack (still with a blank-holder force $F = 200$ kN). For this blank-holder force, shear cracks always occur for a blank size roughly between 130 mm and 145

mm, which is in agreement with the experimental observations (see Fig. 2.3).

In the case $L = 140$ mm which is considered hereafter, the numerical simulation ends at a displacement of about 28.8 mm, due to a numerical instability: indeed, as in the case of a bottom crack, the very final stage of the fracture process becomes unstable. Therefore, the shear crack simulated numerically occurs for a punch displacement which is in agreement with the experimental value (of about 27.4 mm). In both cases (numerically and experimentally), the punch displacement leading to the shear crack is higher than that leading to the bottom crack.

The distribution of the damage parameter d is represented for several punch displacements (20 mm, 25 mm and 28.8 mm just at the final step) and is compared to a photograph of the quasi-fractured specimen in Figure 2.9. The location of the crack is well reproduced by the ML model during the simulation, by comparison with the photograph of the quasi-fractured specimen. Interestingly this location differs from that usually observed for large blanks (bottom crack). Indeed, in the shear crack case the crack initiates at the top of the sheet instead of the bottom. Furthermore, it is remarkable to note that the initiation of the experimental crack, namely in the region of the sheet corner, is also reproduced by the numerical simulation, emphasizing that the numerical calculation is able to predict the experimental cracking behavior.

As in the case of the bottom crack, the distribution of the porosity, which is represented in Figure 2.10 for several punch displacements (20 mm and 28.8 mm), is very similar to that of the damage parameter, but their maximal values are very different (the porosity reaches 0.03 while the damage parameter reaches 0.3). Again, this difference is due to a coupling between void shape effects and coalescence.

The evolution of the total porosity f, second porosity g, nucleated porosity f_{n}, void growth porosity f_{g}, triaxiality T and semi-axes ratios a/c and b/c are represented (versus the punch displacement) in Figure 2.11 in the element that fails first. Before the coalescence occurrence (i.e. for a punch displacement before 18 mm), it is interesting to note that the 'partial porosity' due to void growth (f_{g}) decreases while the 'partial porosity' due to nucleation f_{n} as well as the second porosity g increase, with similar proportions. Therefore, in the case of a shear crack, the model predicts no void growth of initial voids but a small void closure. The increase of the quantity $(f + g)$ is thus solely due to void shape (through g) and void nucleation (through f_{n}). If void nucleation would have been disregarded, the total porosity f would have decreased; in such case, the threshold $(f + g)_c$ can be attained only

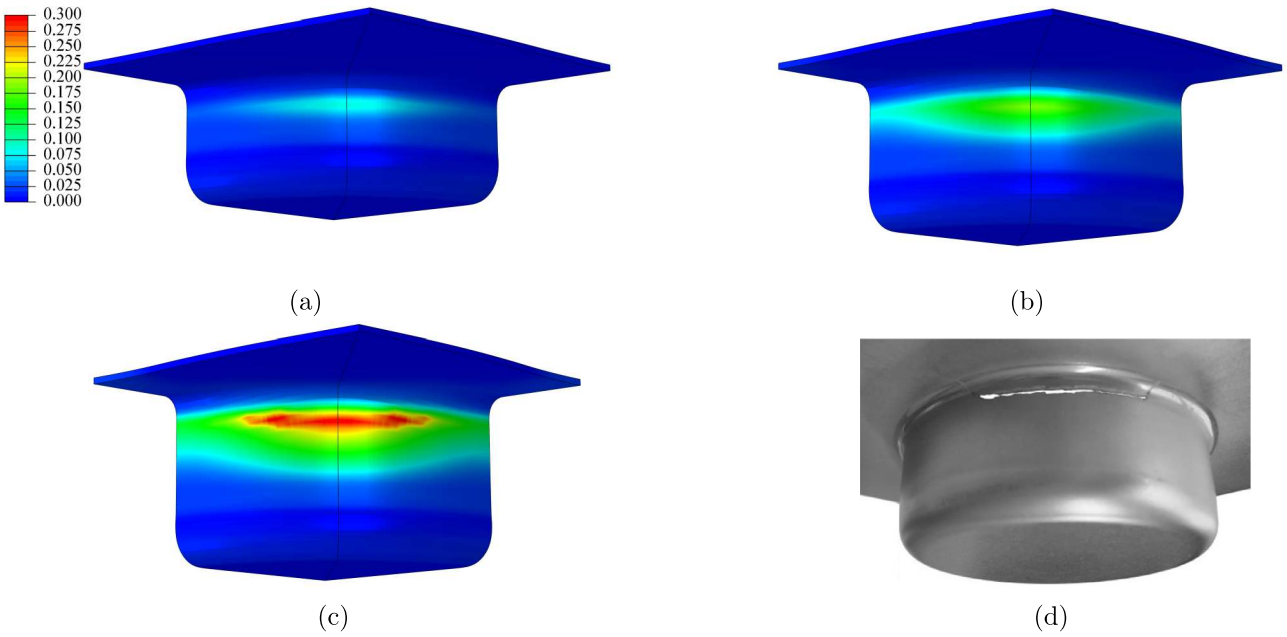

Figure 2.9: Location of the shear crack during deep drawing with a blank size $L = 140$ mm. (a) Distribution of the damage parameter d for a punch displacement of 20 mm, (b) Distribution of the damage parameter d for a punch displacement of 25 mm, (c) Distribution of the damage parameter d for a punch displacement of 28.8 mm (final step of the simulation) and (d) Photograph of the quasi-fractured specimen (after [44]).

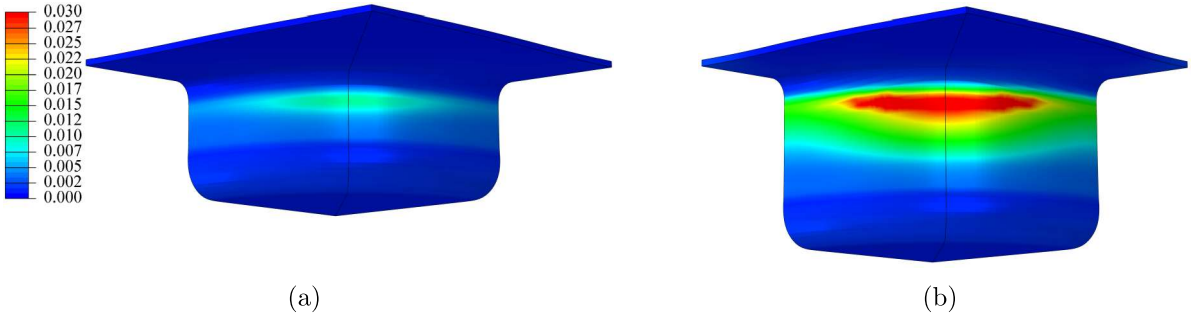

Figure 2.10: Distribution of the porosity f in the simulation of a shear crack during deep drawing with a blank size $L = 140$ mm. (a) Punch displacement of 20 mm and (b) Punch displacement of 28.8 mm.

with an increase of g which corresponds to void shape effects. Here, in the present case, the threshold $(f+g)_c$ is attained due to an increase of both g and f_{n}, but the rate of g is higher than the rate of f_{n}, emphasizing that void shape effects are dominant in this problem and void nucleation plays a minor role. It is worth noting that the stress triaxiality is of about $T \sim 0$ before coalescence, confirming that the local stress state is pure shear (which explains the decrease of the porosity f_{g} due to the sole void

closure mechanism). In that case, important void shape effects are observed, as the void semi-axes ratios reach respectively $a/c \sim 4.25$ and $b/c \sim 2.25$: the cavity has become a general ellipsoidal void with three very different axes $a > b > c$. The predictions of the model are in agreement with the findings of [44] who postulated that the damage mechanism in that case was due to shearing.

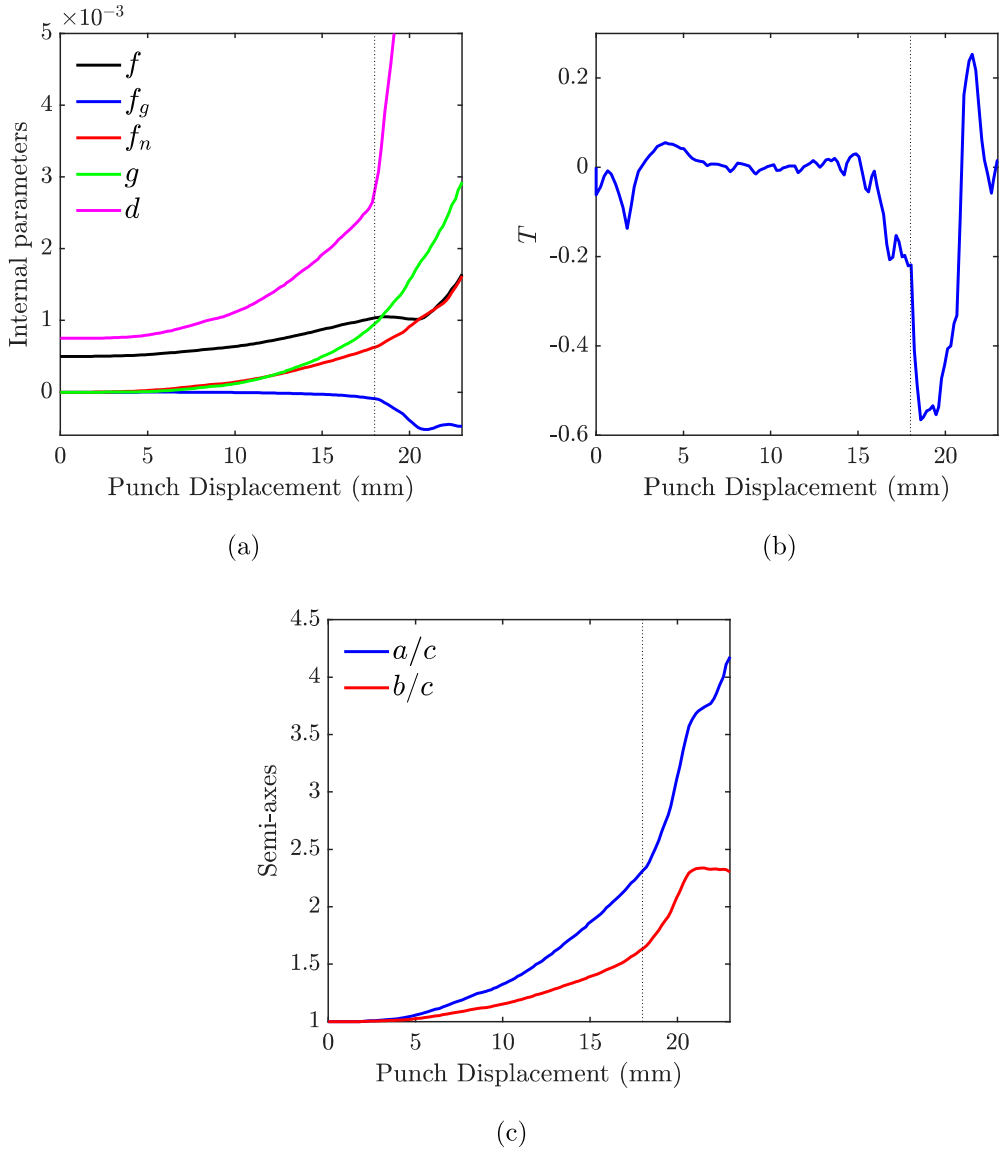

Figure 2.11: Evolution of internal parameters in the element that fails first in the simulation of a shear crack during deep drawing with a blank size $L = 140$ mm. (a) Damage parameter d, total porosity f, second porosity g, porosity due to nucleation f_{nucl} and porosity due to void growth f_{growth}, (b) Stress triaxiality T and (c) Semi-axes a/c and b/c. The onset of coalescence is represented by a dotted vertical line.

Again, it should be also noted that after coalescence the evolution of the internal parameter should be interpreted even more carefully than in the bottom crack case [84]. Indeed after coalescence, when the quantity $(f + g)$ is replaced by $(f + g)^*$, artificial void growth can be observed even during pure shear. This is due to the heuristic model of coalescence of [120], as shown previously by [84].

2.6.2 Comparison with GTN model

The predictions of the ML model are now compared to that of GTN model (without void shape effects), in order to assess the importance of void shape effects on shear-dominated ductile fracture.

First, the set of parameters calibrated for the ML model (see Table 2.3) was found to slightly underestimate ductility during the tensile test. Therefore, an appropriate calibration for GTN model parameters has been performed in order to reproduce accurately the tensile test (see Table 2.4 for the set of parameters and Figure 2.5 for calibration result.).

Table 2.4: Parameters for the GTN model in the case of the AA6016-T4.

	q	f_0	f_c	δ	f_N	ε_N	s_N	d_F
AA6016	1.5	0.0005	0.002	4	0.018	0.9	0.4	0.3

The force-displacement curves of the punch obtained using GTN model are compared to that obtained with the ML model in Figure 2.12, for the two cases considered ($L = 140$ mm and $L = 152$ mm). Before the total failure, the overall behavior is quite similar irrespective of the model used.

In the case of a large blank size ($L = 152$ mm), failure occurs for a displacement of about 23.7 mm using GTN model. (Note that failure occured for a displacement of about 20 mm using the ML model). The distribution of the porosity, for GTN model, is represented in Figure 2.13. For a punch displacement of 20 mm, the damage parameter is not localized yet at the bottom of the specimen but it localizes for a displacement of 23.7 mm. Therefore, GTN model is, as expected, able to predict the bottom crack (as the triaxiality is positive) but it slightly overestimates the ductility as the displacement at failure is higher than that observed experimentally (20.5 mm).

In the case of a small blank size ($L = 140$ mm), there is no failure (at least for the displacements considered) using GTN model while failure was predicted using the ML model for a punch displacement of about 28.8 mm. The distribution of the porosity, for Gurson's model, is represented in Figure 2.14 for two displacements of the punch (28.8 and 35 mm). Using GTN model, the damage parameter

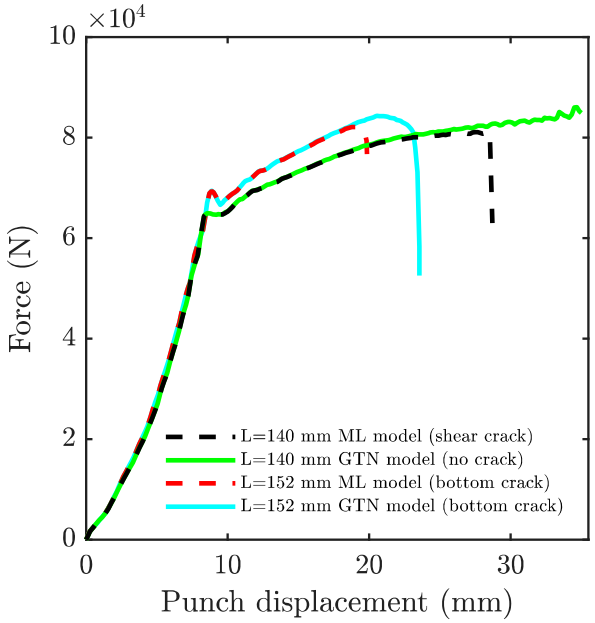

Figure 2.12: Comparison of the punch force-displacement curves using ML and GTN for the two blank sizes considered ($L = 140$ mm and $L = 152$ mm).

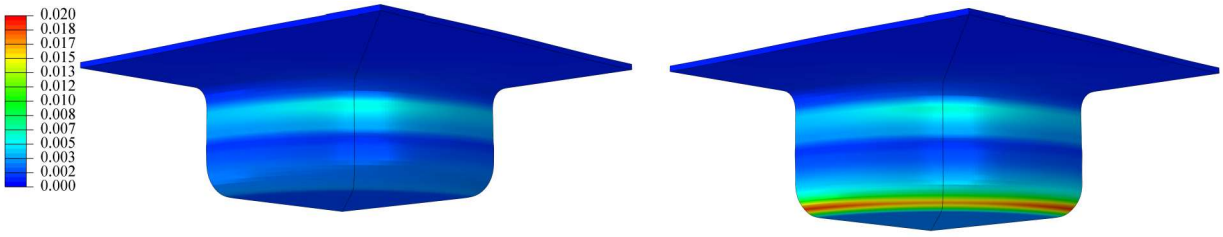

(a) (b)

Figure 2.13: Distribution of the porosity using the GTN model in the simulation of deep drawing with a blank size $L = 152$ mm. (a) Punch displacement of 20 mm and (b) Punch displacement of 23.7 mm.

is not localized in contrast with the ML model which predicts a localization of damage leading to a macroscopic crack. Thus in that case, GTN model is not able to predict the shear crack; this was expected as this model does not predict softening in shear because there is no increase of the porosity (which is the damage parameter in this model) in pure shear.

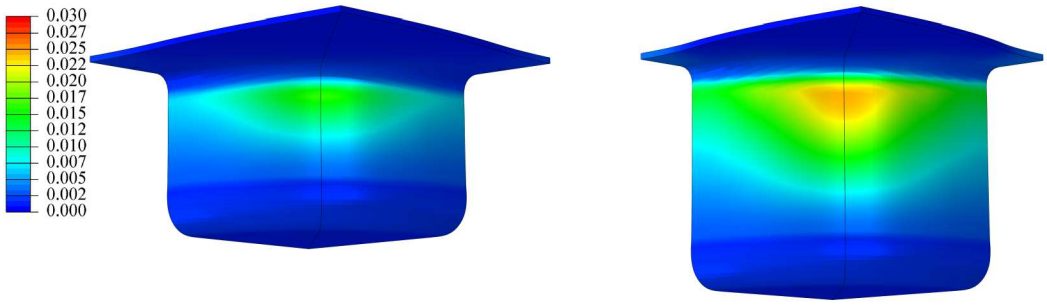

(a) (b)

Figure 2.14: Distribution of the porosity using the GTN model in the simulation of deep drawing with a blank size $L = 140$ mm. (a) Punch displacement of 28.8 mm and (b) Punch displacement of 35 mm.

2.6.3 Discussion

The ML model has permitted to reproduce several macroscopic features observed in forming processes involving complex loading paths with local shear-dominated states. Those results, together with those previously obtained on shear-dominated buterfly specimens [83] and on micromechanical cell calculations [84], confirm the capabilities of the ML model to predict ductile failure at low stress triaxialities in presence of intense shear. Therefore, this model can be considered as an alternative to uncoupled models for the simulation of forming processes because it can predict crack propagation. Indeed, even though uncoupled models are interesting to provide the strain-to-failure [44], this class of models cannot predict crack propagation since they do not take into account the loading history of the damage variables. Furthermore, the ML model can also be considered as a viable micromechanical alternative to Nahshon and Hutchinson [88]'s modification of Gurson's model for the simulation of forming processes. Indeed, even though Nahshon and Hutchinson [88]'s model was successfully applied to the prediction of punch tests [131], this model is based on a heuristic modification of the evolution equation of the porosity, which is not identical to the true volume fraction of the voids, but can be interpreted as a heuristic damage parameter. Consequently, a notable advantage of the ML model is that softening in shear is not due to an artificial increase of the porosity as it is the direct consequence of void shape effects (with possible void closure).

Finally, the evolution of semi-axes in Figures 2.11 and 2.8 has given us some ideas about the average shape of the voids in the fracture area. In the shear crack case, it was observed that the ratio of major to minor semi-axes of the ellipsoidal void reached a very high value, demonstrating elongated

voids in the fracture zone. Additionally, for the bottom crack case, major and moderate semi-axes experience moderate and quite similar increase that corresponds to a oblate spheroidal void shape. These results are consistent with SEM observations of the dimples in the fracture surface presented in Chapter 1 which were obtained from deep drawing experiments on titanium alloy. These experimental observations further confirm the capability of ML model to help access to physical aspects of damage evolution during ductile fracture.

2.7 Conclusion

In this chapter ductile failure in a conventional forming processing was investigated. Experimental results of deep drawing on aluminum alloys have shown that ductile failure in forming processes can be the consequence of shear-dominated loadings. Interestingly, several modes of cracking are observed depending on the blank size and blank-holder force. In order to simulate those experiments, the Madou-Leblond model, which is an extension of GTN model incorporating void shape effects, has been considered. This model permits to reproduce 'bottom cracks' for large blanks and 'shear cracks' for small blanks. The evolution of the internal parameters of the ML model has permitted to highlight the importance of void shape effects upon the final failure. When the triaxiality is low, the porosity decreases but the ratios between the void's semi-axes increase which leads to some softening: indeed in this model, softening can be induced by void shape effects through the second porosity. Finally, comparison with the GTN model shows its difficulty to simulate accurately failure because it generally overestimates ductility since it disregards void shape effects; particularly during low stress triaxiality.

These results are particularly encouraging for the simulation of damage evolution if processes such as severe plastic deformation in which the specimen undergo important shear deformation.

Chapter 3

Analysis of residual stress and shear damage in RCS: A case of severe plastic deformation process

3.1 Resumé en francais

Dans ce chapitre, nous étudierons l'évolution de l'endommagement au cours de l'opération de corrugation et d'aplatissement répétitifs (RCS), un procédé SPD adapté à l'obtention de tôles nanostructurées présenté dans le Chapitre 1. Dans un premier temps, nous ne considérerons qu'une seule passe du procédé. De plus, deux matériaux seront considérés dans nos études : (i) un alliage d'aluminium ductile et (ii) un alliage plus fragile (mais néanmoins ductile). Ceci permettra finalement d'évaluer la simulation numérique dans deux cas distincts, avec et sans endommagement. Enfin, les simulations expérimentales et numériques illustreront l'influence de la ductilité du matériau sur la performance du processus RCS.

Dans le cas d'un matériau ductile (non endommagé), nous utilisons la méthode de diffraction des rayons X pour mesurer les contraintes résiduelles après une passe du processus RCS. Ceci nous aidera à évaluer la validité des simulations numériques. Dans le cas d'un matériau plus fragile, l'évolution de l'endommagement est étudiée à l'aide du modèle ML. Ce chapitre est organisé comme suit :

Dans la Section 3.3, la procédure expérimentale utilisée pour réaliser l'essai RCS et les matériaux utilisés dans le processus RCS sont présentés. De plus, la méthode de diffraction des rayons X et la procédure de reconstruction des contraintes résiduelles sont présentées dans cette section. Ensuite, des simulations numériques sont effectuées pour évaluer l'évolution de l'endommagement et des propriétés

des matériaux pendant et après le processus RCS pour deux cas distincts d'alliages d'aluminium ductiles et fragiles dans les Sections 3.4 et 3.5 respectivement. Ce chapitre se termine par quelques remarques finales dans la Section 3.6.

3.1.1 Procédure expérimentale

Le processus RCS se compose de deux étapes :

1. *Une tôle plate initiale est corruguée à l'aide de deux matrices de corrugation, qui induisent une importante déformation par cisaillement au sein de la tôle. À la fin de cette étape, l'échantillon n'est plus une tôle plate car sa forme est corruguée.*
2. *Ensuite, l'éprouvette corruguée est aplatie à l'aide de deux matrices plate. À la fin de cette étape, le spécimen est à nouveau une tôle plate (voir Figure 3.1).*

Ces deux étapes correspondent à une passe. Comme à la fin d'une passe l'échantillon est plat, l'originalité de ce procédé est qu'il est possible de répéter ces passes afin d'augmenter la déformation plastique, ce qui conduirait à un affinement du grain [35]. Dans ce chapitre, une seule passe de RCS est considérée, ce qui est un premier pas vers la simulation complète de RCS multi-passes avec accumulation d'endommagement d'une passe à l'autre.

La RCS a été réalisée en utilisant un matériau ductile (AA6061-T6) et un matériau fragile (AA 7075-T6). Dans le cas de l'alliage d'aluminium fragile, une fissure en forme de croix est observée pendant l'étape de corrugation dans les motifs proches du centre (voir Figure 3.2). Dans le cas de l'alliage d'aluminium ductile, une seule passe est considérée, c'est-à-dire une corrugation d'une tôle plate initiale suivie d'un aplatissement et les fissures n'apparaissent pas (voir Figure 3.3).

Afin d'effectuer des mesures de DRX, utiles pour valider le modèle numérique, tout d'abord, un motif de la surface de l'échantillon a été électropoli afin d'éliminer les effets de friction de surface. Ensuite, la distribution des contraintes résiduelles est évaluée par des mesures de diffraction des rayons X en utilisant la méthode "psi-tilt". Les valeurs de contraintes résiduelles fournies par la DRX sont une convolution des contraintes résiduelles dans la zone irradiée dont la taille dépend du collimateur. Lorsque la longueur caractéristique du gradient de contrainte est inférieure à la zone irradiée, de forts effets de moyenne sont observés. Afin de déterminer les effets importants du gradient dans la distribution des contraintes résiduelles, une méthode de déconvolution a été développée pour reconstruire la

distribution locale des contraintes résiduelles à partir des mesures moyennes. Les détails de la méthode sont donnés en Annexe B.

3.1.2 Résultats

Dans le cas d'un alliage d'aluminium ductile, nous avons utilisé une méthode de diffraction des rayons X pour valider les résultats obtenus par les simulations. Après avoir utilisé la méthode de déconvolution sur les données expérimentales moyennées, les champs de contraintes résiduelles reconstruits ont montré des améliorations importantes de l'évaluation de l'hétérogénéité et ont fourni de meilleures comparaisons avec les résultats des simulations.

Dans le cas d'un alliage d'aluminium fragile, une fracture a été observée pendant l'étape de corrugation du processus RCS. La simulation utilisant le modèle ML a été capable de reproduire avec précision l'endroit et la forme de la rupture. Dans la zone endommagée, une contribution importante des effets de forme des vides a été observée en plus de la croissance et de la nucléation des vides. La comparaison entre le modèle ML et le modèle GTN a montré un certain retard dans l'apparition de la fissure dans le modèle GTN en raison de la présence d'effets de forme des vides dans le cas d'un matériau fragile et pour des valeurs élevées de déplacement de la matrice corruguée.

Enfin, bien que le modèle GTN ne permette pas de prédire la fissuration induite par le procédé, il a cependant montré qu'il peut être adapté pour décrire l'évolution de l'endommagement lors du procédé RCS avant la rupture finale. En effet pour de faibles déplacements de corrugation, la triaxialité est assez importante (les effets de cisaillements ne se produisent qu'à la fin du procédé). Avec de plus petits déplacements de la matrice corruguée, cette condition est remplie et le modèle GTN est applicable pour la RCS.

Ces résultats constituent une première étape vers la prédiction du comportement mécanique des tôles produites par RCS ; la prochaine étape est de considérer la modélisation des effets d'affinement du grain qui se produisent lorsque RCS est répété afin de simuler les modifications de ductilité et de résistance induites par le procédé.

3.2 Introduction

In this chapter, we will investigate the evolution of damage during repetitive corrugation and straightening (RCS), a SPD process suitable for obtaining nanostructred sheet metals introduced in Chapter 1. In this process, important non-linear effects (such as large deformation and heavy contact conditions) are induced on the material. Hence, we will first consider only one pass of the process. Furthermore, two materials will be considered in our investigations : (i) a ductile aluminum alloy and (ii) a brittle one. This will ultimately permit to asses the numerical simulation in two distinct cases, with and without damage. Finally, experimental and numerical simulations will illustrate the influence of material ductility on performance of the RCS process and evolution of damage.

In the case of the ductile (non-damaged) material, we use X-ray diffraction method to measure the residual stresses after one pass of RCS process. This will help of us asses the validity of numerical simulations. Additionally, as the resolution of diffraction measurement is limited by laboratory equipment, a deconvolution procedure is developed to better exploit the experimental data. The measurements obtained from XRD method will be compared with the results obtained by numerical simulations.

In the case of "*brittle*" material, the damage evolution is investigated using ML model. This chapter is organized as follows :

In Section 3.3, the experimental procedure employed to perform RCS and the materials used in RCS process are introduced. Additionally, X-ray diffraction method and the deconvolution procedure on experimental results are presented in this section. Next, numerical simulations are performed to evaluate the evolution of damage and material properties during and after the RCS process for two distinct cases of ductile and brittle aluminium alloys in sections 3.4 and 3.5 respectively. This chapter is terminated by some concluding remarks in Section 3.6.

3.3 Experimental procedure

3.3.1 Description of RCS experimental set-up

This RCS process consists of two steps:

1. An initial flat sheet is corrugated using two corrugation dies, which induce important shear deformation within the sheet. At the end of this step, the specimen is no longer a sheet as its

shape is corrugated.

2. Then, the corrugated specimen is straightened using two flat straightening dies. At the end of this step, the specimen is again a flat sheet (see Figure 3.1).

These two steps correspond to a pass. Since at the end of a pass the specimen is flat, the originality of this process is that it is possible to repeat these passes in order to increase the plastic deformation, which would lead to grain refinement [35]. In this chapter, only one pass of RCS is considered which is a first step towards the full simulation of multi-pass RCS with accumulating damage from one pass to another. The die profile is based on two perpendicular sinusoidal functions of period 16 mm (see Elizalde et al. [29]) which is suitable for a sheet thickness of about 1 mm (see Figure 3.1), and is composed of 7×7 elementary patterns. The size of the sheet is 120 mm $\times$ 120 mm $\times$ 1 mm. Furthermore, the experiments of RCS have been performed without any lubrication.

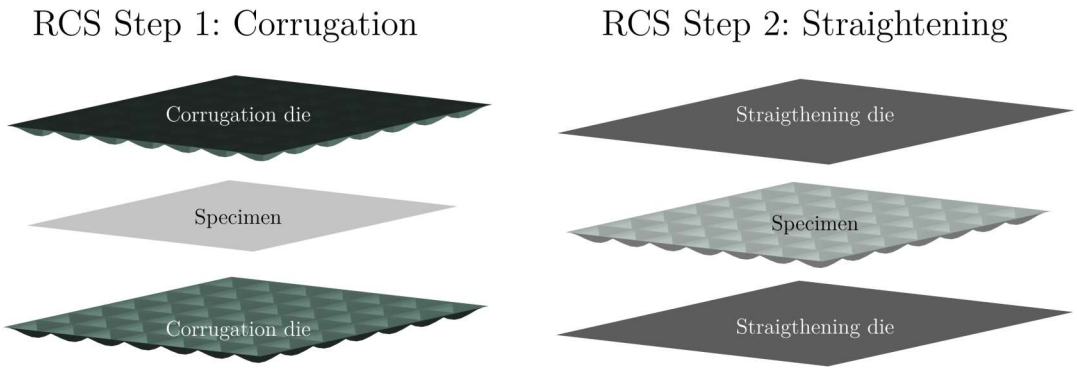

Figure 3.1: Set-up of the RCS experiments.

Tensile tests and RCS process were performed at a deformation speed of 0.5 and 2 mm/min respectively, using an Instron 5500R (10 kN) and an Instron 8802 (25 kN) universal testing machines.

As explained in the introduction of this chapter, the RCS was performed using a ductile (AA6061-T6) and a brittle (AA 7075-T6) material. In the case of the brittle aluminium alloy, a 'cross crack' is observed during the corrugation step in the patterns close to the center (see Figure 3.2). In the case of the ductile aluminum alloy, one pass is considered, that is a corrugation of an initial flat sheet followed by a straightening and cracks did not appear (see Figure 3.3).

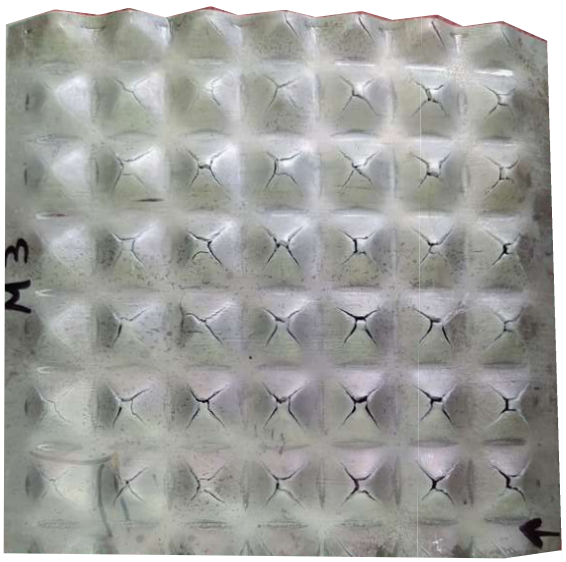

Figure 3.2: Location of cracks observed experimental in repetitive corrugation and straightening experiments (during the first corrugation step of a brittle aluminum alloy (AA7075-T6)).

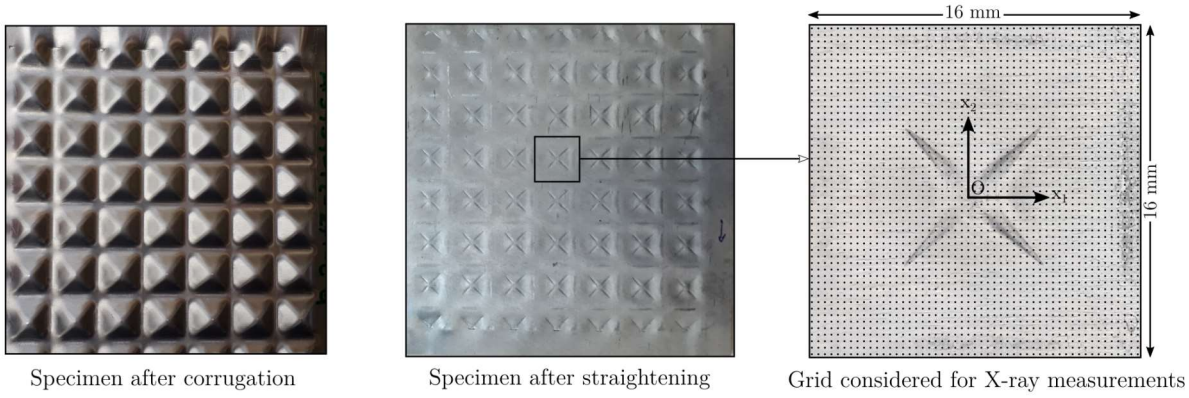

Figure 3.3: Description of the specimen processed by a one pass RCS using a ductile aluminium alloy (AA6061-T6).

3.3.2 Material characterization

3.3.2.1 Ductile Aluminum alloy (AA6061-T6)

First, we consider a precipitation-hardened aluminum alloy 6061-T6. A solid solution heat treatment at 803 K for two hours was applied, then the sample was water-quenched, followed by an aging treatment at 453 K for 18 h [29]. The chemical composition of the Al-6061-T6 alloy is given in Table 3.1.

Table 3.1: Composition of the Al-6061-T6 alloy.

Element	Si	Fe	Cu	Mn	Mg	Cr	Zn	Ti	Al
wt%	0.77	0.24	0.16	0.03	1.03	0.07	0.03	0.02	balance

3.3.2.2 Brittle Aluminum alloy (AA7075-T6)

Next, experiments of repetitive corrugation and straightening have been performed on an aluminum alloy 7075-T6 which is widely used in civil aircraft for its excellent characteristics of specific strength and specific stiffness. Its chemical composition is given in Table 3.2. This Al-7075 alloy was subjected to four-stage heat treatment (T6): heating up to 535°C for 2 hours, water tempering, heating up to 175°C for 18 hours, and air cooling down to room temperature.

Table 3.2: Chemical composition of the Al-7075-T6 alloy.

Element	Si	Fe	Cu	Mn	Mg	Cr	Zn	Ti	Al
wt%	0.23	0.31	1.65	0.22	2.36	0.24	5.72	0.10	balance

3.3.3 XRD measurements

In the case of AA6061-T6, residual stresses are determined in order to asses the numerical simulations of RCS without damage. The residual stress distribution is evaluated on a central pattern located at the bottom surface of a one pass corrugated and straightened specimen (see Figure 3.3), by X-ray diffraction measurements using the psi tilt method and an in-situ diffractometer type X-RAYBOT (manufactured by MRX France). The pattern was electropolished in order to remove surface friction effects using electrolytic polishing machine Struers LectroPol-5 to dissolve a very thin layer from the surface.

Since important gradient effects on the surface are expected in residual stress distribution, a deconvolution method has been developed to reconstruct local distribution of residual stress form the average measurements. Indeed the values of residual stress provided by XRD is a convolution of the residual stresses in the irradiated area whose size depends on the collimator. When the characteristic length of the stress gradient is smaller than the irradiated area, strong averaging effects are observed.

The idea is to solve an inverse problem from the knowledge of the collimator sizes inducing the averaging. The details of the method are given in Appendix B.

The XRD measurements were first performed along a single line on the center of the pattern (the line $x_2 = 0$ in Figure 3.3) with a spatial step 0.32 mm (i.e. 51 points for the reconstructed field). We used two collimators, a smaller one with an irradiated area of diameter 2.5 mm, and a larger one with an irradiated area of size 4.5 mm. The full stress tensor is determined using 13 angles Ψ and 2 angles Φ in order to determine full residual stress tensor (by assuming $\sigma_{33} = \sigma_{12} = 0$).

Next for obtaining a map of distribution of the residual stress, The XRD measurements were performed with a spatial step 0.32 mm so the grid is composed of 51×51 points (i.e. 2601 points for the reconstructed field). We again used the two collimators which permits to provide two average datasets requiring a total of 2906 measurement points. Due to the large number of measurement points required, the XRD measures have been performed using $\Phi = \Psi = 0°$: this permits the determination of the strain ε_{33} which is related to the bi-axial stress $\sigma_h = \sigma_{11} + \sigma_{22}$ at the surface (see Appendix C). In addition, the full stress tensor on several points was determined to find the average of the free-stress interatomic lattice spacing d_0.

It should be noted that the full stress tensor could have been determined for all grid points on the surface but it would have increased by (at least) a factor 25 the experimental time, which was already very important using $\Phi = \Psi = 0°$. The X-ray diffraction conditions are given in Table 3.3.

Table 3.3: Experimental conditions of X-ray diffraction.

Cr-Kα radiation	Voltage	Current	XRD planes	Angle 2θ	Ψ angles
0.2290 nm	20 KV	1 mA	(3 1 1)	139°	1 angle (0°) or 13 angles in $[-37.27°,\ 39.23°]$

3.4 Results I: A case of ductile material

In this section, the results of the simulation of RCS process using a ductile aluminium alloy AA6061-T6 is presented with a focus on deconvolution procedure.

Experimental observations show that in the case of ductile aluminium alloy, cracks are not formed after one pass of corrugation and straightening. Next, the deconvolution procedure is applied to the residual stress measurements obtained by XRD process according to the procedure explained in Section 3.3.3. Finally, the numerical model is implemented in ABAQUS and the experimental results are compared with numerical ones.

3.4.1 Experimental determination of residual stress

Measurement along a single line In the first step, XRD measurements were performed on a single line. Small and large collimator sizes were used with 41 and 37 measurement points respectively. For each measurements points 13 psi and 2 phi angles were selected and 26 measurements were performed to obtain σ_{11} and σ_{22} by neglecting the shear (due to symmetrical nature of the process along the measurement line) and out of plane stresses (due plane-stress condition). Figure 3.4a shows the distribution of measured residual stress along the measurement line using the two collimators. The experimental data have been post-treated in order to enforce symmetry of the die geometry. The collimator size has a great influence in the stress results as it effects the inflection point and stress level (e.g. 100 MPa near the center). The gradient of the measured stress associated with the large collimator are smaller than that associated with the small collimator, which confirms that a strong averaging effect is induced by the measure. Figure 3.4a also shows the stress profile reconstructed from the XRD measurements by the deconvolution method. The reconstructed profile is considerably different from the measured dataset and high stress gradients and inflection points are predicted in contrast with the average datasets.

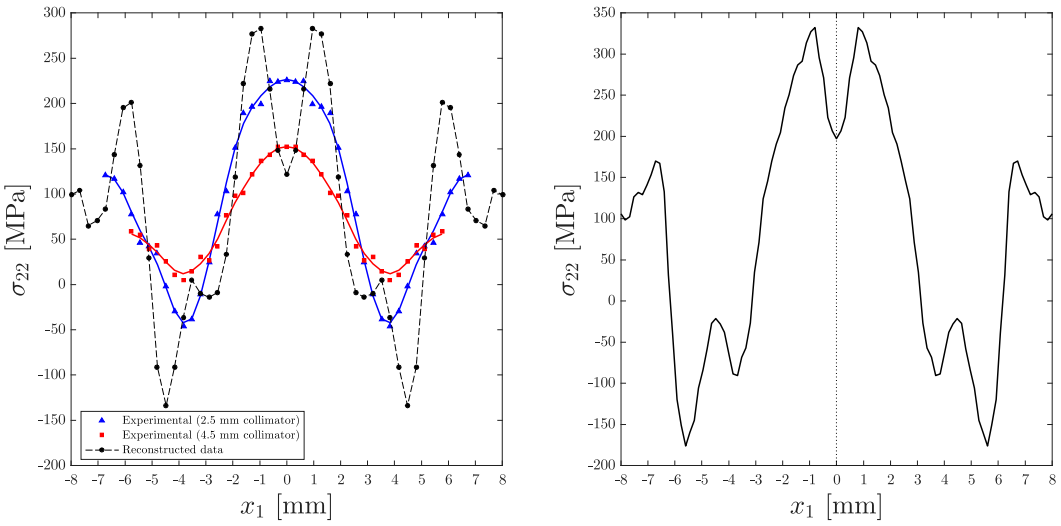

Figure 3.4: (a) Average experimental datasets from XRD measurement and reconstruction of the residual stress σ_{22} by deconvolution method and (b) Spatial distribution of the residual stress σ_{22} on the line $x_2 = 0$ obtained from the numerical simulations.

2D mapping results The two experimental average datasets determined by XRD are shown in

Figures 3.5a and 3.5b. They consist of 41×41 measurement points for the small collimator and 37×37 measurements points for the large collimator. Since the die geometry is symmetric with respect to the x_1-axis, x_2-axis and the 45°-axes, the experimental data have been post-treated in order to enforce these symmetries, which allows the reduction of the experimental uncertainties. The effect of the collimator size is quite notable in terms of distribution and stress levels. For the small collimator, the stress σ_h is in the interval $[-180, -13]$ MPa and for the large collimator, the stress σ_h is in the interval $[-147, -44]$ MPa. Therefore, the stress gradients associated with the large collimator are smaller than that associated with the small collimator, which confirms that a notable averaging effect is induced by the measure.

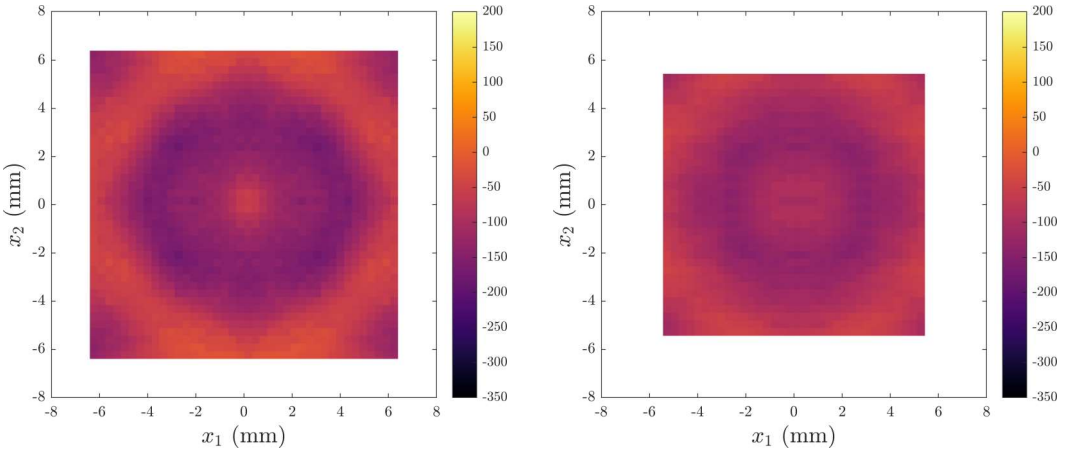

Figure 3.5: Distribution of the residual stress $\sigma_h = \sigma_{11} + \sigma_{22}$ (in MPa) determined experimentally by XRD. (a) Experimental results with a small collimator and (b) Experimental results with a large collimator.

The residual stress distribution reconstructed using 2D deconvolution method is represented in Figure 3.6a. The reconstructed distribution is considerably different from the average datasets collected experimentally. Very high stress gradients are predicted and some 'star' shape in the area deformed by the corrugated die are notably observed. In terms of stress levels, the stress σ_h is in the interval $[-415, 195]$ MPa. It is thus interesting to note that, in several areas, tensile stresses are observed on the reconstructed stress field while only compressive stresses were observed on the average datasets.

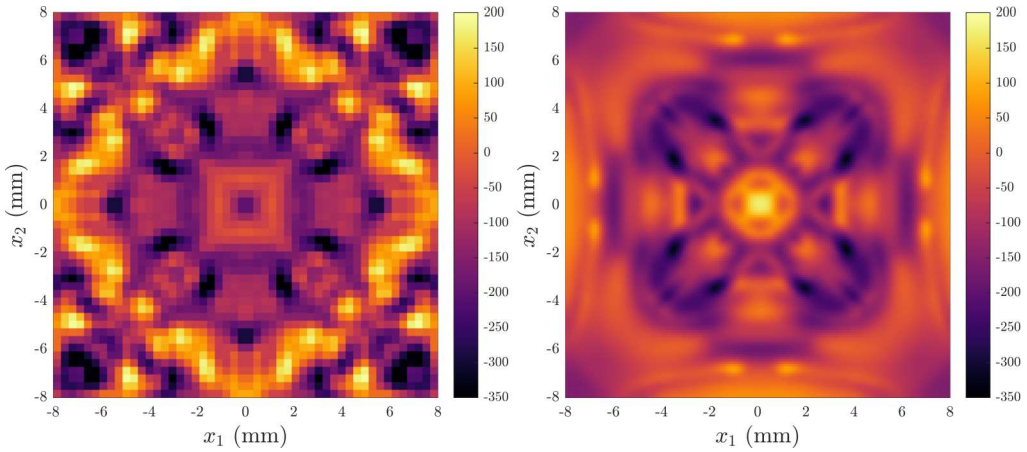

Figure 3.6: Results of reconstructed residual stress distribution $\sigma_h = \sigma_{11} + \sigma_{22}$ (in MPa) from experimental XRD measurements: (a) Reconstructed field and (b) Reference solution from simulation (for comparison).

3.4.2 Numerical results

Numerical model We consider the two steps of the first pass of the process, consisting of one corrugation followed by a straightening, following the conditions given in Ezequiel et al. [35]. The die profile is identical to the experimental geometry so the size of an elementary pattern is $16 \times 16 \times 1$ mm (see Elizalde et al. [29]).

We consider only one elementary pattern subjected to "symmetric-periodic" boundary conditions. The choice comes from a preliminary work presented in Appendix A, on model reduction by comparing the numerical results of a single pattern and a multi-pattern model in order to find the best boundary conditions for the single-pattern model. As shown in Appendix A, the multi-pattern RCS process can be simulated using a single pattern with appropriate boundary conditions, which is representative of the central patterns (see Figure 3.3). Furthermore, due to the symmetry of the process within one pattern, only $1/4^{\text{th}}$ of the pattern is meshed and symmetric boundary conditions are applied in the middle of the model; a sketch of the mesh and the applied boundary conditions are represented in Figure 3.8. The corrugation dies and straightening plates are rigid and the sheet is deformable. The mesh is composed of 11,664 linear R3D8 elements for each straightening plate, 13,568 R3D8 elements for each corrugation die and 256,000 C3D8R elements for the sheet. The size of an element in the sheet is $0.1 \times 0.1 \times 0.1$ mm.

In terms of material modelling we consider the case of a precipitation-hardened aluminum alloy

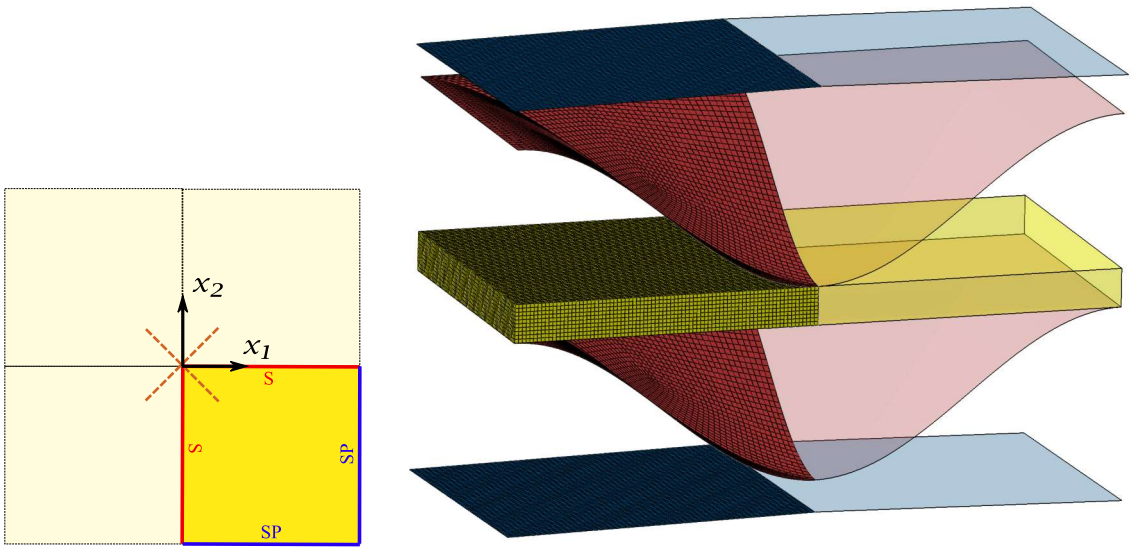

(a) (b)

Figure 3.7: (a) The boundary conditions applied to the $1/4^{\text{th}}$ sheet metal model. SP corresponds to "Symmetric-Periodic" and S corresponds to "Symmetric" (see Appendix A). (b) The mesh considered in the simulations. Half of the experimental model is shown as transparent parts and only $1/4^{\text{th}}$ of the model is meshed. The sheet is shown in yellow, the corrugation dies in red and the straightening dies in blue.

6061-T6 whose behavior follows a power-law isotropic hardening; the yield stress σ_Y is given by

$$\sigma_Y = (\sigma_0 + hp^n)\,, \tag{3.1}$$

where σ_0 is the initial yield stress, h the hardening modulus, n the hardening exponent and p the accumulated plastic strain. The material constants are given in Table 3.4. The contact between the dies and the test sample is supposed to follow a Coulomb model. The value $\mu = 0.25$ is chosen for the friction coefficient, which is typical for the aluminum-steel pair [35].

Table 3.4: Material parameters for the 6061-T6 aluminum alloy used for RCS simulation.

Material	E (GPa)	ν	σ_0 (MPa)	h (MPa)	n
AA 6061-T6	69	0.33	160	170	0.3

Numerical results along a single line In Figure 3.4b the distribution of stress from the numerical simulations is presented. By comparing Figure 3.4a and Figure 3.4b we can see that the reconstructed stress profile as well as the average datasets are very similar to the local stress simulated numerically in similar conditions. In particular, the shape of the profile of the local stress corresponds qualitatively

to that simulated numerically, with the same exact location of inflection points. In the next step, we will try to validate the numerical results by comparing them with XRD measurements on the surface of the specimen instead of a single line.

Surface distribution results Figure 3.6b shows the simulated results of the distribution of residual stress σ_h after one pass of RCS process. Strong heterogeneity was observed after each step of RCS processes, particularly after the straightening step. Interestingly, the distribution of the reconstructed stress field has similar features with that calculated numerically in Figure 3.6b, although they do not coincide exactly. In the numerical simulation, the intervals of values for the stresses are $[-321, 173]$ MPa for the reference distribution, $[-168, 9]$ MPa for the calculated small colimator average dataset and $[-125, -58]$ MPa for the large colimator average dataset. Very similar trends are observed between the experimental and numerical results in terms of distribution and magnitude of the local stress distributions as well as the average datasets, so it can be expected that the reconstructed experimental stress mapping is closer to the 'real' distribution than the average datasets. Hence, it can be reasonably assumed that the 'real' residual stress distribution is (i) significantly more heterogeneous than what we measured with the small and large collimators and (ii) has significant higher compressive stresses and important *tensile* stress.

3.4.3 Discussion

The local stress field reconstructed using the datasets collected from X-ray diffraction measurements with two collimators is very different than the two experimental datasets, which confirms that X-ray diffraction measurements induce strong averaging effects due to the presence of high surface stress gradients. In particular, in the 2D case, high tensile stresses of about 195 MPa are observed on the reconstructed field, while the maximum values obtained experimentally are -13 MPa using the small collimator and -43 MPa using the large collimator. Moreover, since the distribution of experimental stress field reconstructed resembles that calculated numerically in similar processing conditions, it can be assumed that the 2D deconvolution method proposed in this paper has captured the essential features of the stress distribution. For the 2D problem, the raw XRD measurements only provide compressive stresses, which seems unrealistic as tensile stresses were also predicted numerically. The comparison between numerical and experimental results is quite satisfactory even for a quantity (residual stress) which is very sensitive to small modification of the process parameters.

It should be noted that some small differences are still observed between the distribution of the numerical stress distribution and the experimental reconstructed one. Indeed, the numerical simulation of RCS has been performed with values of parameters that are difficult to measure experimentally, such as the friction coefficient and the applied forces of straightening plates. It should also be mentioned that the method presented in Appendix C for measuring ε_{33} from one single diffraction angle is very sensitive to geometrical effects and surface topology; hence some discrepancies in the experimental results were expected. On the other hand, better results were obtained compared with simulations, by applying the deconvolution method on the full-stress tensor measurement along the line.

It can be concluded that the single-pattern numerical model developed permits to reproduce quite accurately the mechanical fields of the RCS process. Therefore this numerical model can be used in a more complex situation, including damage for instance.

3.5 Results II: A case of brittle aluminium alloy

In this section, the simulation of RCS process using a brittle aluminium alloy (AA7075) is presented. Experimental RCS using this alloy has led to fracture during the corrugation step. In this part, we closely analyze the evolution of damage using the ML model.

3.5.1 Numerical model

A 3D finite element model of the repetitive corrugation and straightening processing has been made using the commercial code ABAQUS/Standard. As in the previous case, following the approach introduced in Appendix A, the simulation of multi-pattern RCS can be performed on a single elementary pattern subjected to symmetric boundary conditions on its lateral edges (see Figure 3.8). Furthermore, due to the symmetry of the process within one pattern, only $1/8^{\text{th}}$ of the pattern is meshed and symmetric boundary conditions are applied in the middle of the model; a sketch of the mesh is represented in Figure 3.9. It should be mentioned that since in this case (damaged brittle aluminium alloy), XRD measurements are not performed, we do not need to create the same numerical model as the case of undamaged ductile material. In the former case, fully structured mesh was created for the $1/4^{\text{th}}$ model for facilitating the deconvolution procedure.

The sheet metal is modelled as a 3D deformable part and the mesh is composed of 20288 elements

and 23823 nodes; we use selectively subintegrated 8-node trilinear brick (C3D8 elements in ABAQUS) which are suitable for quasi-incompressible plasticity. The mesh contains 10 elements in the sheet thickness. The corrugation and straightening dies are modeled as rigid 3D shells and are meshed with 1039 and 958 R3D4 elements respectively. Contact conditions are considered between the sheet and the rigid parts using a Coulomb friction model, with a value of 0.25 for the friction coefficient (see [35]). It should be noted that, as explained in Section 3.3, failure occurs during the corrugation step for this material, so the straightening step is not reached in the simulations.

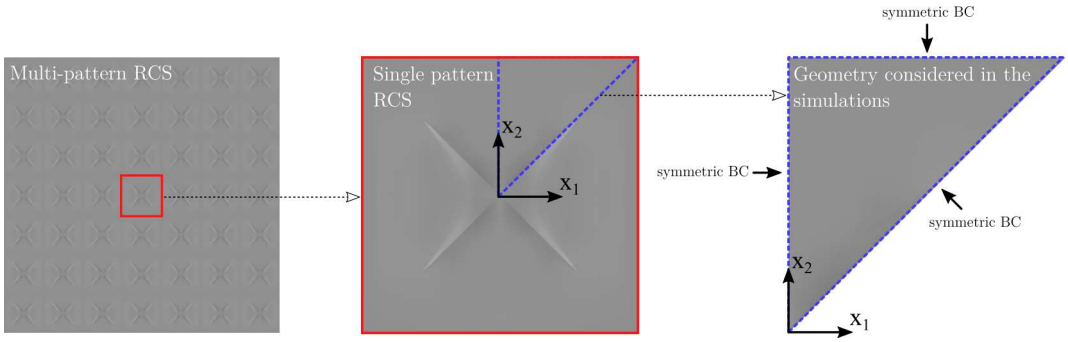

Figure 3.8: Geometry considered in the simulations of RCS.

3.5.2 Parameter Identification

Recent experimental works have shown that aluminum alloys 7075 exhibit a moderate anisotropy [95]; therefore as a first approximation we assume that its behavior is isotropic and the hardening behavior follows a Swift law:

$$\sigma(\varepsilon) = A(\varepsilon_0 + \bar{\varepsilon})^n \tag{3.2}$$

where the parameters A and ε_0 have been calibrated using a tensile test (see also [130] for a similar calibration) and are provided in Table 3.5.

Table 3.5: Swift hardening law parameters for the AA7075-T6.

Material	A [MPa]	n	ε_0
AA7075-T6	673.85	0.1529	0.0075

Then, one needs to calibrate the parameters related to damage. Accordingly, several simulations of the tensile test were performed in order to find the set of parameters that reproduces at best the experimental tensile test. The calibrated set of parameters is given in Table 3.6. In this case, the ratio

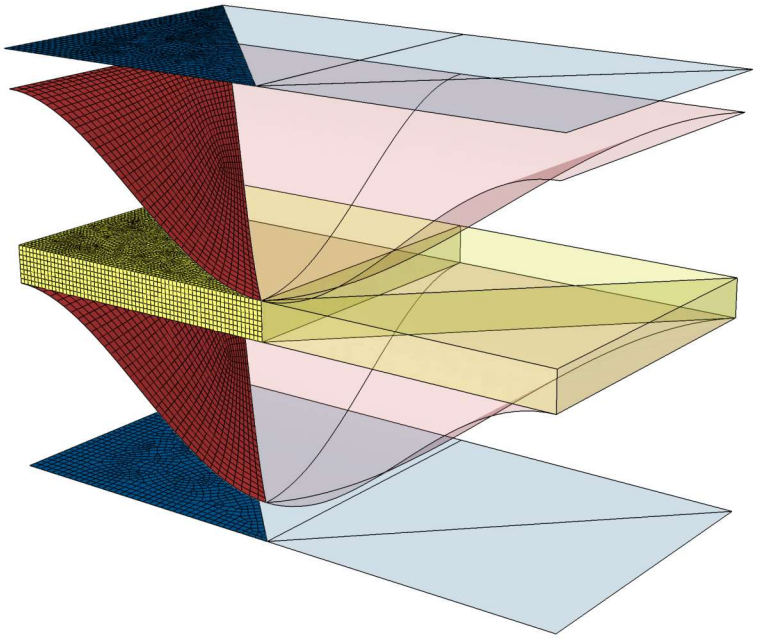

Figure 3.9: Mesh considered in the simulations of RCS. Half of the experimental model is shown as transparent parts and only $1/8^{\text{th}}$ of the model is meshed. The sheet is shown in yellow, the corrugation dies in red and the straightening dies in blue.

$(f+g)_c/f_0$ (equal to 4) and the value of δ are in agreement with the results obtained in [84].

Table 3.6: Parameters for the model ML in the case of the AA7075-T6.

	q	f_0	$(f+g)_c$	δ	f_N	ε_N	s_N	d_F	$(P_0)_{ij}$
AA7075	1.5	0.0005	0.005	4	0.01	0.6	0.2	0.3	δ_{ij}

The experimental stress-strain curve of the aluminum alloy 7075-T6 is compared to the predictions of the model (using the calibrated parameters) in Figure 3.10. Overall, a good agreement is observed between the experimental stress-strain curves and the numerical ones produced with both ML and GTN models.

3.5.3 Numerical results

The numerical simulation ends at a die displacement of about 3.3 mm, due to a numerical instability (the slope of the force-displacement curve becomes vertical). The crack simulated numerically thus occurs for a die displacement which is in agreement with the experimental value (of about 3.2 mm).

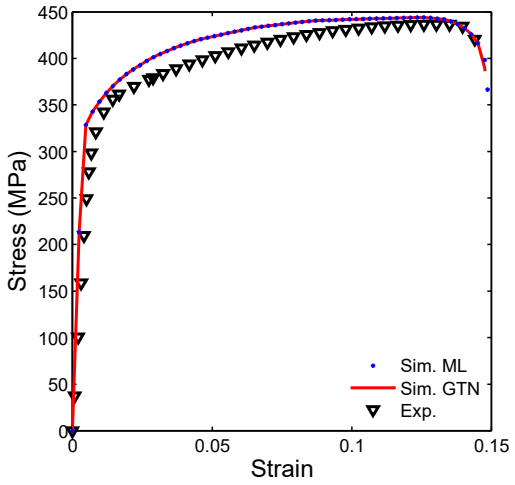

Figure 3.10: Experimental and numerical stress-strain curves of the aluminum alloy 7075-T6 used in the corrugation experiments.

Then, the distribution of the damage parameter d is represented for several displacements of the corrugation die (2.8 mm, 3 mm and 3.3 mm which is the end of the simulation), and is compared to the fractured specimen in Figure 3.11. Overall, the location of the crack and its 'cross' shape are well reproduced by the ML model during the simulation of RCS, by comparison with the photograph of the quasi-fractured specimen (taken on a pattern far from the boundaries). In the simulation, the damage parameter becomes localized with very high values (higher than 0.2) for a displacement of about 3.3 mm which is in agreement with the experimental values.

In addition, the distribution of the porosity is represented in Figure 3.12 for two displacements of the corrugation die (3 mm and 3.3 mm). It is localized in the same regions as the damage parameter but its maximal value is of about 0.02, which is ten times lower than the damage parameter. As in the case of deep drawing, from the definition of the damage parameter, this difference can be attributed by two factors, void shape effects and/or coalescence.

Then, the evolution of the total porosity f, second porosity g, nucleated porosity f_{n}, void growth porosity f_{g}, stress triaxiality T and semi-axes ratios a/c and b/c are represented (versus the punch displacement) in Figure 3.13 in the element that fails first, in order to understand the effect of each mechanism on the failure. Before that coalescence occurs (for a corrugation die displacement lower than 2.7 mm), the porosity due to void growth (f_{g}) decreases while the porosity due to void nucleation (f_{n})

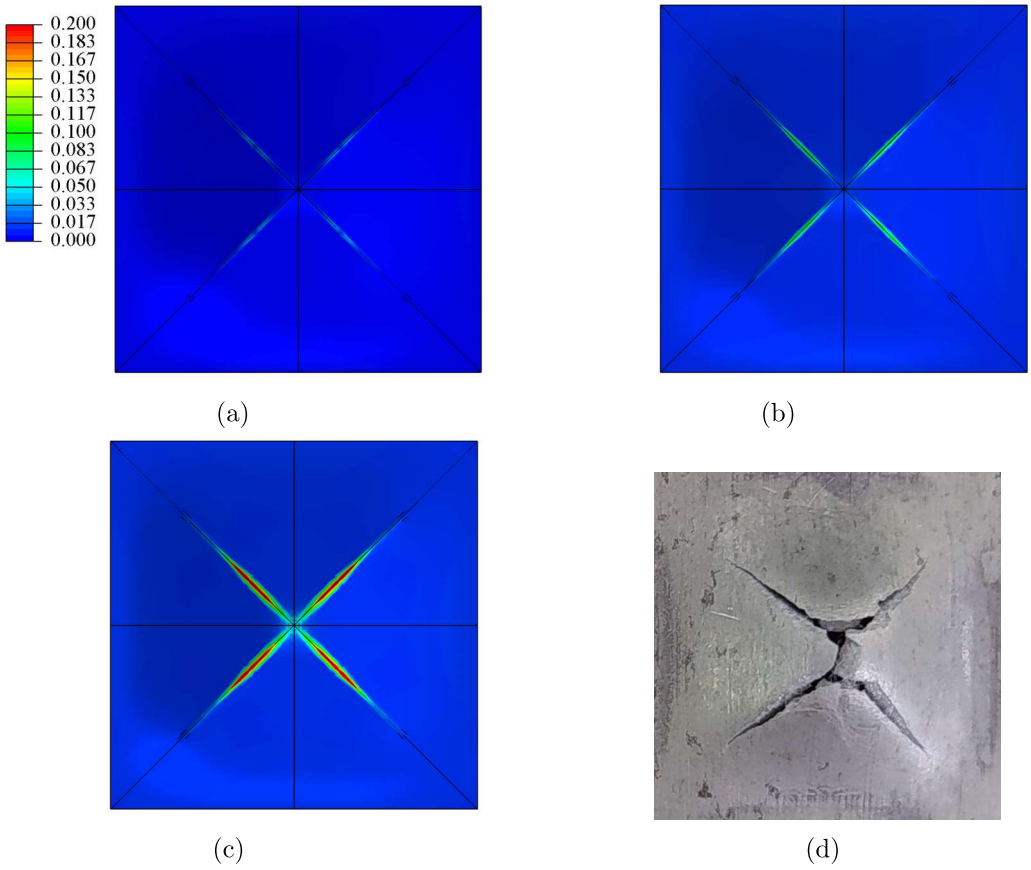

Figure 3.11: Location of the 'cross-shaped' crack in the RCS process. (a) Distribution of the damage parameter d for a die displacement of 2.8 mm, (b) Distribution of the damage parameter d for a die displacement of 3 mm, (c) Distribution of the damage parameter d for a die displacement of 3.3 mm (final step of the simulation) and (d) Photograph of the cross-shaped crack (on one motif) of the quasi-fractured multi-motif specimen (after a displacement of 3.2 mm).

increases; before a die displacement of 2 mm, the total porosity is almost constant and then it slightly increases due to void nucleation. The second porosity (g), related to void shape effects, increases with a rate similar to the total porosity. Therefore, in the case of RCS, the ML model predicts no void growth, and the increase of the quantity $(f + g)$ is mainly due to void shape effects (through g) and void nucleation (through f_{n}). The stress triaxiality T is negative before coalescence which explains void closure. As shown in Figure 3.13c, important void shape effects are associated with the increase of the second porosity; before coalescence, the maximal values for the semi axes are of about $a/c \sim 3$ and $b/c \sim 2$. The initial spherical void thus becomes a general ellipsoidal cavity. It must be noted that the element which fails first is located under the upper side of the pointy edge of the corrugation die; hence during the beginning of the process (before 1.5 mm of die displacement) it is slightly deformed.

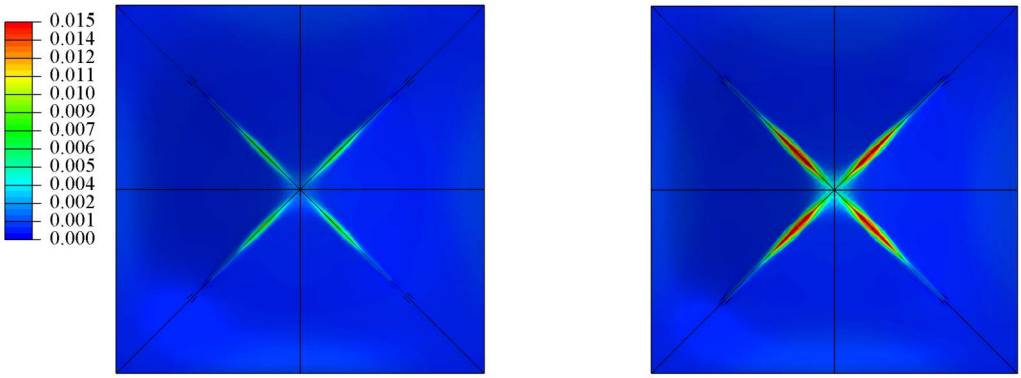

(a) (b)

Figure 3.12: Distribution of the porosity f in the simulation of RCS process. (a) Die displacement of 3 mm and (b) Die displacement of 3.3 mm.

This explains why the internal parameters do not evolve much before a displacement of 1.5 mm.

3.5.4 Comparison with GTN model

The simulation of the RCS process is now investigated using GTN model without void shape effects. In that case, the same set of parameters (see Table 3.6) was used because it was found to reproduce accurately the tensile test using the GTN model.

The force-displacement curves of the corrugation die using GTN model are compared to that obtained with ML model and to the experimental results, in Figure 3.14. Overall, the force-displacement curve is very similar using both GTN and ML models before the occurrence of softening. The fracture happens for a displacement of about 3.7 mm using the GTN model but in this case the numerical instability is not associated with a macroscopic softening on the force-displacement curve.

The distribution of the porosity is represented in Figure 3.15 for two values of the corrugation die displacement (3.3 mm and 3.8 mm). At a displacement of 3.3 mm (for which failure is observed experimentally) the distribution of the porosity follows the 'cross-shape' but it is not localized enough to trigger macroscopic softening. Then, at a displacement of about 3.8 mm (for which the simulation stops due to numerical instability), the distribution of the porosity in that case is similar to the shape of the crack in the experiments. The maximum level of the porosity is about 0.055 which approximately corresponds to $f^* \approx 0.3$.

Therefore, given that the displacement leading to failure is overestimated, it cannot be concluded

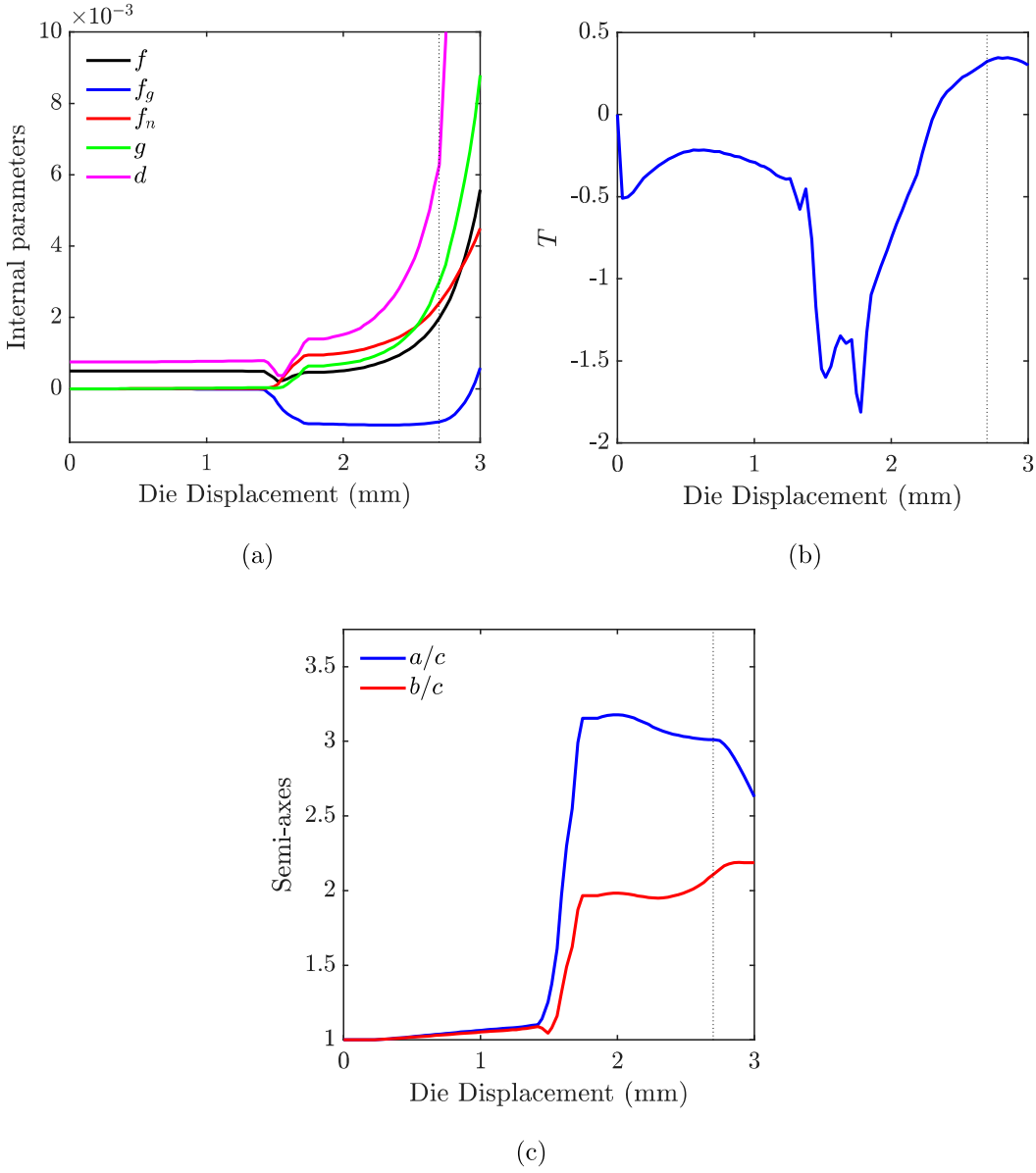

Figure 3.13: Evolution of internal parameters in the integration point that fails first in the simulation of RCS process. (a) Damage parameter d, total porosity f, second porosity g, porosity due to nucleation f_{nucl} and porosity due to void growth f_{growth}, (b) Stress triaxiality T and (c) Semi-axes a/c and b/c.

that failure is quantitatively predicted using GTN model for brittle materials and for high corrugation displacement. Nonetheless, the GTN model can be considered as sufficient to describe approximately the evolution of damage during RCS, before the total failure. Indeed, in contrast to the case of shear cracks during deep drawing in which the crack was located it areas at very low stress triaxiality (with

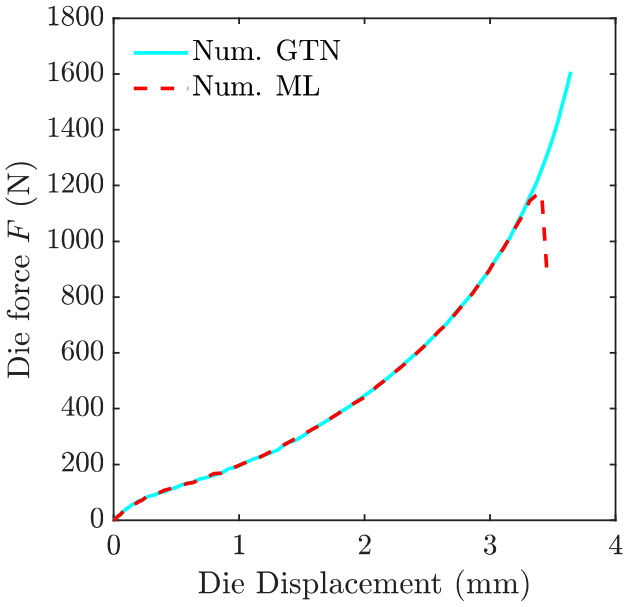

Figure 3.14: Comparison of the die force-displacement curves using ML and GTN in the case of RCS.

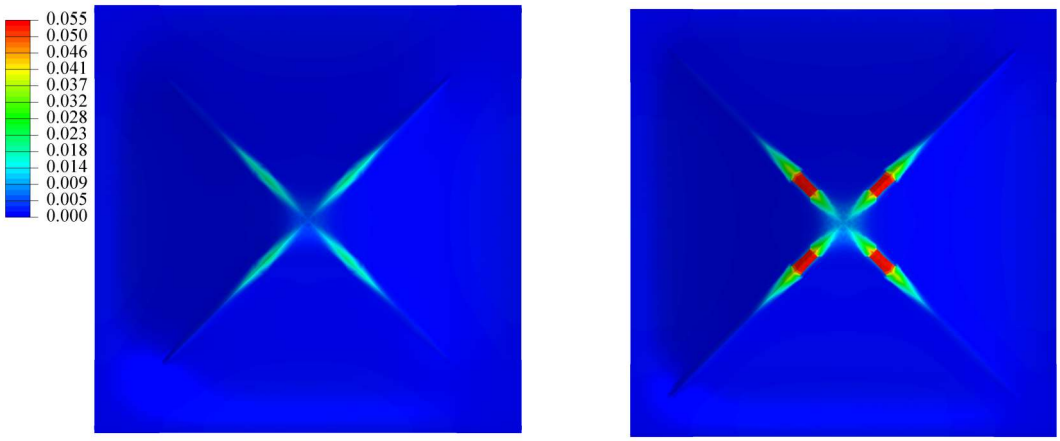

(a) (b)

Figure 3.15: Distribution of the porosity using the GTN model in the simulation of the RCS process. (a) Die displacement of 3.3 mm and (b) Die displacement of 3.8 mm.

almost no void growth), the triaxiality is high during the most part of the simulation of RCS (see Figure 3.16). The triaxiality becomes small only at the very end of the process due to important shear. Therefore, the GTN model can be considered as relevant for RCS to describe void growth during the process, but it will general overestimate failure during the process when shear-dominated

loadings occur.

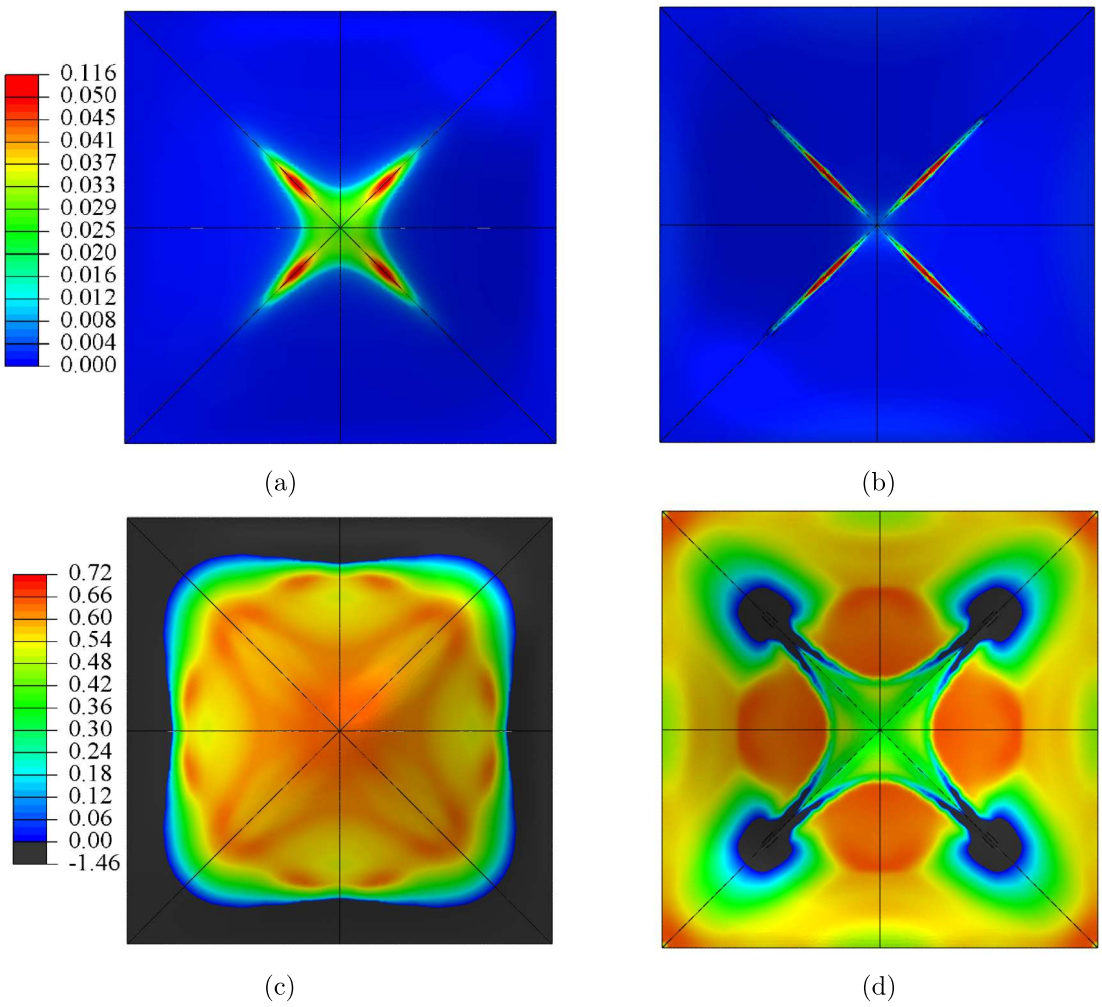

Figure 3.16: Distribution of damage and triaxiality at front and back side of the RCS specimen before fracture showing the contribution of high triaxiality stress condition on evolution of damage. (a) Damage parameter d at back side, (b) Damage parameter d at front side, (c) Triaxiality T at back side and (d) Triaxiality T at front side.

3.6 Conclusion

In this chapter, simulations of one pass of RCS process, which is a SPD process that could be used to produce nanostructured sheet metals, was performed. We considered two distinct cases of ductile (AA6061-T6) and brittle (AA7075-T6) aluminum alloys. In the first case, no fracture was observed and we used a X-ray diffraction method to validate the results obtained by simulations. The experimental

results using different collimators showed strong averaging effects. In order to handle these effects, a deconvolution method on averaged experimental data was performed and the reconstructed residual stress fields showed very important improvements in the evaluation of heterogeneity and provided better comparisons with the simulation results.

In the case of brittle aluminum alloy, fracture was observed during the corrugation step of the RCS process. Simulation using ML model were able to reproduce accurately the occurrence and shape of the failure. In the damaged zone, important contribution of void shape effects was observed in addition to growth and nucleation of voids. The comparison of ML and GTN model showed some delay in the occurrence of crack in GTN model due to presence of high void-shape effects in the case of brittle material and for high values of corrugation die displacement.

Finally, GTN model was found to be able to capture the evolution of damage during most of the RCS process. However this model cannot capture accurately the occurrence of failure in RCS because of the presence of shear-dominated loadings when the corrugation displacement is important. When the corrugation die displacement is moderate, the GTN model is admissible to capture the evolution of damage.

These results constitute a first step towards the prediction of the mechanical behavior of sheets produced by RCS; the next step is to consider the modelling of grain refinement effects that occur when RCS is repeated in order to ultimately simulate the emergent strength and ductility of processed sheets.

Chapter 4

Development of an extended Gurson-type model including hardening based on dislocation density evolution: Application to multi-pass severe plastic deformation

4.1 Resumé en francais

Dans le Chapitre 3, nous avons analysé la première passe du processus RCS et il a été observé que pour des déplacements modérés de corrugation, les effets de la forme des vides peuvent être négligés et que le modèle GTN semble être approprié pour décrire l'évolution de l'endommagement. Dans ce chapitre, nous allons poursuivre le développement et considérer deux passes du processus RCS. La seconde passe induira une déformation plastique supplémentaire, ce qui nécessite de considérer un modèle de durcissement avancé, adapté aux matériaux traités par SPD. Par conséquent, un modèle de Gurson étendu, incluant une description de l'évolution des densités de dislocations et de la structure cellulaire des dislocations, comme origine du durcissement, sera développé et implémenté dans ABAQUS sous la forme d'une routine (UMAT). Ce chapitre est organisé de la façon suivante :

Tout d'abord, les procédures expérimentales réalisées pour le processus RCS à deux passes sont présentées dans le cas d'un échantillon de cuivre pur. Ensuite, un modèle de Gurson étendu incluant l'évolution de densités de dislocations est développé et implémenté numériquement. Ses paramètres sont calibrés en utilisant un essai de traction sur un cuivre pur. La première application du modèle concerne l'étude de l'affinement du grain dans un exemple de chargement proportionnel axisymétrique,

qui permet d'étudier l'affinement maximal du grain en fonction de la triaxialité et de la porosité initiale. Enfin, le modèle est appliqué à la prédiction de la résistance et de la ductilité d'une éprouvette traitée par RCS après deux passes.

4.1.1 Procédures expérimentales

Le matériau utilisé dans ce chapitre est un cuivre pur à $99,9\%$*. Il a été choisi parce que (i) il a une ductilité élevée et (ii) il a été largement utilisé dans plusieurs processus SPD [32, 123, 133] ce qui en fait un bon candidat pour étudier l'évolution du couple résistance-ductilité.*

Le procédé RCS est appliqué à l'échantillon de cuivre de manière similaire à la procédure présentée dans le Chapitre 3. Nous rappelons qu'une passe correspond à une corrugation suivie d'un aplatissement. Pour la première passe, des matrices de corrugation et d'aplatissement sont utilisées sur l'échantillon de tôle initial. Pour la deuxième passe, l'échantillon est déplacé d'une distance égale à la moitié de la période de corrugation (8 mm) dans les directions $x-$ *et* $y-$*, comme le montre la Figure 4.1. Cela permet d'augmenter l'homogénéité de l'état mécaniques (qui est très hétérogène après la première passe).*

Avant le processus RCS et après la passe 2, des tests de traction sont effectués afin d'étudier l'effet du processus sur le compromis résistance-ductilité.

4.1.2 Un modèle de Gurson étendu incluant l'évolution de la densité des dislocations

Afin d'évaluer l'effet du durcissement, de l'affinement du grain et de l'endommagement ductile pendant la SPD, une extension du modèle d'endommagement micromécanique de Gurson [47] est proposée, basée sur l'évolution des structures cellulaires des dislocations dans la matrice entourant le vide. Ce modèle de durcissement sera adapté du modèle composite développé par Estrin et al. [33] et décrit dans la Section 1.4 du Chapitre 1.

Suivant l'approche de Gurson, le durcissement est considéré en supposant que la dissipation plastique dans le volume élémentaire représentatif est égale à la dissipation plastique dans un "matériau équivalent" fictif ayant la même fraction volumique de porosité ($\boldsymbol{\sigma} : \boldsymbol{D}^p = (1-f)\bar{\sigma}\dot{\bar{\varepsilon}}$*), et la limite d'élasticité* $\bar{\sigma}$ *est une fonction non linéaire de la déformation équivalente* $\bar{\varepsilon}$*, qui sera décrite par un modèle basé sur la densité de dislocation.*

Afin de prendre en compte les déformations plastiques sévères (et leurs conséquences sur l'affinement du grain), un modèle de durcissement basé sur les dislocations et le travail d'Estrin et al. [33], est considéré. L'avantage de cette modélisation est qu'elle peut rendre compte de toutes les étapes du durcissement.

Dans ce modèle, la contrainte de cisaillement résolue équivalente τ dépend de la contrainte de cisaillement résolue dans chaque phase (désignée par τ_w dans les parois et τ_i à l'intérieur de la cellule) en utilisant une loi des mélanges ($\tau = v_w\tau_w + v_i\tau_i$). En utilisant le facteur de Taylor M, la limite d'élasticité $\bar{\sigma}$ utilisée dans le modèle de Gurson peut être exprimée en termes de contrainte de cisaillement résolue critique équivalente.

Dans l'hypothèse de chargements quasi-statiques, l'équation d'évolution des densités de dislocation ρ_w et ρ_i peut alors être écrite en fonction de la déformation équivalente $\bar{\varepsilon}$ (voir Eq. 4.11).

Pour l'implémentation numérique du modèle, nous nous concentrons sur l'étape locale de la solution élastoplastique qui consiste à projeter le prédicteur de contrainte élastique sur la surface d'écoulement (voir la Section 4.4.3, pour plus de détails sur l'implémentation numérique du modèle). L'algorithme a donc été implémenté dans le code éléments finis Abaqus en utilisant une procédure UMAT. Cette implémentation consiste en la définition (i) des paramètres d'entrée (Props) (voir le Tableau 4.2), (ii) des variables d'état qui sont sauvegardées à chaque pas de temps (Statev) (voir le Tableau 4.1) et (iii) de la résolution numérique (méthode de Newton pour le multiplicateur plastique et du point fixe pour l'écrouissage).

4.1.3 Résultats

Le modèle a d'abord été appliqué à l'étude de l'affinement du grain dans un exemple de chargement proportionnel axisymétrique, en s'interessant en particulier à l'affinement maximal du grain en fonction de la triaxialité et de la porosité initiale. Les résultats ont montré que l'affinement maximal possible des grains est directement influencé par l'état initial du matériau (fraction volumique de vide initiale) et les conditions de chargement (triaxialité de la contrainte).

Enfin, le modèle a été appliqué à la prédiction de la résistance et de la ductilité d'une éprouvette traitée par RCS après deux passes. Ce calcul de structures nous a permis d'avoir accès à l'évolution

des paramètres internes après chaque passe. Nous avons pu comparer l'hétérogénéité et l'évolution des paramètres microstructuraux et également suivre l'évolution et la localisation de l'endommagement au cours du processus. Le modèle permet de capturer qualitativement l'évolution de la résistance et de la ductilité. Il est intéressant de noter que l'augmentation du nombre de passes permet d'homogénéiser la distribution de la taille des grains (ce qui est approprié pour augmenter la résistance), mais que la porosité est en revanche très localisée dans certaines petites zones, ce qui est supposé diminuer la ductilité car cela favorise la localisation des déformations.

Le modèle développé peut être utilisé comme une alternative aux modèles de durcissement de type Voce ou Swift dans l'approche de Gurson, car il est valable pour les importantes déformation habituellement rencontrées pendant la SPD. De plus, il peut être utilisé pour suivre localement l'évolution de la microstructure. Ce modèle constitue un premier pas vers une prédiction quantitative du compromis résistance-ductilité car il est encore limité à des niveaux de triaxialité modérés et la modélisation de la coalescence est heuristique.

4.2 Introduction

In Chapter 3 we analyzed the first pass of the RCS process and it was observed that for moderate corrugation displacements void shape effects can be neglected and the GTN model appeared to be suitable to describe damage evolution. In this chapter we will pursue the development of the numerical framework and consider two passes of the RCS process. The second pass will induce further plastic deformation which requires to consider an advanced hardening modelling that is suitable for materials processed by SPD. Hence, an extended Gurson's model, including a description of the evolution of dislocation densities and cellular structure of dislocations, will be developed and implemented in ABAQUS using user material (UMAT) Fortran subroutine.

This chapter is organized as follows:

First, the experimental procedures performed for two pass RCS process are presented in the case of a pure copper sample. Then, an extended Gurson model including dislocation density evolution is developed and implemented numerically. Its parameters are calibrated using a tensile test of a pure copper. The first application of the model concerns the study of grain refinement in an axisymmet-

ric proportional loading example, which permits to investigate the maximum grain refinement as a function of the triaxiality and initial porosity. Finally the model is applied to the prediction of the strength and ductility of a specimen processed by RCS after two passes.

4.3 Experimental procedures

4.3.1 Material composition

The material used in this chapter is a 99.9% pure copper. It was chosen because (i) it has a high ductility and (ii) it has been widely used in several SPD processes [32, 123, 133] which makes it a good candidate to investigate the strength-ductility evolution. A 61 $\times$ 30 cm cold rolled plate of 0.8 mm thickness was initially cut to a 12 $\times$ 12 cm size. An annealing heat treatment is applied to enhance the ductility and remove residual stress as well as grain distortions due to the previous rolling process. The samples were kept in 550°C temperature for three hours before cooling to room temperature.

4.3.2 RCS multi-pass set-up

The RCS process is applied to the copper specimen similar to the procedure presented in Chapter 3. We recall that a pass corresponds to a corrugation followed by a straightening. For the first pass, corrugation and straightening dies are used on the initial sheet metal sample. For the second pass, the specimen is moved by a distance of half the corrugation period (8 mm) in the $x-$ and $y-$ directions, as shown in Figure 4.1. This permits to increase the homogeneity of the mechanical fields (which are very heterogeneous after the first pass). The process is performed using Instron 8802 servo-hydraulic machine with 250 kN maximum load capacity. Additionally, a very thin layer of Teflon has been placed between the sheet metal and the dies in order to reduce the friction.

4.3.3 Tensile test specimen and procedure

Before the RCS process and after pass 2, tensile tests are performed in order to investigate the effect of the process on the strength-ductility trade-off. The tensile specimen were cut according to ASTM E8M standard with a gauge dimension of 37 $\times$ 7 mm (see Figure 4.2).

Then the tensile tests were performed at deformation speed of 0.5 mm/min (which is equivalent to about 10^{-5} m/s) using an Instron 1125 universal testing machine with 100 kN loading capacity. Very

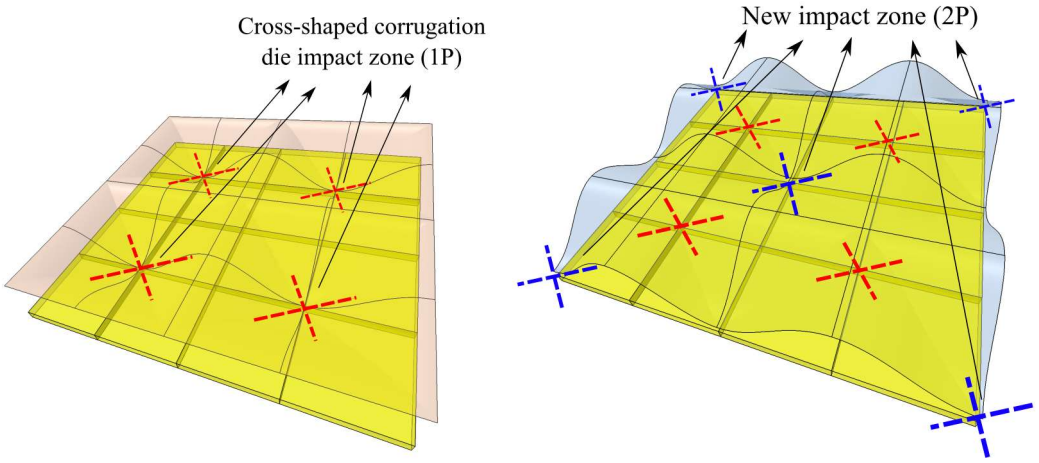

(a) Pass 1 (b) Pass 2

Figure 4.1: Shifting of the corrugation die patterns along the sheet metal specimen after 1st pass. (a) The part of sheet metal shown in the image will undergo corrugation in pass 1 and four patterns will be formed. (b) The corrugation die is shifted half a pattern down and half a pattern to the right.

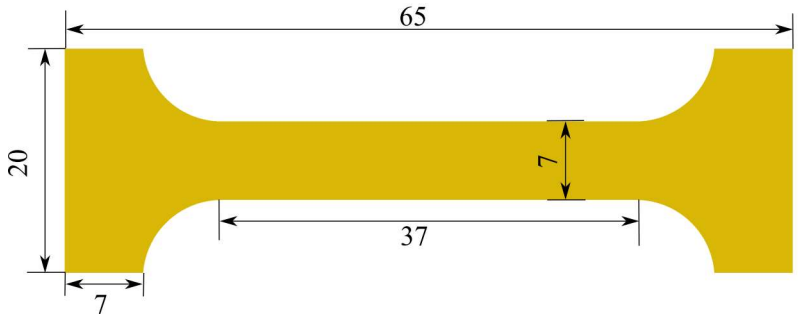

Figure 4.2: Dimension of the tensile test specimen.

slow deformation rates are used to perform quasi-static experiments and avoid strain rate effects. A G51-12MA Instron extensometer was also used to measure the strain. The experimental stress-strain curves obtained before RCS and after 2 passes are reproduced in Figure 4.3. It should be noted that the stress-strain curves after only one pass are not included because of a lack of repeatability due to a high heterogeneity of the local fields.

4.4 An extended Gurson model including dislocation density evolution

In this section, an extended Gurson model including dislocation density evolution is developed. As mentioned in Chapter 1 Section 1.4, conventional hardening laws, such as Voce or Swift laws that were

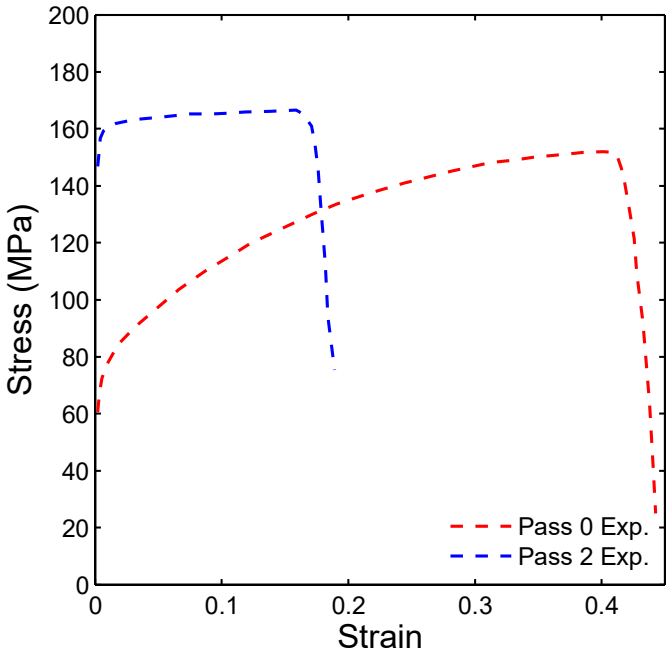

Figure 4.3: Comparison between experimental stress-strain curves of pure copper obtained from tensile test on a specimen cut from the initial state and after 2 passes of RCS. The stress-strain curve after 1 pass is not included due to the lack of repeatability of the results when the tensile specimen is cut from different parts of the processed sheet metal.

used in Chapters 2 and 3, are not suitable for severe plastic deformations when the material undergoes very high strains with important changes in the microstructure. Hence, in order to asses the effect of hardening, grain refinement, and ductile damage, a extension of Gurson [47]'s micromechanical damage model is proposed based on the evolution of dislocation cell structures in the matrix surrounding the void. This model of hardening will be adapted from the composite model developed by Estrin et al. [33] (described in Section 1.4 of Chapter 1).

4.4.1 GTN model

We consider the GTN model for spherical voids. Contrary to the approach adopted in Chapters 2 and 3, here we will neglect void shape effects as a first approximation and voids are assumed to remain spherical during the damage evolution. Hence the model developed will not be suitable for low stress triaxality conditions. Nonetheless, it should be noted that, as shown in Chapter 3, void shape effects

have only a small effect in the simulation of RCS for *moderate corrugation die displacements*.

First, the yield criterion in GTN model is recalled:

$$\Phi(\boldsymbol{\sigma}, \bar{\sigma}, f) = \frac{\sigma_{eq}^2}{\bar{\sigma}^2} + 2qf\cosh\left(\frac{3\sigma_m}{2\bar{\sigma}}\right) - 1 - (qf)^2 \leq 0. \tag{4.1}$$

In this equation σ_{eq} is the macroscopic equivalent von Mises stress, σ_m is the macroscopic mean stress, $\bar{\sigma}$ is the average yield of some fictitious *equivalent* material (whose evolution equation will be given hereafter), f is the volume fraction of porosity, and q is Tvergaard's parameter.

The macroscopic flow rule, deduced from the normality property reads

$$\boldsymbol{D}^p = \dot{\lambda}\frac{\partial\Phi}{\partial\boldsymbol{\sigma}}(\boldsymbol{\sigma}, \bar{\sigma}, f) \quad , \quad \dot{\lambda}\begin{cases} = 0 & \text{if} \quad \Phi(\boldsymbol{\sigma}, f, \bar{\sigma}) < 0 \\ \geq 0 & \text{if} \quad \Phi(\boldsymbol{\sigma}, f, \bar{\sigma}) = 0, \end{cases} \tag{4.2}$$

where $\boldsymbol{D}^p$ is the Eulerian plastic strain rate and $\dot{\lambda}$ is the plastic multiplier.

Void nucleation is described by the strain-controlled term of Chu and Needleman [24]'s heuristic model. The total nucleation rate is given by

$$\dot{f}_{\text{nucleation}} = \frac{f_N}{s_N\sqrt{2\pi}}\exp\left[-\frac{1}{2}\left(\frac{\bar{\varepsilon} - \varepsilon_N}{s_N}\right)^2\right] \times \dot{\bar{\varepsilon}}, \tag{4.3}$$

where f_N, ε_N and s_N respectively represent the volume fraction, average nucleation strain and standard deviation of the nucleating voids.

Void coalescence is classically accounted for by using Tvergaard and Needleman [120]'s classical modification of Gurson [47]'s model, which consists in replacing the porosity f by some larger fictitious one f^*, once some 'critical value' f_c has been reached:

$$f^* = \begin{cases} f & \text{if} \quad f \leq f_c \\ f_c + \delta(f - f_c) & \text{if} \quad f > f_c, \end{cases} \tag{4.4}$$

where f_c and $\delta > 1$ are material parameters.

Finally, following Gurson's approach, the hardening is considered by assuming that the plastic dissipation in the RVE is equal to the plastic dissipation in some fictitious "equivalent material" with the same volume fraction of porosity f:

$$\boldsymbol{\sigma} : \boldsymbol{D}^p = (1 - f)\bar{\sigma}\dot{\bar{\varepsilon}}. \tag{4.5}$$

In this equation, the yield stress $\bar{\sigma}$ is a non-linear function of the equivalent strain $\bar{\varepsilon}$, which will now be described by a dislocation density based model.

4.4.2 Dislocation-based model of hardening

In order to account for severe plastic deformation (and their consequences upon grain refinement), a dislocation-based model of hardening, based on the pioneering work of Estrin et al. [33], is considered. The advantage of this modelling is that it can account for all hardening stages. This approach is based on a description of the dislocation substructures as a composite model, made of cell interiors and walls, in which the dislocation densities have different evolution equations. The model of Estrin et al. [33], initially developed in a 2D case, has been extended to 3D loadings by Tóth et al. [123], through some appropriate modifications of the dislocation density evolution laws. It is important to note that, in this approach, strain rate effects are important notably in the description of dynamic recovery process by dislocation cross-slip. Nonetheless, since Gurson's model has been developed using limit-analysis theory, it is restricted by essence to rate-independent materials. As a consequence, we will use a rate-independent version of Estrin et al. [33]'s model (see e.g. Lapovok et al. [65]).

Following Estrin et al. [33]'s approach, a "composite microstructure", made of cells and walls is considered to describe the microstructure. In this model, the overall resolved shear stress τ depends on the resolved shear stress in each phase (denoted by τ_w in the walls and τ_i in the cell interior) using a rule of mixture:

$$\tau = v_w \tau_w + v_i \tau_i, \tag{4.6}$$

where v_w and $v_i = 1 - v_w$ are respectively the volume fraction of walls and cell interiors. Using the Taylor factor M, the yield stress $\bar{\sigma}$ used in Gurson's model can be express in terms of the equivalent critical resolved shear stress τ:

$$\bar{\sigma} = \tau M. \tag{4.7}$$

In the limit of quasi-static loadings, the resolved shear stresses in each phase are given by

$$\begin{cases} \tau_w &= \alpha \mu b \sqrt{\rho_w} \\ \tau_i &= \alpha \mu b \sqrt{\rho_i}, \end{cases} \tag{4.8}$$

where ρ_w and ρ_i are the dislocation densities in the walls and cell interiors, respectively. In equation (4.8), b is the magnitude of the dislocation Burgers vector, α is a constant (typically around 0.25) and μ is the shear modulus. Then, we make the classical assumption that the resolved shear strain rates for the cell walls $\dot{\gamma}_w$ and cell interiors $\dot{\gamma}_i$ are equal to some equivalent resolved shear strain $\dot{\gamma}$

$$\dot{\gamma}_w = \dot{\gamma}_i = \dot{\gamma}. \tag{4.9}$$

In addition, the equivalent resolved shear strain $\dot{\gamma}$ can be related to the plastic strain rate $\dot{\bar{\varepsilon}}$, using again the Taylor factor M:

$$\dot{\bar{\varepsilon}} = \frac{\dot{\gamma}}{M}. \tag{4.10}$$

Under the assumption of quasi-static loadings, the evolution equation of the dislocation densities ρ_w and ρ_i can then be written as

$$\begin{cases} \dot{\rho}_w &= \left(\alpha^* \dfrac{6 v_i^{2/3}}{b d v_w} + \beta^* \dfrac{\sqrt{3} v_i \sqrt{\rho_w}}{v_w b} - k_0 \rho_w \right) M \dot{\bar{\varepsilon}} \\ \dot{\rho}_i &= \left(\alpha^* \dfrac{\sqrt{\rho}_w}{\sqrt{3} b} - \dfrac{6 \beta^*}{b d v_i^{1/3}} - k_0 \rho_i \right) M \dot{\bar{\varepsilon}}. \end{cases} \tag{4.11}$$

In equation (4.11), α^* is constant related to the fraction of operative Franck-Read sources, β^* is a constant related to the fraction of dislocations moving from cell interiors to walls and finally k_0 is a constant related to dislocation annihilation.

Motivated by experimental observation on metals, the volume fraction of cell walls is assumed to decrease with the evolution of the resolved shear strain according to the following phenomenological expression

$$v_w = v_{inf} + (v_0 - v_{inf}) \exp\left(-\frac{\bar{\varepsilon}}{\Gamma} \right), \tag{4.12}$$

where v_0 is the initial volume fraction of cell walls (before plastic deformation) and v_{inf} is the minimal value (reached after large plastic strains). In equation (4.12), Γ is a parameter that controls the "shrinkage" rate of the dislocation cells.

Finally, the total dislocation density in the material can be deduced from the dislocation densities in both cell walls and cell interior as

$$\rho = v_w \rho_w + v_i \rho_i. \tag{4.13}$$

Therefore, an increase of the dislocation density would lead to a decrease of the average grain size which can be estimated using Holt's equation:

$$d = \frac{K}{\sqrt{\rho}}, \tag{4.14}$$

where K is a constant.

4.4.3 Numerical implementation of the model

The numerical implementation of the model is now presented and in particular we focus on the local step of the elastoplastic solution which consists in projecting the elastic stress predictor on the yield surface.

Following Enakoutsa et al. [30], Gurson [47]'s model fits into the class of "generalized standard" materials [50] under some hypotheses: the existence and uniqueness of the solution of the projection problem are ensured [30], provided that (i) the evolution equations of $\boldsymbol{\varepsilon}$ (the total strain) and $\overline{\varepsilon}$ (the hardening parameter) are discretized in time with an implicit-scheme; (ii) the additional terms due to the objective time-derivative of $\boldsymbol{\Sigma}$ (in the hypoelasticity law) are discretized in time with an explicit-scheme; (iii) the value of the porosity f used in the criterion and the flow rule is taken at the preceding time-step. The equations of the local problem read

$$\left\{\begin{array}{ll}
\boldsymbol{\varepsilon} = \boldsymbol{\varepsilon}^{\mathrm{e}} + \boldsymbol{\varepsilon}^{\mathrm{p}} & \text{Decomposition of the total strain} \\
\boldsymbol{\sigma} = (3\kappa\mathbb{J} + 2\mu\mathbb{K}) : \boldsymbol{\varepsilon}^{\mathrm{e}} & \text{Isotropic elasticity law} \\
\Phi(\boldsymbol{\sigma}, f, \overline{\sigma}) \leq 0 & \text{Plasticity criterion} \\
\left\{\begin{array}{lcl}
\dot{\boldsymbol{\varepsilon}}^{\mathrm{p}} & = & \dot{\lambda}\dfrac{\partial \Phi}{\partial \boldsymbol{\sigma}}(\boldsymbol{\sigma}, f, \overline{\sigma}) \\
\dot{\lambda} & \geq & 0 \\
\dot{\lambda}\Phi(\boldsymbol{\sigma}, f, \overline{\sigma}) & = & 0
\end{array}\right. & \text{Flow rule and consistency conditions} \\
\overline{\sigma} \equiv \sigma(\overline{\varepsilon}, \rho_w, \rho_i), (1-f)\overline{\sigma}\ \dot{\overline{\varepsilon}} = \boldsymbol{\sigma} : \dot{\boldsymbol{\varepsilon}}^{\mathrm{p}}, & \text{Strain hardening law}
\end{array}\right. \tag{4.15}$$

where $\overline{\sigma} \equiv \sigma(\overline{\varepsilon}, \rho_w, \rho_i)$ is the hardening function depending on the dislocation densities of the composite microstructure, $\boldsymbol{\varepsilon}^{\mathrm{e}}$ is the elastic strain tensor, $\boldsymbol{\varepsilon}^{\mathrm{p}}$ the plastic strain tensor. The fourth-order tensors $\mathbb{J}$ and $\mathbb{K}$ are respectively the spherical projection tensor and the deviatoric projection tensor, and κ

and μ are respectively the bulk and shear moduli.

The local projection problem thus consists in finding the mechanical state $\mathcal{S}_{n+1} = \{\boldsymbol{\varepsilon}_{n+1}\,,\ \boldsymbol{\varepsilon}^{\mathrm{p}}_{n+1},\ \boldsymbol{\sigma}_{n+1},\ \overline{\varepsilon}_{n+1}\}$ at time t_{n+1} resulting from a given, known strain increment $\Delta\boldsymbol{\varepsilon}_n$ (resulting from a global elastoplastic iteration) and knowing the previous mechanical state $\mathcal{S}_n = \{\boldsymbol{\varepsilon}_n\,,\ \boldsymbol{\varepsilon}^{\mathrm{p}}_n,\ \boldsymbol{\sigma}_n,\ \overline{\varepsilon}_n\}$ at time t_n. The yield criterion and the flow rule are thus discretized using an implicit scheme with respect to $\boldsymbol{\varepsilon}^{\mathrm{p}}$ and $\overline{\varepsilon}$, while an explicit scheme is considered for f. The discretized equations of the local projection problem are given by

$$\left\{\begin{array}{lcl} \boldsymbol{\sigma}_{n+1} & = & \boldsymbol{\sigma}^{\mathrm{elas}}_{n+1} - (3\kappa\mathbb{J} + 2\mu\mathbb{K}) : \Delta\boldsymbol{\varepsilon}^{\mathrm{p}}_n \\ \Phi(\boldsymbol{\sigma}_{n+1}, f_n, \overline{\sigma}_{n+1}) & \leq & 0 \\ \Delta\boldsymbol{\varepsilon}^{\mathrm{p}}_n & = & \Delta\lambda_n \dfrac{\partial\Phi}{\partial\boldsymbol{\sigma}}(\boldsymbol{\sigma}_{n+1}, f_n, \overline{\sigma}_{n+1}) \\ \Delta\lambda_n & \geq & 0 \\ \Delta\lambda_n \Phi(\boldsymbol{\sigma}_{n+1}, f_n, \overline{\sigma}_{n+1}) & = & 0 \\ \overline{\sigma}_{n+1} & = & \sigma(\overline{\varepsilon}_n + \Delta\overline{\varepsilon}_n) \\ (1-f_n)\overline{\sigma}_{n+1}\Delta\overline{\varepsilon}_n & = & \boldsymbol{\sigma}_{n+1} : \Delta\boldsymbol{\varepsilon}^{\mathrm{p}}_n, \end{array}\right. \tag{4.16}$$

where $\boldsymbol{\sigma}^{\mathrm{elas}}_{n+1} = \boldsymbol{\Sigma}_n + (3\kappa\mathbb{J} + 2\mu\mathbb{K}) : \Delta\boldsymbol{\varepsilon}_n$ is the elastic predictor, that is the stress tensor at time t_{n+1} resulting from the strain increment $\Delta\boldsymbol{\varepsilon}_n$ fictitiously considered as purely elastic.

The algorithm consists essentially in finding $\overline{\sigma}_{n+1}$ and $\Delta\boldsymbol{\varepsilon}^{\mathrm{p}}_{n+1}$ and the treatment of hardening is done classically using a fixed point method, as explained in the following steps:

1. Initialization of the yield stress using the previous value. Assume that

$$\left\{\begin{array}{ll} \rho_{w,n+1} & = \rho_{w,n} \\ \rho_{i,n+1} & = \rho_{i,n} \\ v_{w,n+1} & = v_{inf} + (v_0 - v_{inf})\exp\left(-\dfrac{\overline{\varepsilon}_n}{\Gamma}\right) \\ v_{i,n+1} & = 1 - v_{w,n+1} \\ d_{n+1} & = \dfrac{K}{\sqrt{v_{w,n+1}\rho_{w,n+1} + v_{i,n+1}\rho_{i,n+1}}} \end{array}\right. \tag{4.17}$$

   so one has

$$\overline{\sigma}_{n+1} = \overline{\sigma}_n = \alpha\mu b M(v_{w,n+1}\sqrt{\rho_{w,n+1}} + v_{i,n+1}\sqrt{\rho_{i,n+1}}). \tag{4.18}$$

2. Compute $\boldsymbol{\varepsilon}^{\mathrm{p}}_{n+1}$ and $\boldsymbol{\sigma}_{n+1}$ with this value $\overline{\sigma}_{n+1}$ using Newton–Raphson method. This step will not be detailed here since it is classical for GTN model (see e.g. the algorithms of Enakoutsa et al. [30] or Dorhmi et al. [26]).

3. Deduce the increment of equivalent accumulated plastic strain $\Delta\overline{\varepsilon}_n = \dfrac{\boldsymbol{\sigma}_{n+1} : \Delta\boldsymbol{\varepsilon}^{\mathrm{p}}_n}{(1-f_n)\overline{\sigma}_{n+1}}$.

4. Compute the increment of dislocation densities

$$\left\{\begin{array}{ll} \Delta\rho_{w,n+1} & = \left(\alpha^* \dfrac{6(v_{i,n+1})^{2/3}}{bd_{n+1}v_{w,n+1}} + \beta^* \dfrac{\sqrt{3}v_{i,n+1}\sqrt{\rho_{w,n+1}}}{v_{w,n+1}b} - k_0\rho_{w,n+1}\right) M\Delta\overline{\varepsilon}_n \\ \Delta\rho_{i,n+1} & = \left(\alpha^* \dfrac{\sqrt{\rho}_{w,n+1}}{\sqrt{3}b} - \dfrac{6\beta^*}{bd_{n+1}v_{i,n+1}^{1/3}} - k_0\rho_{i,n+1}\right) M\Delta\overline{\varepsilon}_n. \end{array}\right. \tag{4.19}$$

5. Update the values of the dislocation densities, volume fraction of cell walls and average cell size

$$\left\{\begin{array}{ll} \rho_{w,n+1} & = \rho_{w,n} + \Delta\rho_{w,n} \\ \rho_{i,n+1} & = \rho_{i,n} + \Delta\rho_{i,n} \\ v_{w,n+1} & = v_{inf} + (v_0 - v_{inf})\exp\left(-\dfrac{\overline{\varepsilon}_n + \Delta\overline{\varepsilon}_n}{\Gamma}\right) \\ v_{i,n+1} & = 1 - v_{w,n+1} \\ d_{n+1} & = \dfrac{K}{\sqrt{v_{w,n+1}\rho_{w,n+1} + v_{i,n+1}\rho_{i,n+1}}} \end{array}\right. \tag{4.20}$$

6. Deduce a refined estimate of $\overline{\sigma}_{n+1}$:

$$\overline{\sigma}_{n+1} = \overline{\sigma}_n = \alpha\mu bM(v_{w,n+1}\sqrt{\rho_{w,n+1}} + v_{i,n+1}\sqrt{\rho_{i,n+1}}). \tag{4.21}$$

and follow the procedure (step 2 to 6) until the method converges and $\overline{\sigma}_{n+1}$ reaches a stationary value.

4.4.4 Description of the UMAT

The algorithm has then been implemented in the finite element code Abaqus using a UMAT procedure. This implementation consists in the definition of (i) input parameters (Props), (ii) state variables that are saved at each times step (Statev) and (iii) the numerical resolution (Newton method for the plastic multiplier and fixed point for hardening). Furthermore, an ad-hoc modification has been added to the previous constitutive equations to avoid numerical issues. Indeed, in ductile fracture problems, softening can become brutal when the damage parameter (here corresponding to qf^*) reaches high values, typically when $qf^* \geq 0.3$. Therefore, it is of interest to "delete" elements that can be considered as (almost) totally damaged, because in such case fracture occurs almost instantaneously. Thus, when the damage parameter qf^* becomes larger than a critical value, denoted by f_F, the stress is imposed

to become nil, that is $\boldsymbol{\sigma} = \mathbf{0}$, corresponding to element deletion.

The internal parameters that are stored (in addition to the stress tensor), either for the calculations and post-treatments, are provided in Table 4.1.

Table 4.1: State Variables (STATEV) used in this UMAT.

STATEV	Parameter	Variable name
1	f	FV
2	$\bar{\varepsilon}_p$	EPSB
3	ρ_w	RHOW
4	ρ_i	RHOI
5	v_w	VW
6	d	DSIZE

A summary of the input parameters that are required for this model is provided in Table 4.2. They consists of 2 elastic constants, 11 constants for the hardening behavior and 8 parameters for the ductile damage behavior.

4.4.5 Calibration of the model parameters for pure copper

The model parameters have been calibrated for the pure copper considered in the experiments of Section 4.3. First, the elastic constants for the pure copper are classically taken as $E = 120$ GPa and $\nu = 0.358$.

Then, the parameters related to the hardening composite model are calibrated by adjusting the parameters found in the literature [46, 65], which are generally calibrated using TEM for initial dislocation densities (ρ_w and ρ_i), EBSD for volume fraction of cell walls and interiors (v_w and v_i) and discrete dislocation dynamics simulations for dislocation production, migration and annihilation constants (α^* and β^* and k_0), in order to reproduce the experimental stress-strain curve of the tensile test for the pure copper (see Figure 4.3). The set of parameters related to hardening is provided in Table 4.3.

Table 4.2: Input property parameters (PROPS) used in the UMAT developed.

Props number	Parameter	Variable name
Elastic Constants		
1	E	E
2	ν	NU
Dislocation Density-based hardening law parameters		
3	ρ_w^0	RHOW0
4	ρ_i^0	RHOI0
5	α	ALPHA
6	b	BURGERS
7	M	MTAYLOR
8	α^*	ASTAR
9	β^*	BSTAR
10	k_0	K0
11	v_{inf}	VINF
12	v_0	V0
13	Γ	GAMMA
14	K	K
GTN ductile damage parameters		
15	f_0	K0
16	q	VINF
17	f_c	FC
18	δ	DLT
19	f_N	FN
20	ε_N	EPSN
21	s_N	SN
22	f_F	FF

ρ_{w0} [m^{-2}]	ρ_{i0} [m^{-2}]	α	b [m]	M	α^*	β^*	k_0	v_{inf}	v_0	Γ	K
4×10^{14}	2×10^{14}	0.25	2.56×10^{-10}	3.06	0.065	0.012	4.3	0.06	0.2	3.2	500

Table 4.3: Values of parameters for dislocation density based hardening law for pure copper.[123]

Finally, the next step is the calibration of the GTN damage parameters, f_0, f_c, δ, f_N, s_N and ε_N. This can be done through microtomography observations using synchrotron diffraction experiments or by using macroscopic results such as a tensile test. Here the parameters have been calibrated using the macroscopic tensile test for simplicity. It must be noted that the set of parameters calibrated is generally not unique as different sets of parameters of Gurson's model could lead to the same softening and fracture behavior [111]. The set of parameters related to damage is provided in Table 4.4

f_0	q	f_c	δ	f_N	ε_N	s_N
0.001	1	0.01	8	0.01	0.3	0.2

Table 4.4: Values of parameters for damage in the case of pure copper.

The model predictions (using the calibrated parameters) are compared to the experimental results in Figure 4.4. Overall the numerical stress-strain curve is in very good agreement with the experimental curve.

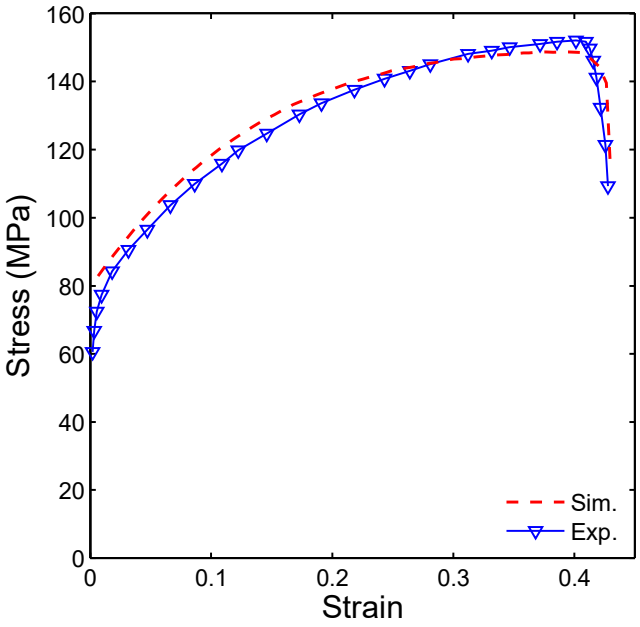

Figure 4.4: Comparison of numerical and experimental stress-strain curves for copper.

4.5 Numerical study of grain refinement in an axisymmetric proportional loading example

In this section, we investigate the response of an elementary volume predicted by the model for an axisymmetric proportional loading with major axial stress, under conditions of fixed stress triaxiality. This case of homogeneous loading will be of interest to investigate the influence of the initial porosity and loading conditions on the achievable grain refinement before failure.

4.5.1 Description of the simulations

We consider an elementary volume (i.e. a material point) subjected to a macroscopic loading state under conditions of fixed stress triaxiality $T = \sigma_m/\sigma_{eq}$. The non-zero components of the stress tensor are:

$$\begin{cases} \sigma_{11} &= \sigma_{22} = \sigma_{\mathrm{m}} - \dfrac{1}{3}\sigma_{\mathrm{eq}} \\ \sigma_{33} &= \sigma_{\mathrm{m}} + \dfrac{2}{3}\sigma_{\mathrm{eq}}. \end{cases} \tag{4.22}$$

In terms of model parameter, we will consider, for the hardening behavior, the calibrated values of the pure copper given in Table 4.4. For the parameters of the GTN model, we will consider fictitious values for the porosity (in order to study its influence) and no nucleation will be considered: the values $f_0 = [0.005;\ 0.001;\ 0.0002]$ and $f_c = 0.01$ will be considered. In addition, several values for the stress triaxialitiy will be considered: $T = [1/3;\ 1/2;\ 2/3\ ;3/4;\ 1;\ 3/2]$.

The objective of these simulations is to investigate the influence of the porosity f_0 and the loading conditions (through the value of the imposed stress triaxiality T) on grain refinement. In particular, we will study the evolution of the grain size d (as a function of the strain), and notably the value of d when coalescence is reached: this value would correspond to the minimal grain size achievable before failure.

4.5.2 Results

First, the evolution of the normalized macroscopic stress $\sigma_{eq}/\bar{\sigma}_0$ (where $\bar{\sigma}_0$ is the initial yield stress calculated using the values of Table 4.3) and normalized porosity f/f_0 are represented in Figures 4.5, 4.6 and 4.7 respectively for the cases $f_0 = 0.0002$, $f_0 = 0.001$ and $f_0 = 0.005$. In each case, the influence of the stress triaxiality is investigated. As expected for the GTN model (irrespective of the hardening law), the critical f_c is reached more rapidly for (i) an important stress triaxiality T (because the porosity growth rate increases when the stress triaxiality T increases) and (ii) a high initial volume fraction f_0.

In addition, the evolution of several internal parameters is shown in Figure 4.8 in the case $T = 1/3$ and $f_0 = 0.0002$ for illustrative purposes. First, the evolution of the normalized dislocation densities in cell walls ρ_w/ρ_{w0} and cell interiors ρ_i/ρ_{i0} are shown Figure 4.8a. The increase of the dislocation

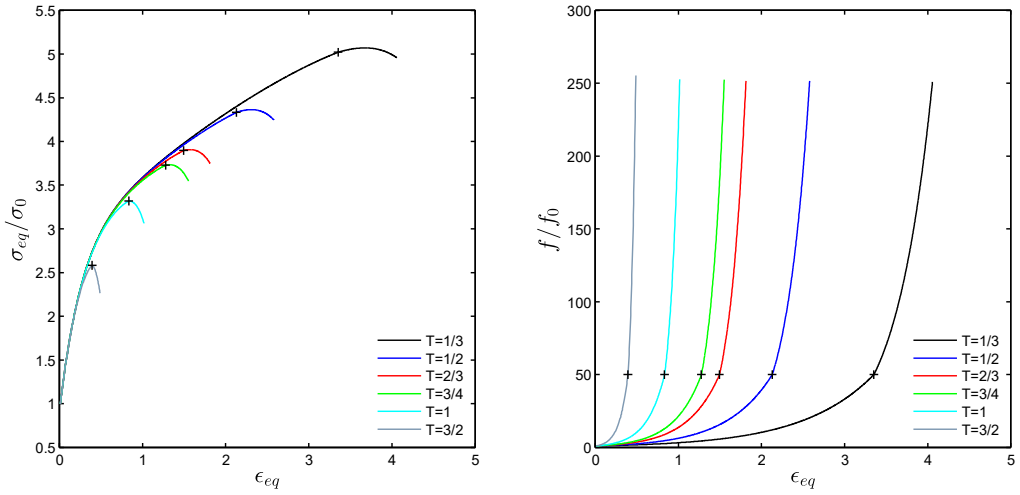

(a) (b)

Figure 4.5: Numerical results for the extended GTN model applied to an elementary volume for $f = 0.0002$. Evolution of (a) Normalized equivalent stress $\sigma_{eq}/\bar{\sigma}_0$ and (b) Normalized void volume fraction f/f_0. The onset of coalescence is shown by the symbol $+$.

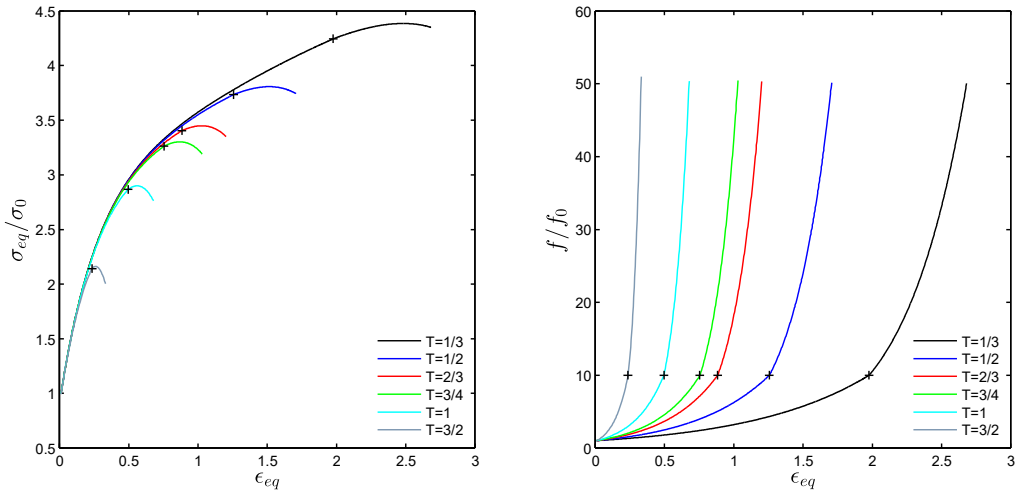

(a) (b)

Figure 4.6: Numerical results for the extended GTN model applied to an elementary volume for $f = 0.001$. Evolution of (a) Normalized equivalent stress $\sigma_{eq}/\bar{\sigma}_0$ and (b) Normalized void volume fraction f/f_0. The onset of coalescence is shown by the symbol $+$.

density in the walls is very important in comparison to the increase of the dislocation in the cell interiors. However, it has only a moderate effect on the evolution of the total dislocation density ρ/ρ_0

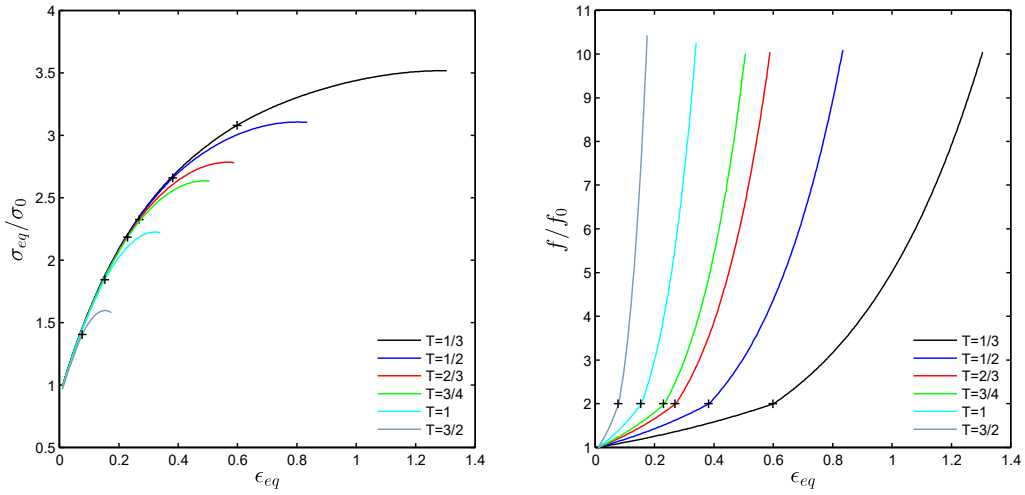

(a) (b)

Figure 4.7: Numerical results for the extended GTN model applied to an elementary volume for $f = 0.005$. Evolution of (a) Normalized equivalent stress $\sigma_{eq}/\bar{\sigma}_0$ and (b) Normalized void volume fraction f/f_0. The onset of coalescence is shown by the symbol $+$.

because the volume fraction of cell walls v_w (i) is initially lower than that of cell interiors v_i and (ii) it decreases rapidly as shown in Figure 4.8b. The average cell size d is represented in Figure 4.8c: it decreases from the value $d_0 \sim 32$ μm to approximately 6 μm (at $\varepsilon_{eq} \sim 4$): therefore in that case a "grain refinement" with a ratio $d_0/d \sim 6$ is achieved.

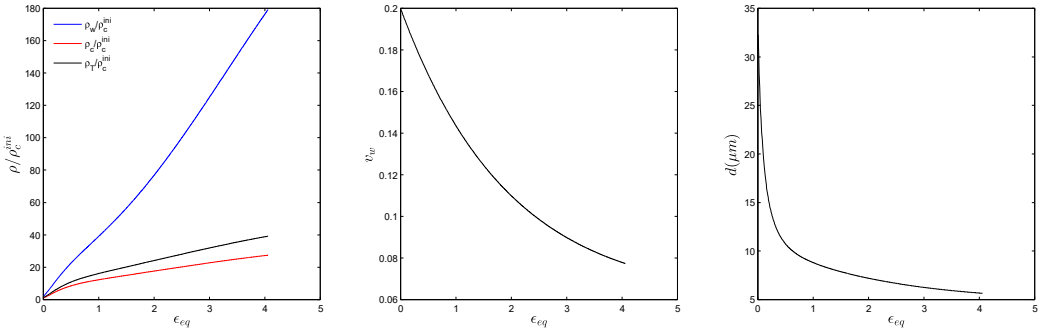

(a) (b) (c)

Figure 4.8: Evolution of some internal variables using the developed model for $T = 1/3$ and $f_0 = 0.0001$. (a) Normalized dislocation densities in cell walls ρ_w, cell interiors ρ_c and total dislocation density ρ_T, (b) Volume fraction of cell walls v_w and (c) Average cell size parameter d.

Finally, the maximal ratio of cell refinement d_0/d before the coalescence occurrence, is represented

in Figure 4.9 for all the values of f_0 and T considered. As expected, grain refinement is promoted by a decrease of the triaxiality and the initial volume fraction f_0; it should be noted that the values considered for the triaxiality has been restricted to $T > 1/3$ because the GTN model is not suitable at low stress triaxiality. Nonetheless, the trend observed is expected to continue when T reaches zero to negative values but threshold for d_0/d is also expected to exist. According to these results, important grain refinement can be achieved at low stress triaxiality levels and with materials having low levels of initial impurities. In the context of SPD processes, in which the final aim is to provide important grain refinement, these results show that grain refinement is generally influenced by (i) the initial conditions of the material in term of damage and (ii) the loading conditions applied to the material during the process.

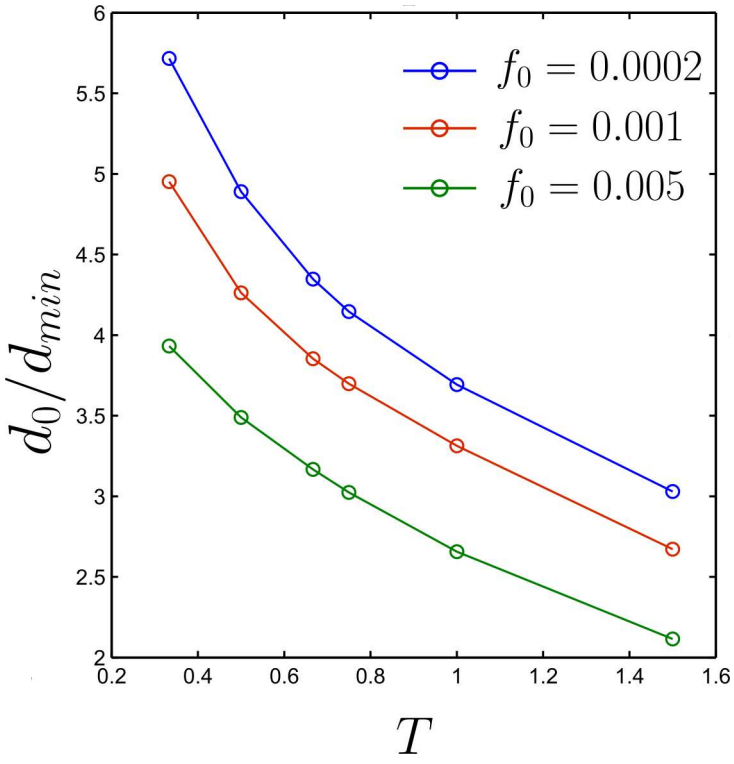

Figure 4.9: The maximum grain refinement d_0/d_{min} achieved as a function of triaxiality T and initial void volume fraction f_0.

4.6 Numerical prediction of strength and ductility after Repetitive Corrugation and Straightening processing

The aim of this section is to predict numerically the stress-strain curve of a specimen processed by RCS, which corresponds to the determination of the strength and ductility after severe plastic deformation.

4.6.1 Description of the numerical model

The numerical model used for investigating the strength-ductility trade-off is composed of a two-steps RCS procedure followed by a tensile test:

- The simulation of RCS is composed of one deformable sheet metal blank, four corrugation and four straightening dies. The first pass of the model is performed using the same numerical model than used in Chapter 3 Section 3.4. However, we did not use the $1/8^{\text{th}}$ symmetric configuration because one plane of symmetry is lost during the second pass. Therefore we considered a model of $1/4^{\text{th}}$ of a pattern. In order to perform the second pass, the corrugation dies are moved half a pattern (8mm) in both the x- and y-directions. The boundary conditions for the first and second pass are shown in Figure 4.10.

- After the very last step of the second pass, a tensile test is performed: this is done by applying a displacement on the surface of the blank in the x^+ direction while maintaining the double symmetry conditions on surfaces with normal vectors x^- and z^-. It should be noted that this procedure permits only to perform an approximate tensile test, as necking cannot take place. In order to assess its relevance, the same procedure will also be used before processing (i.e. at 0 pass) and compared to the tensile test performed numerically in Section 4.4.

Unlike the aluminum sheet metals used in Chapter 3, the thickness of copper samples are 0.8 mm. A mesh size of 0.1 mm has been used for the deformable sheet metal and 0.15 mm for the rigid dies. A constant mesh size has been taken to be equal in all cases of RCS and tensile test simulations in order to get comparable results and avoid any mesh dependency from one simulation to another. Also the coefficient of friction is taken equal to 0.05 which represents low friction (due to Teflon) copper-steel contact.

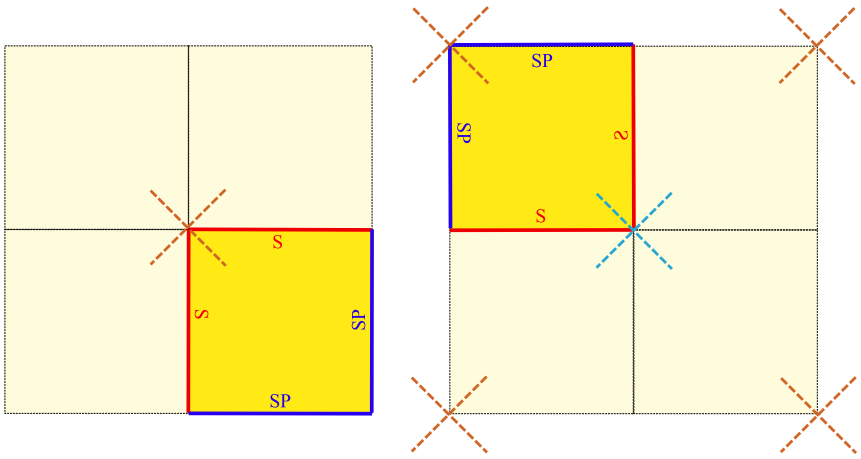

Figure 4.10: The boundary condition applied to the reduced model ($1/4^{\text{th}}$ model) in (a) pass 1 and (b) pass 2. SP corresponds to "Symmetric-Periodic" and S corresponds to "Symmetric" (see Appendix A)

Several quantities will be studied in order to investigate the evolution of damage and dislocation structure as a function of the number of RCS passes:

1. The distribution of internal variables of the model will be studied after 1 and 2 passes. In particular we will consider variables related to (i) hardening such as total dislocation density ρ_t and average cell size d and (ii) damage void volume fraction f. This allows us to better understand the phenomenon governing the change in strength and ductility happening during RCS.

2. The macroscopic stress-strain response before and after the process will be studied. This will show the increase in the strength and the evolution of the ductility happened after each pass. It should be noted that the results for the first pass will not be presented because of a lack of representativity in the experimental results due to a very high heterogeneity of the local fields.

4.6.2 Results

The distribution of the total dislocation density ρ_t is represented in Figure 4.11 after pass 1 and pass 2. After the first pass, the dislocation ρ_t increases by a factor of 10 from an initial value of 2.4×10^{14} m^{-2} to $2.4{\times}10^{15}$ m^{-2} at the most deformed area. It is very heterogeneous with a minimum value of 2.7×10^{14} m^{-2} (in the areas far from the corrugation pattern) and a maximum value of

2.4×10^{15} m^{-2}. Its average value, which can be computed as its volume average, is of about 9×10^{14} m^{-2}. After the second pass, the distribution of ρ_t is more homogeneous, with a minimum value of 6.8×10^{14} m^{-2} and a maximum value of 2.7×10^{15} m^{-2}. Its average value is of about 1.5×10^{15} m^{-2}. Therefore, both the maximum and average of the total dislocation density increase with the number of passes. Furthermore, the homogeneity of the distribution also increases with the number of passes.

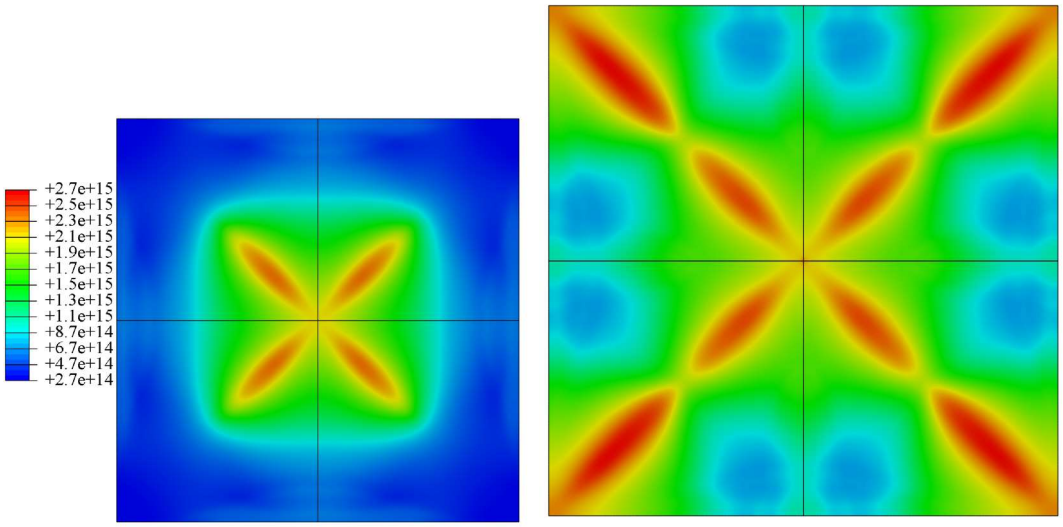

(a) (b)

Figure 4.11: Distribution of total dislocation density ρ_t after (a) Pass 1 and (b) Pass 2.

Figure 4.12 illustrates the distribution of average cell (grain) size parameter d after pass 1 and pass 2. The results show that in the first pass, moderate grain refinement by a factor of 3 has been achieved in the heavily deformed heterogeneous cross shaped spots. The minimum and maximum grain sizes are respectively of about 10 and 32 μm, and the average grain size is 18 μm. After the second pass, the minimum cell size does not change much (from 10 to about 9 μm) but the homogeneity of the refinement increases. Indeed in that case, the minimum and maximum grain sizes are respectively of about 19 and 9 μm, and the average grain size is 13 μm. This is due to the particularity of the second pass as it shifts the cross shaped zone.

Then, in order to follow the evolution of damage during the process, Figure 4.13 shows the distribution of void volume fraction parameter f after pass 1 and pass 2. After the first pass, the distribution of the porosity is very heterogeneous and f reaches a maximum value of 0.007 in a very localized area in the cross-shaped zone at the back side of the sheet metal. After the second pass, the maximum

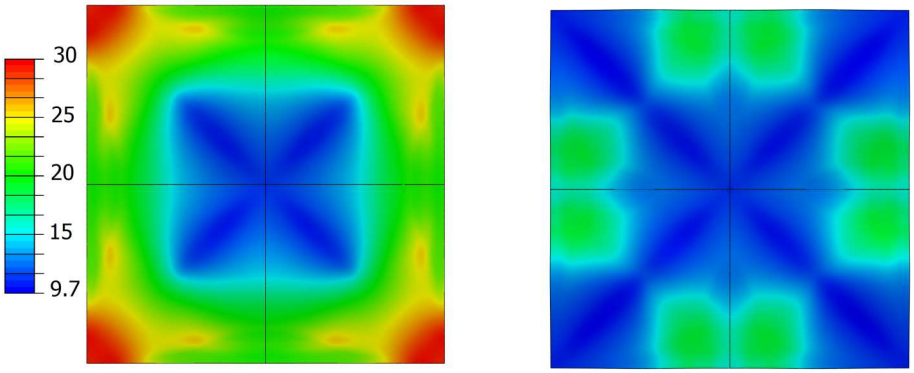

(a) (b)

Figure 4.12: Distribution of average cell size d after (a) Pass 1 and (b) Pass 2.

value is shifted to the position of the new cross and reaches a value of 0.009 but mostly on the front side. It is also heterogeneous with maximum values localized in very small areas separated by less damaged areas. It should be noted that the evolution of void volume fraction is generally due to the corrugation step: in our cases, the value of f in corrugation steps of pass 1 and pass 2 has reached 0.01 and 0.03 (and then it decreases during straightening). Overall, the void volume fraction increases moderately during a full pass but it becomes very heterogeneous.

Finally, the stress-strain curves before and after processing, respectively denoted by 0P and 2P, are represented in Figure 4.14 and compared to the experimental results. It must be noted that before processing (0P), two numerical stress-strain curves are represented: one is obtained from a numerical tensile test using the specimen represented in Figure 4.2 (this curve corresponds to the result of Figure 4.4) and the other one is obtained from the unprocessed plate. Overall, a good agreement is observed between the experimental and numerical results, that is an increase of the yield strength and a decrease of the ductility as the number of passes increases. Before processing some differences are observed between the two numerical results, because necking in the tensile test performed on the unprocessed plate is delayed: ductility is therefore slightly overestimated. After pass 2, the numerical model is able to capture the trend of the hardening (which "saturates") but its level is slightly overestimated. In the numerical tensile test after pass 2, failure occurs at a strain of about 0.12 which is slightly lower than the experimental value (0.17). These results shows that the model is able to qualitatively capture the strength-ductility evolution of material during RCS.

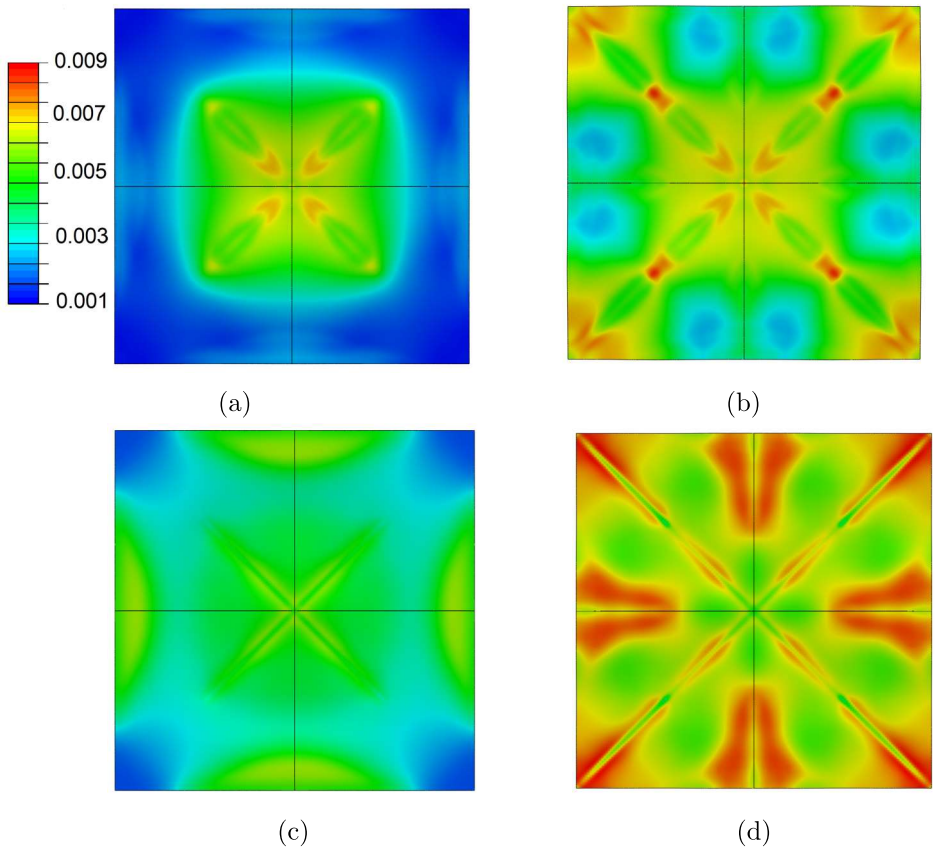

Figure 4.13: Distribution of the void volume fraction f after (a) Pass 1 (back face), (b) Pass 2 (back face), (c) Pass 1 (front face) and (d) Pass 2 (front face).

4.7 Discussion

The model developed in this chapter allows a description of several microstructural changes that occur during plastic deformation such as the evolution of the dislocation density, grain size and void volume fraction. The model has been used to simulate a multi-pass SPD process and overall it has been successful in predicting the strength-ductility trade-off after plastic deformation. The results obtained are thus promising in the investigation of the strength-ductility dilemma. Several comments are in order:

- The numerical tensile test performed after the second pass of RCS may not be fully representative of the experimental tensile test because it is performed on the full plate while the specimen for the experimental tensile test has been performed using a standard geometry; necking is thus absent from the numerical simulation. It should also be noted that the experimental results can

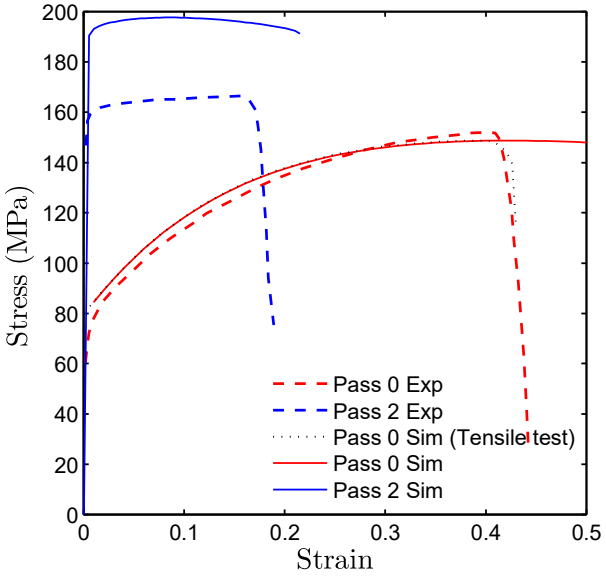

Figure 4.14: Comparison between numerical and experimental stress-strain curves of copper at initial state and after 1 and 2 passes of RCS.

be different if the specimen is cut in another location of the processed specimen: the location and the pattern chosen to cut the specimen can influence the stress-strain curve. For instance, the RCS experimental geometry is composed of a 7×7 corrugation die pattern, so a specimen cut from a pattern that is not inside the stabilized zone (see Appendix A) would not provide representative results. Furthermore it was observed that after one pass, there is a lack of representativity of the experimental stress-strain curves because the process is very heterogeneous after one pass.

- The porosity increases in corrugation step and decreases in straightening due to high compression. However the increase is not completely reversible because the "nucleated porosity" continues increasing at each pass. Consequently, the void volume fraction evolution has an irreversible cyclic characteristic and the highest value is always achieved at the corrugation step, as shown in Figure 4.15. Fracture can even eventually happen during corrugation. This behavior can explain how damage will modify ductility; indeed this continuous increase of the porosity due to nucleation will decrease the overall ductility.

- The geometry considered for the corrugation dies lead to mix of heterogeneity (heavily deformed cross shaped areas) and homogeneity (shifted crosses at each pass). This would lead to creation of

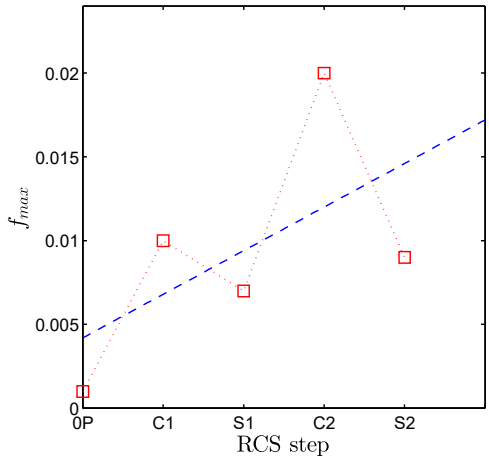

Figure 4.15: Evolution of maximum void volume fraction with different steps of RCS. C1, S1, C2 and S2 are corrugation and straightening steps of pass 1 and pass 2 respectively.

a composite material microstructure which could be interesting for increasing the yield strength (in heavily deformed areas). Nonetheless, the presence of localized area with high levels of porosity decreases the ductility even if the average porosity does not increase much: indeed these areas will promote strain localization and therefore ductility will decrease. A modification of the die geometry would be necessary to delete these very localized areas in order to enhance the ductility.

- Grain refinement and dislocation density have a rapid increase in the first pass and then tend to saturate at higher passes (see Figures 4.12 and 4.11). This is a characteristic of the behavior of microstructure in metals. This was also observed in Figure 4.8a and 4.8d.

- The model developed in this work was based on the GTN model (for spherical voids) because of the relatively high triaxiality during RCS processing with low levels of corrugations. This model is only valid as long as we avoid inducing shear deformation by applying high values of corrugation die displacement. It should be mentioned however that as we saw in Chapter 3, there are still some void shape effects that neglecting them could delay the onset of fracture to some extent. The extension of the ML model using the dislocation-based density model would permit to consider shear-dominated loadings. However since coalescence under shear is complex, the prediction of the ductility would still be difficult as the only available model of coalescence

is heuristic.

- The GTN model is derived using limit-analysis which excludes by essence rate-dependent behaviors. Since in practice the hardening model of Estrin et al. [33] is rate-dependent (to describe dynamic recovery notably), it could be interesting to consider a rate-dependent extension of Gurson's model, as done by Leblond et al. [67] (see also Flandi and Leblond [37]).

4.8 Conclusion

In this chapter two pass RCS process was analyzed in the case of a pure copper sample. An extended Gurson model including dislocation density evolution was developed and implemented numerically, in order to take into account the cellular microstructure of materials processed by SPD. The model has been first applied to the study of grain refinement in an axisymmetric proportional loading example, allowing the investigation of the maximum grain refinement as a function of the triaxiality and initial porosity. Finally the model was applied to the prediction of the strength and ductility of a specimen processed by RCS after two passes. The main results can be resumed as follows:

- In the case of axisymmetric proportional loading, the results showed the influence of some parameters including initial void volume fraction and stress triaxiality on the hardening behavior of the material. The maximum grain refinement possible is directly influenced by material degradation (initial void volume fraction) and loading condition (stress triaxiality): decreasing the stress triaxiality and the initial porosity permits to achieve more grain refinement before coalescence.

- The structural simulation of two-pass RCS with the new model enabled us to have access to the evolution of internal parameters after each pass. We were able to compare the heterogeneity and evolution of microstructural parameters and also follow the evolution and localization of damage during the process. The model permits to capture the strength-ductility evolution. Interestingly, the increase in passes permits to homogenize the distribution of grain size (which is suitable to increase strength), but the porosity in the other hand is very localized in some small areas which is assumed to decrease ductility as it will promote strain localization.

The model developed can be used as an alternative to Voce or Swift type hardening models in Gurson's approach as it is valid for high strain deformations usually experienced during SPD. Furthermore it

can be used to follow locally the evolution of the microstructure (and therefore can be compared to experimental data such as EBSD maps). This model constitutes a first step toward a quantitative prediction of the strength-ductility trade-off because it is still restricted to moderate triaxiality levels and the modelling of coalescence is heuristic. Further developments of this approach should include (i) void shape effects that are important at low stress triaxiality and (ii) a micromechanical modelling of coalescence in order to capture precisely strain localization as a measure of ductility.

Chapter 5

Conclusion

5.1 General conclusion

The aim of this thesis was to investigate the strength and ductility of materials processed by severe plastic deformation, using numerical simulation. Special attention has been given to the evolution of damage during the deformation, as it can greatly influence the ductility and plays an important role in a possible optimization of the process. The focus of this thesis was particularly the application of SPD on sheet metals. In this context, three different cases were particularly investigated:

1. A conventional plastic deformation process, namely deep drawing, intentionally chosen due to moderately high plastic deformation in addition to low stress triaxiality, which requires a spacial treatment for the numerical modelling of damage evolution.

2. A case of SPD of sheet metals, called repetitive corrugation and straightening was considered. In a first attempt for numerical simulations, only one pass of RCS was analyzed and the evolution of damage was investigated.

3. Finally, by going one step further and as a first step toward the simulation of multi-pass SPD, a case of RCS with two passes was analyzed. This required the developement of a new model of material hardening which takes into account both damage and microstructural evolution.

The simulation of deep drawing process presented in Chapter 2, was made for two distinct process conditions, leading to "bottom" and "shear" cracks. In order to evaluate the damage in shear stress and low triaxiality, we considered an extended Gurson model called Madou-Leblond model, which includes

void shape effects. Numerical simulations based on experimental investigations found in the literature were performed and the results were consistent with the experiments: The crack locations and punch displacement to fracture for both bottom crack and shear crack conditions were predicted. In addition, the local evolution of damage showed important void shape effects, particularly around the location of the shear crack case where low triaxiality condition was dominating. The same simulations were performed with GTN model which does not take into account the void shape effects; for the case of shear crack, it was unable to predict the fracture and for the bottom crack, the fracture was predicted with some delays. This investigation proved the capacity of the ML model for structural calculation with low stress triaxiality.

The numerical simulation of RCS, as an example of multi-pattern SPD process was investigated in Chapter 3. In this chapter, two distinct cases of "ductile" and "brittle" (high and low ductility material) aluminium alloys were investigated. For performing the simulation of multi-pattern RCS, a reduced model based on a single pattern was developed, representing patterns located in the stabilized zone of the multi-pattern. The experimental results for one pass RCS process on "ductile" aluminium alloy did not lead to any fracture. Therefore in that case, a numerical simulation of one pass RCS was performed without damage evolution. In order to validate the numerical model, the residual stress obtained from the simulation was compared with the residual stress measured using X-ray diffraction method. Averaging effects caused by finite size of the XRD iradiated area were handled by developing a deconvolution method on the experimental measurements: the local and average stresses were linked by a linear relationship which permits to reconstruct the local fields. The quality of the results were enhanced by using two different colimator sizes and overlapping XRD measurement. The reconstructed residual stress obtained by deconvolution procedure were satisfactory with respect to the numerical results.

The experimental results with "brittle" aluminum alloy showed fracture during corrugation step. The ML model was used to simulate the process and the numerical simulation was able to predict the location and onset of fracture. Simulation with GTN model was also able to predict the fracture but with some delays. The results on one pass RCS indicates that GTN model could be appropriate for simulation of RCS process for ductile material provided that the triaxiality during this process remains quite high in the specimen which usually is the case, when the corrugation dies are stopped before complete squeezing of the sheet metal (before inducing shear deformation).

Finally, as a first step to simulate multi-pass SPD, two passes of RCS were studied in Chapter 4. In order to simulate the intense deformation happening during SPD (particularly at higher passes), a model based on cellular structure of dislocation densities was developed. Additionally, based on the results on ductile aluminium alloy previously obtained, this model was coupled with GTN model in order to investigate the evolution of damage during RCS. This model was assessed numerically under different initial conditions: numerical simulations in an axi-symmetrical loading have permitted to study the influence of initial void density and imposed triaxiality on the maximum grain refinement before coalescence. Finally, finite element analysis was performed using this model for simulation of two pass RCS on pure copper. Hence, the model was implemented in ABAQUS using a UMAT subroutine. The results permit to study the distribution of internal variables related to microstructure and evolution of damage in the first and second pass. The results showed that after the first pass, the maximum dislocation density and grain refinement have an abrupt evolution but the maximum values remain almost the same after the second pass; however, the homogeneity of the distribution of these variables in greatly increased. A numerical tensile test was performed after the RCS processing and it permits to qualitatively reproduce the strength and ductility of the experimental results.

5.2 Prospective

During this thesis, a numerical analysis of SPD process has been performed. Numerical models for deep drawing and RCS in one and two passes, along with several material hardening and damage models have been developed. These numerical framework and material models have been developed in order to improve our understanding of the evolution of the mechanical behavior of material during SPD and eventually, optimise process parameters to enhance the strength-ductility response of the processed materials. In this framework, several paths for continuation of this work can been envisaged:

- Several assumptions have been made in this work in order to simplify the material behavior. In the case of deep drawing, it was assumed that the material is isotropic and that the voids were initially spherical. In reality, most of the sheet metals have some degrees of anisotropy. By implementing an anisotropic hardening law in ML model, we will be able to consider anisotropic materials in the simulations. Also, by performing experimental analysis such as microtomography, we could account for the initial void shape distribution in the material.

- Eventually more passes of RCS process can be modeled to investigate higher levels of deformation and continue investigating the strength-ductility trade-off.

- In Chapter 4, we coupled GTN model with dislocation density model. The next step is to extend the ML model with dislocation density based hardening. This would permit us to consider SPD with more shear dominated loading. Another interesting process would be ECAP process. This process undergoes very high plastic deformation under low triaxiality thus using the ML model would be suitable in this case.

- The numerical models investigated in this thesis could be enriched by experimental investigations. This would let us better identify the model parameters and validate the numerical results such as, EBSD for grain and cell size distribution, microtomography for void growth and nucleation and SEM for fracture characterisation. Additionally, using XRD method on the processed experiments and comparing the results with the numerical ones could give us insight on the microsturucture change during the process. The peak width obtained by XRD after processing to remove instrumental broadening can give information about the crystal size and dislocation density. These features could be compared with the results obtained bythe model developed (based on dislocation densities) in order to calibrate the parameters and validate the numerical model.

References

[1] Ammar, A., 2010. The proper generalized decomposition: a powerful tool for model reduction. International Journal of Material Forming 3, 89–102.

[2] Azushima, A., Kopp, R., Korhonen, A., Yang, D.Y., Micari, F., Lahoti, G.D., Groche, P., Yanagimoto, J., Tsuji, N., Rosochowski, A., Yanagida, A., 2008. Severe plastic deformation (SPD) processes for metals. CIRP Annals 57, 716–735.

[3] Baczmanski, A., Braham, C., Seiler, W., Shiraki, N., 2004. Multi-reflection method and grazing incidence geometry used for stress measurement by X-ray diffraction. Surface and Coatings Technology 182, 43–54.

[4] Badreddine, H., Labergère, C., Saanouni, K., 2016. Ductile damage prediction in sheet and bulk metal forming. Comptes Rendus Mécanique 344, 296–318.

[5] Baik, S.C., Estrin, Y., Kim, H.S., Hellmig, R.J., 2003. Dislocation density-based modeling of deformation behavior of aluminium under equal channel angular pressing. Materials Science and Engineering: A 351, 86–97.

[6] Barlat, F., Glazov, M.V., Brem, J.C., Lege, D.J., 2002. A simple model for dislocation behavior, strain and strain rate hardening evolution in deforming aluminum alloys. International Journal of Plasticity 18, 919–939.

[7] Barsoum, I., Faleskog, J., 2007. Rupture mechanisms in combined tension and shear—Experiments. International Journal of Solids and Structures 44, 1768–1786.

[8] Ben Moussa, N., Sidhom, H., Braham, C., 2012. Numerical and experimental analysis of residual stress and plastic strain distributions in machined stainless steel. International Journal of Mechanical Sciences 64, 82–93.

[9] Ben Rhouma, A., Sidhom, N., Makhlouf, K., Sidhom, H., Braham, C., Gonzalez, G., 2019. Effect of machining processes on the residual stress distribution heterogeneities and their consequences on the stress corrosion cracking resistance of AISI 316l SS in chloride medium. The International Journal of Advanced Manufacturing Technology 105, 1699–1711.

[10] Benseddiq, N., Imad, A., 2008. A ductile fracture analysis using a local damage model. International Journal of Pressure Vessels and Piping 85, 219–227.

[11] Benzerga, A.A., 2002. Micromechanics of coalescence in ductile fracture. Journal of the Mechanics and Physics of Solids 50, 1331–1362.

[12] Benzerga, A.A., Besson, J., 2001. Plastic potentials for anisotropic porous solids. European Journal of Mechanics - A/Solids 20, 397–434.

[13] Benzerga, A.A., Leblond, J.B., 2010. Ductile fracture by void growth to coalescence. Advances in Applied Mechanics 44, 169–305.

[14] Benzerga, A.A., Leblond, J.B., 2014. Effective yield criterion accounting for microvoid coalescence. Journal of Applied Mechanics 81, 031009.

[15] Benzerga, A.A., Leblond, J.B., Needleman, A., Tvergaard, V., 2016. Ductile failure modeling. International Journal of Fracture 201, 29–80.

[16] Besson, J., 2010. Continuum Models of Ductile Fracture: A Review. International Journal of Damage Mechanics 19, 3–52.

[17] Bhovi, P.M., Gururaj, S.H., Lohit, R.B., Venkateswarlu, K., 2018. Simulation studies on RCS processed Al-Mg-Sc alloy. Materials Today: Proceedings 5, 7525–7531.

[18] Bhovi, P.M., Patil, D.C., Kori, S.A., Venkateswarlu, K., Huang, Y., Langdon, T.G., 2016. A comparison of repetitive corrugation and straightening and high-pressure torsion using an Al-Mg-Sc alloy. Journal of Materials Research and Technology 5, 353–359.

[19] Bong, H.J., Kim, D., Kwon, Y.N., Lee, J., 2021. Predicting hot deformation behaviors under multiaxial loading using the Gurson-Tvergaard-Needleman damage model for Ti–6al–4v alloy sheets. European Journal of Mechanics - A/Solids 87, 104227.

[20] Bonora, N., 1997. A nonlinear CDM model for ductile failure. Engineering Fracture Mechanics 58, 11–28.

[21] Cai, Z.Y., Meng, B., Wan, M., Wu, X.D., Fu, M.W., 2020. A modified yield function for modeling of the evolving yielding behavior and micro-mechanism in biaxial deformation of sheet metals. International Journal of Plasticity 129, 102707.

[22] Cao, Y., Ni, S., Liao, X., Song, M., Zhu, Y., 2018. Structural evolutions of metallic materials processed by severe plastic deformation. Materials Science and Engineering: R: Reports 133, 1–59.

[23] Chinesta, F., Ladeveze, P., Cueto, E., 2011. A Short Review on Model Order Reduction Based on Proper Generalized Decomposition. Archives of Computational Methods in Engineering 18, 395–404.

[24] Chu, C.C., Needleman, A., 1980. Void Nucleation Effects in Biaxially Stretched Sheets. Journal of Engineering Materials and Technology 102, 249–256.

[25] Dorhmi, K., Derrien, K., Hadjem-Hamouche, Z., Morin, L., Bonnet, F., Chevalier, J.P., 2021. Experimental study and micromechanical modelling of the effective elastic properties of fe–TiB2 composites. Composite Structures 272.

[26] Dorhmi, K., Morin, L., Derrien, K., Hadjem-Hamouche, Z., Chevalier, J.P., 2020. A homogenization-based damage model for stiffness loss in ductile metal-matrix composites. Journal of the Mechanics and Physics of Solids 137, 103812.

[27] Dunand, M., Mohr, D., 2011a. On the predictive capabilities of the shear modified Gurson and the modified Mohr–Coulomb fracture models over a wide range of stress triaxialities and Lode angles. Journal of the Mechanics and Physics of Solids 59, 1374–1394.

[28] Dunand, M., Mohr, D., 2011b. Optimized butterfly specimen for the fracture testing of sheet materials under combined normal and shear loading. Engineering Fracture Mechanics 78, 2919–2934.

[29] Elizalde, S., Ezequiel, M., Figueroa, I.A., Cabrera, J.M., Braham, C., Gonzalez, G., 2020.

Microstructural Evolution and Mechanical Behavior of an Al-6061 Alloy Processed by Repetitive Corrugation and Straightening. Metals 10, 489.

[30] Enakoutsa, K., Leblond, J., Perrin, G., 2007. Numerical implementation and assessment of a phenomenological nonlocal model of ductile rupture. Computer Methods in Applied Mechanics and Engineering 196, 1946–1957.

[31] Estrin, Y., Mecking, H., 1984. A unified phenomenological description of work hardening and creep based on one-parameter models. Acta Metallurgica 32, 57–70.

[32] Estrin, Y., Tóth, L.S., Bréchet, Y., Kim, H.S., 2006. Modelling of the evolution of dislocation cell misorientation under severe plastic deformation. Materials Science Forum Conference Name: Nanomaterials by Severe Plastic Deformation ISBN: 9780878499854 ISSN: 1662-9752 Pages: 675-680 Publisher: Trans Tech Publications Ltd Volume: 503-504.

[33] Estrin, Y., Tóth, L.S., Molinari, A., Bréchet, Y., 1998. A dislocation-based model for all hardening stages in large strain deformation. Acta Materialia 46, 5509–5522.

[34] Estrin, Y., Vinogradov, A., 2013. Extreme grain refinement by severe plastic deformation: A wealth of challenging science. Acta Materialia 61, 782–817.

[35] Ezequiel, M., Figueroa, I.A., Elizalde, S., Cabrera, J.M., Braham, C., Morin, L., Gonzalez, G., 2020. Numerical and experimental study of a 5754-aluminum alloy processed by heterogeneous repetitive corrugation and straightening. Journal of Materials Research and Technology 9, 1941–1947.

[36] Fang, Z.C., Wu, Z.L., Huang, C.G., Wu, C.W., 2020. Review on residual stress in selective laser melting additive manufacturing of alloy parts. Optics & Laser Technology 129, 106283.

[37] Flandi, L., Leblond, J.B., 2005. A new model for porous nonlinear viscous solids incorporating void shape effects – i: Theory. European Journal of Mechanics - A/Solids 24, 537–551.

[38] Garcia, D., 2010. Robust smoothing of gridded data in one and higher dimensions with missing values. Computational Statistics & Data Analysis 54, 1167–1178.

[39] Ghahremaninezhad, A., Ravi-Chandar, K., 2013. Ductile failure behavior of polycrystalline Al 6061-T6 under shear dominant loading. International Journal of Fracture 180, 23–39.

[40] Gologanu, M., 1997. Etude de quelques problèmes de rupture ductile des métaux. Ph.D. thesis. Université Paris 6.

[41] Gorji, M., 2015. Instability and Fracture Models to Optimize the Metal Forming and Bending Crack Behavior of Al-Alloy Composites. Ph.D. thesis. ETH-Zürich.

[42] Gorji, M., Berisha, B., Hora, P., Barlat, F., 2016a. Modeling of localization and fracture phenomena in strain and stress space for sheet metal forming. International Journal of Material Forming 9, 573–584.

[43] Gorji, M., Berisha, B., Manopulo, N., Hora, P., 2016b. Effect of through thickness strain distribution on shear fracture hazard and its mitigation by using multilayer aluminum sheets. Journal of Materials Processing Technology 232, 19–33.

[44] Gorji, M.B., Mohr, D., 2018. Predicting shear fracture of aluminum 6016-T4 during deep drawing: Combining Yld-2000 plasticity with Hosford–Coulomb fracture model. International Journal of Mechanical Sciences 137, 105–120.

[45] Grolleau, V., Roth, C.C., Mohr, D., 2022. Design of in-plane torsion experiment to characterize anisotropic plasticity and fracture under simple shear. International Journal of Solids and Structures 236-237, 111341.

[46] Gu, C.F., Tóth, L.S., Beausir, B., 2012. Modeling of large strain hardening during grain refinement. Scripta Materialia 66, 250–253.

[47] Gurson, A.L., 1977. Continuum theory of ductile rupture by void nucleation and growth: Part I–Yield criteria and flow rules for porous ductile media. ASME Journal of Engineering Materials and Technology 99, 2–15.

[48] Hadoush, A., van den Boogaard, A., 2008. Time reduction in implicit single point incremental sheet forming simulation by refinement - derefinement. International Journal of Material Forming 1, 1167–1170.

[49] Hajizadeh, K., Ejtemaei, S., Eghbali, B., 2017. Microstructure, hardness homogeneity, and tensile properties of 1050 aluminum processed by constrained groove pressing. Appl. Phys. A 123, 504.

[50] Halphen, B., Nguyen, Q.S., 1975. Generalized standard materials. Journal de mécanique 14, 39–63.

[51] Haltom, S.S., Kyriakides, S., Ravi-Chandar, K., 2013. Ductile failure under combined shear and tension. International Journal of Solids and Structures 50, 1507–1522.

[52] Hennion, V., Sprauel, J.M., Michaud, H., 2000. Contribution to residual-stress evaluation in high-stress-gradient zones by X-ray diffraction. Journal of Applied Crystallography 33, 26–34.

[53] Hosseini, E., Kazeminezhad, M., 2009. A hybrid model on severe plastic deformation of copper. Computational Materials Science 44, 1107–1115.

[54] Huang, J.Y., Zhu, Y.T., Jiang, H., Lowe, T.C., 2001. Microstructures and dislocation configurations in nanostructured Cu processed by repetitive corrugation and straightening. Acta Materialia 49, 1497–1505.

[55] Huang, Y., Langdon, T.G., 2013. Advances in ultrafine-grained materials. Materials Today 16, 85–93.

[56] Inoue, T., Tsuji, N., 2009. Quantification of strain in accumulative roll-bonding under unlubricated condition by finite element analysis. Computational Materials Science 46, 261–266.

[57] Kahloun, C., Badawi, P., Viaris de Lesegno, P., 1994. X-ray Analysis. The case of substantial stress gradients and strong heterogeneity, in: Proceedings of the 4th International Conference on Residual Stresses, Baltimore, Maryland, USA.

[58] Kahloun, C., Badji, R., Queyreau, S., Franciosi, P., Bacroix, B., 2014. Spatial Convolution of a Stress Field Analyzed by X-Ray Diffraction.

[59] Kami, A., Dariani, B.M., Sadough Vanini, A., Comsa, D.S., Banabic, D., 2015. Numerical determination of the forming limit curves of anisotropic sheet metals using GTN damage model. Journal of Materials Processing Technology 216, 472–483.

[60] Kami, A., Dariani, B.M., Vanini, A.S., Comsa, D.S., Banabic, D., 2014. Application of a GTN damage model to predict the fracture of metallic sheets subjected to deep-drawing. Proceedings of the Romanian Academy, Series A 15.

[61] Kawasaki, M., Horita, Z., Langdon, T.G., 2009. Microstructural evolution in high purity aluminum processed by ECAP. Materials Science and Engineering: A 524, 143–150.

[62] Kerfriden, P., Passieux, J.C., Bordas, S.P.A., 2012. Local/global model order reduction strategy for the simulation of quasi-brittle fracture. International Journal for Numerical Methods in Engineering 89, 154–179.

[63] Khodabakhshi, A.R., Kazeminezhad, M., 2019. Effects of non-isothermal annealing on microstructure and mechanical properties of severely deformed aluminum samples: Modeling and experiment. Transactions of Nonferrous Metals Society of China 29, 1127–1137.

[64] Kotkunde, N., Deole, A.D., Gupta, A.K., Singh, S.K., Aditya, B., 2014. Failure and formability studies in warm deep drawing of ti–6al–4v alloy. Materials & Design 60, 540–547.

[65] Lapovok, R., Dalla Torre, F.H., Sandlin, J., Davies, C.H.J., Pereloma, E.V., Thomson, P.F., Estrin, Y., 2005. Gradient plasticity constitutive model reflecting the ultrafine micro-structure scale: the case of severely deformed copper. Journal of the Mechanics and Physics of Solids 53, 729–747.

[66] Leblond, J.B., 2015. UMAT available at the address www.dalembert.upmc.fr/home/leblond/.

[67] Leblond, J.B., Perrin, G., Suquet, P., 1994. Exact results and approximate models for porous viscoplastic solids. International Journal of Plasticity 10, 213–235.

[68] Lee, B.H., Keum, Y.T., Wagoner, R.H., 2002. Modeling of the friction caused by lubrication and surface roughness in sheet metal forming. Journal of Materials Processing Technology 130-131, 60–63.

[69] Leggatt, R.H., 2008. Residual stresses in welded structures. International Journal of Pressure Vessels and Piping 85, 144–151.

[70] Lehto, P., 2021. Adaptive domain misorientation approach for the EBSD measurement of deformation induced dislocation sub-structures. Ultramicroscopy 222, 113203.

[71] Lemaitre, J., 1985. A Continuous Damage Mechanics Model for Ductile Fracture. Journal of Engineering Materials and Technology 107, 83–89.

[72] Lu, J., 1996. Handbook of Measurement of Residual Stresses. Fairmont Press.

[73] Madou, K., Leblond, J.B., 2012a. A Gurson-type criterion for porous ductile solids containing arbitrary ellipsoidal voids—I: Limit-analysis of some representative cell. Journal of the Mechanics and Physics of Solids 60, 1020–1036.

[74] Madou, K., Leblond, J.B., 2012b. A Gurson-type criterion for porous ductile solids containing arbitrary ellipsoidal voids—II: Determination of yield criterion parameters. Journal of the Mechanics and Physics of Solids 60, 1037–1058.

[75] Madou, K., Leblond, J.B., 2013. Numerical studies of porous ductile materials containing arbitrary ellipsoidal voids—I: Yield surfaces of representative cells. European Journal of Mechanics - A/Solids 42, 480–489.

[76] Madou, K., Leblond, J.B., Morin, L., 2013. Numerical studies of porous ductile materials containing arbitrary ellipsoidal voids—II: Evolution of the length and orientation of the void axes. European Journal of Mechanics - A/Solids 42, 490–507.

[77] Mahmoudi, A.H., Ghasemi, A., Farrahi, G.H., Sherafatnia, K., 2016. A comprehensive experimental and numerical study on redistribution of residual stresses by shot peening. Materials & Design 90, 478–487.

[78] Maire, E., Carmona, V., Courbon, J., Ludwig, W., 2007. Fast x-ray tomography and acoustic emission study of damage in metals during continuous tensile tests. Acta Materialia 55, 6806–6815.

[79] Marciszko, M., Baczmański, A., Braham, C., Wróbel, M., Wroński, S., Cios, G., 2017. Stress measurements by multi-reflection grazing-incidence X-ray diffraction method (MGIXD) using different radiation wavelengths and different incident angles. Acta Materialia 123, 157–166.

[80] Mckenzie, P.W.J., Lapovok, R., Estrin, Y., 2007. The influence of back pressure on ECAP processed AA 6016: Modeling and experiment. Acta Materialia 55, 2985–2993.

[81] Mecking, H., Kocks, U.F., 1981. Kinetics of flow and strain-hardening. Acta Metallurgica 29, 1865–1875.

[82] Morin, L., Braham, C., Tajdary, P., Seddik, R., Gonzalez, G., 2021. Reconstruction of heterogeneous surface residual-stresses in metallic materials from X-ray diffraction measurements. Mechanics of Materials 158, 103882.

[83] Morin, L., Leblond, J.B., Mohr, D., Kondo, D., 2017a. Prediction of shear-dominated ductile fracture in a butterfly specimen using a model of plastic porous solids including void shape effects. European Journal of Mechanics - A/Solids 61, 433–442.

[84] Morin, L., Leblond, J.B., Tvergaard, V., 2016. Application of a model of plastic porous materials including void shape effects to the prediction of ductile failure under shear-dominated loadings. Journal of the Mechanics and Physics of Solids 94, 148–166.

[85] Morin, L., Michel, J.C., Leblond, J.B., 2017b. A Gurson-type layer model for ductile porous solids with isotropic and kinematic hardening. International Journal of Solids and Structures 118, 167–178.

[86] Mughrabi, H., 1983. Dislocation wall and cell structures and long-range internal stresses in deformed metal crystals. Acta Metallurgica 31, 1367–1379.

[87] Nahrmann, M., Matzenmiller, A., 2021. Modelling of nonlocal damage and failure in ductile steel sheets under multiaxial loading. International Journal of Solids and Structures 232, 111166.

[88] Nahshon, K., Hutchinson, J.W., 2008. Modification of the Gurson model for shear failure. European Journal of Mechanics - A/Solids 27, 1–17.

[89] Nelson, D., 1981. Effects of Residual Stress on Fatigue Crack Propagation, in: Residual stress effects in fatigue, Astm stp 776. american society for testing and materials edition.

[90] Nes, E., 1997. Modelling of work hardening and stress saturation in FCC metals. Progress in Materials Science 41, 129–193.

[91] Nielsen, K.L., Dahl, J., Tvergaard, V., 2012. Collapse and coalescence of spherical voids subject to intense shearing: studied in full 3d. International Journal of Fracture 177, 97–108.

[92] Niroomandi, S., Alfaro, I., Cueto, E., Chinesta, F., 2008. Real-time deformable models of non-linear tissues by model reduction techniques. Computer Methods and Programs in Biomedicine 91, 223–231.

[93] Nor, F.M., Osman, N., Kurniawan, D., 2020. Finite element analysis of repetitive corrugation and straightening die designs for severe plastic deformation of magnesium alloy. AIP Conference Proceedings 2262, 030017.

[94] Pack, K., Tancogne-Dejean, T., Gorji, M.B., Mohr, D., 2018. Hosford-Coulomb ductile failure model for shell elements: Experimental identification and validation for DP980 steel and aluminum 6016-T4. International Journal of Solids and Structures 151, 214–232.

[95] Pandya, K.S., Roth, C.C., Mohr, D., 2020. Strain rate and temperature dependent fracture of aluminum alloy 7075: Experiments and neural network modeling. International Journal of Plasticity 135, 102788.

[96] Peyre, P., Fabbro, R., 1995. Laser shock processing: a review of the physics and applications. Optical and Quantum Electronics 27, 1213–1229.

[97] Pineau, A., Benzerga, A.A., Pardoen, T., 2016. Failure of metals i: Brittle and ductile fracture. Acta Materialia 107, 424–483.

[98] Ponte Castañeda, P., Zaidman, M., 1994. Constitutive models for porous materials with evolving microstructure. Journal of the Mechanics and Physics of Solids 42, 1459–1497.

[99] Prinz, F.B., Argon, A.S., 1984. The evolution of plastic resistance in large strain plastic flow of single phase subgrain forming metals. Acta Metallurgica 32, 1021–1028.

[100] Rahimi, F., Sadeghi, B.M., Ahmadi, M., 2018. Finite element analysis of the deformation behaviour of pure aluminium in repetitive corrugation-straightening and constrained groove pressing. International Journal of Manufacturing Technology and Management 32, 598–609.

[101] Rollett, A., Kocks, F., 1994. A review of the stages of work hardening. Solid State Phenomena 35, 1–18.

[102] Rossini, N.S., Dassisti, M., Benyounis, K.Y., Olabi, A.G., 2012. Methods of measuring residual stresses in components. Materials & Design 35, 572–588.

[103] Roth, C.C., Morgeneyer, T.F., Cheng, Y., Helfen, L., Mohr, D., 2018. Ductile damage mechanism under shear-dominated loading: In-situ tomography experiments on dual phase steel and localization analysis. International Journal of Plasticity 109, 169–192.

[104] Ryckelynck, D., Chinesta, F., Cueto, E., Ammar, A., 2006. On the a priori model reduction: Overview and recent developments. Archives of Computational Methods in Engineering 13, 91–128.

[105] Saanouni, K., 2008. On the numerical prediction of the ductile fracture in metal forming. Engineering Fracture Mechanics 75, 3545–3559.

[106] Saanouni, K., Nesnas, K., Hammi, Y., 2000. Damage Modeling in Metal Forming Processes. International Journal of Damage Mechanics 9, 196–240.

[107] Saxena, R.K., Dixit, P.M., 2011. Numerical analysis of damage for prediction of fracture initiation in deep drawing. Finite Elements in Analysis and Design 47, 1104–1117.

[108] Shin, D.H., Park, J.J., Kim, Y.S., Park, K.T., 2002. Constrained groove pressing and its application to grain refinement of aluminum. Materials Science and Engineering: A 328, 98–103.

[109] Shirdel, A., Khajeh, A., Moshksar, M.M., 2010. Experimental and finite element investigation of semi-constrained groove pressing process. Materials & Design 31, 946–950.

[110] Soyarslan, C., Tekkaya, A.E., 2010. A damage coupled orthotropic finite plasticity model for sheet metal forming: CDM approach. Computational Materials Science 48, 150–165.

[111] Springmann, M., Kuna, M., 2005. Identification of material parameters of the Gurson–Tvergaard–Needleman model by combined experimental and numerical techniques. Computational Materials Science 33, 501–509.

[112] Tancogne-Dejean, T., Roth, C.C., Morgeneyer, T.F., Helfen, L., Mohr, D., 2021. Ductile damage of AA2024-t3 under shear loading: Mechanism analysis through in-situ laminography. Acta Materialia 205, 116556.

[113] Teixeira, P., Santos, A.D., Andrade Pires, F.M., César de Sá, J.M.A., 2006. Finite element prediction of ductile fracture in sheet metal forming processes. Journal of Materials Processing Technology 177, 278–281.

[114] Tekkaya, A.E., Bouchard, P.O., Bruschi, S., Tasan, C.C., 2020. Damage in metal forming. CIRP Annals 69, 600–623.

[115] Thangapandian, N., Balasivanandha Prabu, S., Padmanabhan, K.A., 2016. Effects of die profile on grain refinement in Al–Mg alloy processed by repetitive corrugation and straightening. Materials Science and Engineering: A 649, 229–238.

[116] Thuillier, S., Maire, E., Brunet, M., 2012. Ductile damage in aluminium alloy thin sheets: Correlation between micro-tomography observations and mechanical modeling. Materials Science and Engineering: A 558, 217–225.

[117] Torkestani, A., Dashtbayazi, M.R., 2018. A new method for severe plastic deformation of the copper sheets. Materials Science and Engineering: A 737, 236–244.

[118] Torki, M.E., Benzerga, A.A., 2018. A mechanism of failure in shear bands. Extreme Mechanics Letters 23, 67–71.

[119] Tvergaard, V., 1981. Influence of voids on shear band instabilities under plane strain conditions. International Journal of Fracture 17, 389–407.

[120] Tvergaard, V., Needleman, A., 1984. Analysis of the cup-cone fracture in a round tensile bar. Acta metallurgica 32, 157–169.

[121] Tóth, L.S., Estrin, Y., Lapovok, R., Gu, C., 2010. A model of grain fragmentation based on lattice curvature. Acta Materialia 58, 1782–1794.

[122] Tóth, L.S., Gu, C., 2014. Ultrafine-grain metals by severe plastic deformation. Materials Characterization 92, 1–14.

[123] Tóth, L.S., Molinari, A., Estrin, Y., 2001. Strain hardening at large strains as predicted by dislocation based polycrystal plasticity model. Journal of Engineering Materials and Technology 124, 71–77.

[124] Ungár, T., Tóth, L.S., Illy, J., Kovács, I., 1986. Dislocation structure and work hardening in polycrystalline ofhc copper rods deformed by torsion and tension. Acta Metallurgica 34, 1257–1267.

[125] Uthaisangsuk, V., Prahl, U., Münstermann, S., Bleck, W., 2008. Experimental and numerical failure criterion for formability prediction in sheet metal forming. Computational Materials Science 43, 43–50.

[126] Vaara, J., Kunnari, A., Frondelius, T., 2020. Literature review of fatigue assessment methods in residual stressed state. Engineering Failure Analysis 110, 104379.

[127] Valiev, R.Z., Islamgaliev, R.K., Alexandrov, I.V., 2000. Bulk nanostructured materials from severe plastic deformation. Progress in materials science 45, 103–189.

[128] Webster, G.A., Ezeilo, A.N., 2001. Residual stress distributions and their influence on fatigue lifetimes. International Journal of Fatigue 23, 375–383.

[129] Xiao, X., Tong, X., Liu, Y., Zhao, R., Gao, G., Li, Y., 2018. Prediction of shot peen forming effects with single and repeated impacts. International Journal of Mechanical Sciences 137, 182–194.

[130] Yang, Z., Zhao, C., Dong, G., Chen, Z., 2021. Experimental calibration of ductile fracture parameters and forming limit of AA7075-T6 sheet. Journal of Materials Processing Technology 291, 117044.

[131] Ying, L., Wang, D.t., Liu, W.q., Wu, Y., Hu, P., 2018. On the numerical implementation of a shear modified GTN damage model and its application to small punch test. International Journal of Material Forming 11, 527–539.

[132] Zehetbauer, M., Seumer, V., 1993. Cold work hardening in stages IV and v of f.c.c. metals—i. experiments and interpretation. Acta Metallurgica et Materialia 41, 577–588.

[133] Zenasni, Z., Haterbouch, M., Atmani, Z., Atlati, S., Zenasni, M., Nasri, K., Oussouaddi, O., 2019. Physics-based plasticity model incorporating microstructure changes for severe plastic deformation. Comptes Rendus Mécanique 347, 601–614.

[134] Zhang, K., Badreddine, H., Yue, Z., Hfaiedh, N., Saanouni, K., Liu, J., 2021. Failure prediction of magnesium alloys based on improved CDM model. International Journal of Solids and Structures 217-218, 155–177.

[135] Zhang, Z., Wu, Y., Huang, F., 2022. Extension of a shear-controlled ductile fracture criterion by considering the necking coalescence of voids. International Journal of Solids and Structures 236-237, 111324.

Appendix A

Reduced-single pattern RCS model

A.1 Motivation

The numerical simulations of RCS are demanding in terms of computational capacities because of the non-linearities involved (large strains, contact conditions, damage, etc.), the size of the specimens processed and the large set of processing conditions (die shape, friction, loading conditions, number of passes, etc). In particular, since in practice possible industrial RCS corrugation die can contain thousands of elementary patterns, an important difficulty in the simulation of RCS is the large number of patterns which necessitates a large number of elements. The development of an efficient numerical model for RCS processing is thus appealing in order to reduce the computational time and facilitate the optimization of the process.

The reduction of calculation cost can be achieved using several techniques. Among those techniques, model-order reduction in mechanical engineering usually refers to various numerical strategies that have been introduced to circumvent challenging scenarios in numerical simulations including process control, parametric modeling, inverse identification, and process or shape optimization [1, 23, 62, 104]. Those methods are very efficient in problems involving small strains but their extension to finite deformation remains scarce [92]. Furthermore, they are generally based on a modal decomposition of the solution which is determined *globally* and thus does not take into account the geometrical specificities of the structure (such as the repetition of a pattern). Hence, in several non-linear processes involving geometrical features, alternative strategies closely related to the process considered are generally employed: e.g. in single point incremental sheet forming a refinement-derefinement technique was used to reduce computational time [48], in orthogonal cutting process a model based on

a reduction of the geometry was proposed to simulate the process [8] and in shot peening processing a model based on two shots was proposed to model random shot peening [129]. In the case of RCS, an important feature is the repetition of the corrugation die pattern, therefore the development of a reduced geometrical model, based on a single pattern, is interesting to improve the computational cost of the process.

A.2 Numerical modelling of multi-pattern RCS

A numerical model for the multi-pattern RCS process is developed in order to provide a reference solution which will be useful to assess the reduced model. Several non-linearities involved in the process such as large plastic strains and contact conditions between the sheet and the dies will be studied. In this work we will assume that the out-of-plane direction is long enough so 2D plane-strain conditions are applicable for the process.

Although the shape of the corrugation die highly affects the distribution of deformation during RCS process [55], the aim of this work is not to compare several corrugation shapes, so the most simple shape will be considered. The geometrical model considered, represented in Figure A.1, is thus composed of several corrugation patterns of circular shape (with 6 mm radius) and the width of one pattern is taken as $L = 20$ mm. In the following of the paper, we refer to each corrugation die pattern and the part of the workpiece directly deformed by it, as one pattern of the process (as in Figure 1.7). The workpiece thickness is taken as 1 mm.

Since this RCS processing is usually performed in quasi-static conditions, an elastic-plastic model without strain rate effects is considered for the sheet. Moreover, an isotropic behavior is considered in this work. Thus, the material model is supposed to follow a J2 isotropic plasticity model with isotropic hardening. The yield stress σ_y follows a power-law of the form

$$\sigma_y = \sigma_0 + hp^n, \tag{A.1}$$

where σ_y is the flow stress and p is the accumulated plastic strain. For the simulations, an aluminum alloy AA5083 is chosen because of its good ductility and formability which makes this alloy a suitable candidate for severe plastic deformation [35]. The following values, obtained from the stress-strain curve in a tensile test, are thus considered for the material parameters:

$\sigma_0 = 160$ MPa, $h = 180$ MPa and $n = 0.35$.

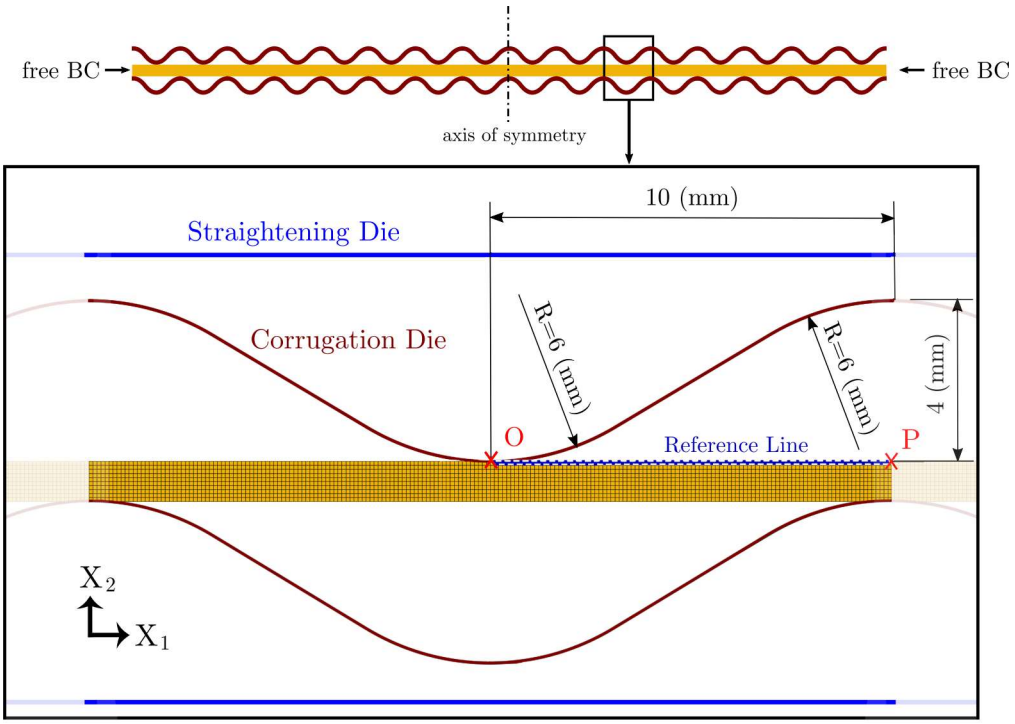

Figure A.1: Finite element model of multi-pattern RCS (with 16 patterns for illustrative purposes) with an enlarged view on one pattern with dimensions. Reference line OP and reference point P labeled on the figure will be used for the study of the mechanical and geometrical fields.

Moreover, the corrugation and straightening dies made from high strength steel can be modeled as rigid wires (in the two dimensional model).

The friction between the dies and the sheet is accounted for by a Coulomb friction model in which the frictional force is related to the normal pressure applied on the surface. According to literature, the friction coefficient f between aluminum (sample) and steel (die) depends on the amount and type of lubrication used, and its calibration is not an easy task. Thus, in this paper, we will use several values for the friction coefficient in order to study different lubrication conditions: $f = [0.1,\ 0.25,\ 0.5,\ 0.75]$.

For the full multi-pattern model, a corrugation die consisting of 50 patterns was used. Since both lateral edges of the sheet are free (see Figure A.1), the model has a plane of symmetry in its middle. It can thus be modelled by using only half of the patterns (here 25 patterns) with a symmetric boundary condition imposed on the left edge of the workpiece (blocking its movement in x_1-direction) and a free boundary condition on its right edge. The numerical simulation has been performed with the finite element code Abaqus/Standard. In practice, four (implicit) steps are considered: (S1)

corrugation, (S1R) redistribution of stress after corrugation (unloading), (S2) straightening and (S2R) redistribution of stress after straightening (unloading). The workpiece is meshed with 50000 4-node reduced-integration plane-strain elements (C4PER Abaqus elements) of square shape with an element size of about 0.1 mm; a mesh sensitivity analysis has been performed and this mesh was found to provide converged results. Finally, a loading force of 10 kN is used in the model, which is representative of experimental conditions. In the following, this model (with 50 patterns) will be termed as the *full multi-pattern model*.

A.2.1 Preliminary stabilization analysis of mechanical fields

Due to the repetition of the elementary pattern, the mechanical fields are *expected* to stabilize in the patterns far from the free boundary.

First, as an illustrative example, a calculation is performed for a friction coefficient $f = 0.25$ and the distribution of the longitudinal stress σ_{11} is represented in Figure A.2 in several patterns at the last step of the simulation (after the final stress redistribution). Interestingly, the stress distribution in the first patterns (on the left) is the same and is different from that near the free boundary. Those results seem to indicate the existence of a stabilized section in the middle of the specimen (left side of the figure) and away from the free edge (right side of the figure).

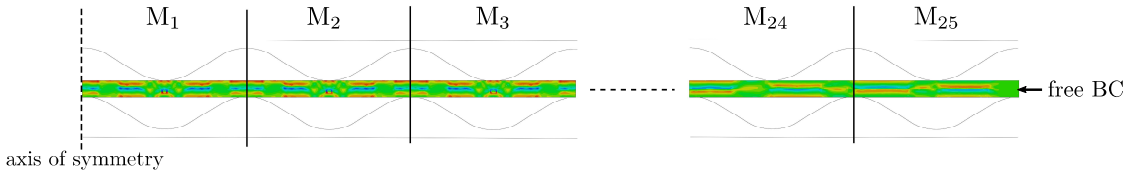

Figure A.2: Distribution of the longitudinal stress σ_{11} at the end of the simulation of the full multi-pattern model (with 2×25 patterns).

Quantitative distributions of the equivalent plastic strain (PEEQ) and von Mises equivalent stress (σ_{eq}) are then provided on the upper line of the specimen[1] (defined in Figure A.1) of several patterns (still at the last step of the process), in Figures A.3 and A.4, respectively. Interestingly, the distribution of the equivalent plastic strain appears to be the same from pattern M_1 to M_{17}, which confirms that a stabilization of the mechanical fields occurs far from the free boundary. A similar behavior is observed for the equivalent stress although there is a slight difference between the stress distributions from

[1]Only the right half of each pattern are investigated due to the fact that the stress and strain values in each pattern are almost symmetric because of the the symmetric form of corrugation die patterns.

pattern M_1 to M_{17} which is not surprising as the residual stresses are very sensitive to small variations of the equivalent plastic strain.

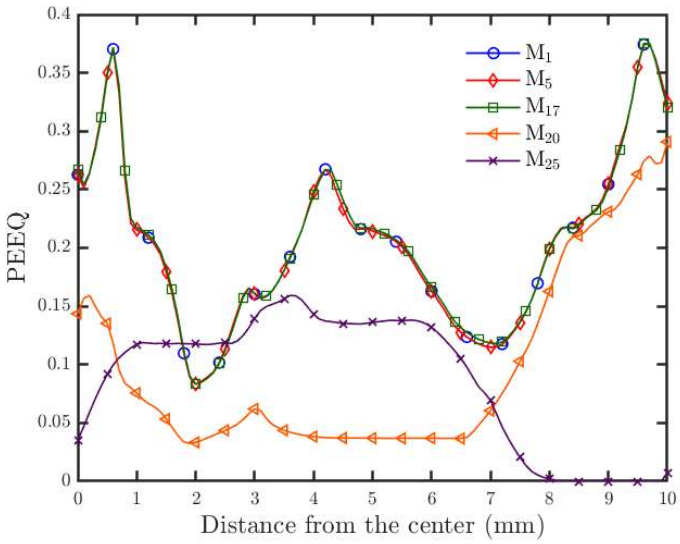

Figure A.3: Distribution of the equivalent plastic strain (PEEQ) on the upper line (line OP in Figure A.1) of the specimen for several patterns at the last step of the process.

Away from the introduced stabilized section, the strain and stress patterns change abruptly. As a result, it will not be possible to develop a representative model in the transient section (in this case from pattern M_{18} to M_{25}). On the other hand, it appears possible to develop a reduced model to reproduce the mechanical behavior in the patterns of the stabilized section of the process (in this case from pattern M_1 to M_{17}) and this is the objective of this paper.

A.2.2 Influence of the friction coefficient on the stabilization of the mechanical fields

In forming processes, the friction coefficient between the specimen and the dies has a great influence on the deformation and the mechanical fields [68]. It is thus of interest to investigate its influence on the stabilization behavior. In particular, we study the stabilization behavior of the residual stress field (since residual stresses are prominent in structural integrity of sheets) and the plastic strain field (as it is related to the mechanism of grain refinement induced by severe plastic deformation).

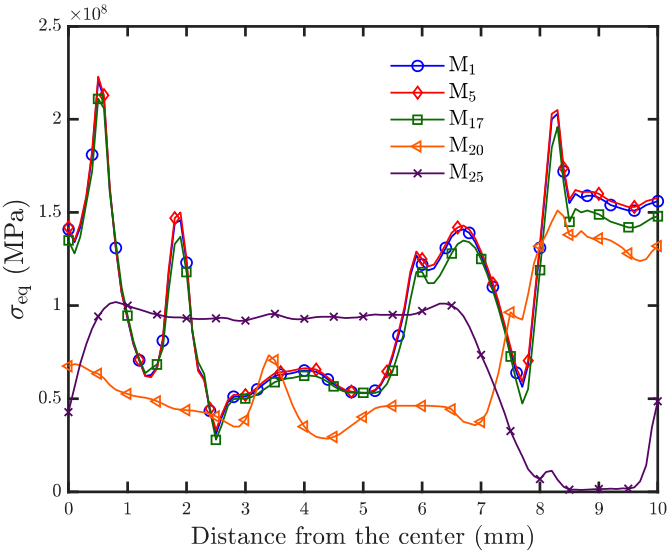

Figure A.4: Distribution of the von Mises equivalent stress (σ_{eq}) on the upper line (line OP in Figure A.1) of the specimen for several patterns at the last step of the process.

First, a normalized stabilization criterion *for stress* (denoted by Δ^i_σ) is introduced to study this variation. This criterion is taken as a volume average of the difference between the von Mises equivalent stress in pattern M_i and that in pattern M_1 taken on the initial (reference) configuration:

$$\Delta^i_\sigma = \frac{\langle |\sigma^{M_1}_{eq} - \sigma^{M_i}_{eq}| \rangle_{\Omega_0}}{|\langle \sigma^{M_1}_{eq} \rangle_{\Omega_0}|}, \tag{A.2}$$

where $\langle \cdot \rangle_{\Omega_0}$ is the spatial average over the initial (non-deformed) configuration (denoted by Ω_0) given by

$$\langle f \rangle = \frac{1}{\text{vol}(\Omega_0)} \int_{\Omega_0} f \, \mathrm{d}\Omega. \tag{A.3}$$

This criterion permits to take into consideration the spatial fluctuation of the von Mises stress within a pattern. Since each pattern may have slight differences in term of their geometry, the average is computed on the initial configuration which is the same for all patterns.

Similarly, a normalized stabilization criterion *for plastic strain* can be also introduced (denoted by Δ^i_ϵ), as a the average of the difference between the accumulated plastic strain in pattern M_i and that in pattern M_1 taken again on the initial (reference) configuration:

$$\Delta^i_\epsilon = \frac{\langle |p^{M_1}_{eq} - p^{M_i}_{eq}| \rangle_{\Omega_0}}{|\langle p^{M_1}_{eq} \rangle_{\Omega_0}|}, \tag{A.4}$$

where p_{eq} is the local accumulated plastic strain (PEEQ in Abaqus). Both criteria will be used to quantify the stabilization of the mechanical fields within the full multi-pattern model.

The stress stabilization criterion Δ_σ^i is represented in Figure A.5 at the end of the simulation (after stress redistribution), for different values of friction coefficient. This permits to highlight the occurrence of the stabilization of the mechanical fields, which depends on the friction coefficient. We define the minimum (approximate) number of patterns required to achieve stabilization, denoted by N_s and characterizing the transient section, as the total number of patterns for which Δ_σ^i is higher than a tolerance value which is taken as 3%. Interestingly, this number N_s increases when the friction coefficient f decreases. This behavior can be qualitatively explained by the fact that small values of the friction coefficient allows a larger amplitude in the longitudinal displacement and consequently, it 'takes' more patterns to achieve stabilization, while an important value of the friction coefficient 'locks' the sheet so a large number of patterns are constrained with the same kinematic conditions.

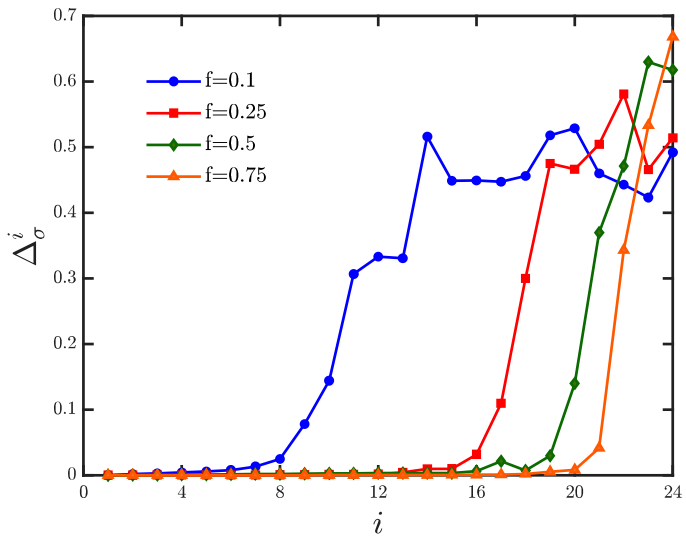

Figure A.5: Stabilization criteria for residual stress calculated after the redistribution (unloading) step as a function of different friction coefficient in the full multi-pattern model.

For completeness, the number of patterns required to achieve stabilization N_s (i.e. the length of the transient section) is represented in Figure A.6 for both stress (Δ_σ^i) and strain (Δ_ϵ^i) criteria, as a function of the friction coefficient at the end of each step (S1, S1R, S2 and S2R). It should be noted

that since the accumulated plastic strain does not evolve during unloading, the criteria Δ_ϵ^i is only represented at the steps S1 and S2.

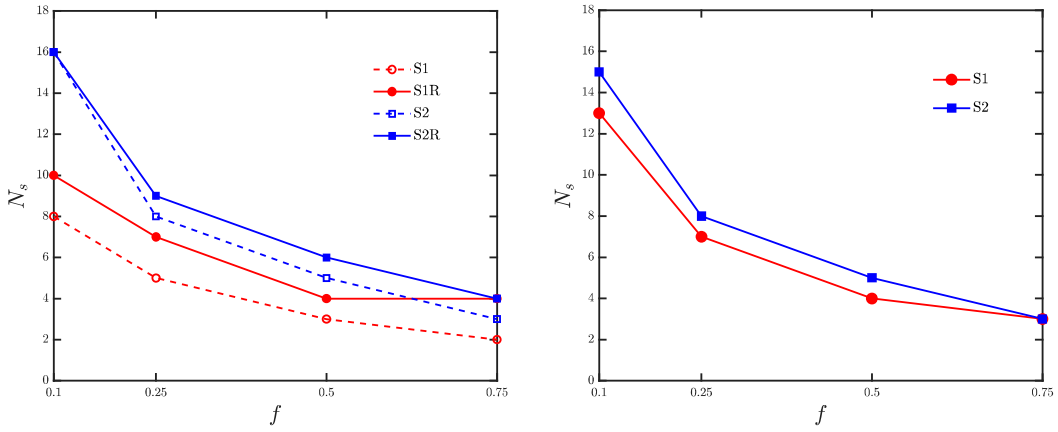

(a) (b)

Figure A.6: Minimum number of patterns required to achieve stabilization N_s for several friction coefficients. (a) Results obtained using the von Mises stress criterion Δ_σ^i and (b) Results obtained using the plastic strain criterion Δ_ϵ^i.

From Figure A.6a it can be seen that in both steps S1 (corrugation) and S2 (straightening), the number of patterns to stabilization using the criterion Δ_σ^i is smaller before stress redistribution compared to after stress redistribution. It means that after stress redistribution, the stabilized section becomes smaller. Also by comparing steps S1 and S2, it is observed that the stabilization zone is always larger during the corrugation stage. It can be explained by the fact that stress distribution during pressing is more sensitive than bending.

The criterion based on the plastic strain (Δ_ϵ^i) leads to a similar result, which is that the transient section is again smaller in corrugation compared to straightening. Moreover, it is interesting to note that the number of patterns required to achieve stabilization is generally lower using the plastic strain criterion Δ_ϵ^i in comparison with the stress criterion Δ_σ^i after stress redistribution: this is actually expected since small variations in plastic strain can lead to important variations in residual stresses.

A.2.3 Kinematic of the patterns

Finally, we study the kinematic of the edges of each pattern of the full multi-pattern model in the x_1-direction. This can guide the development of appropriate boundary conditions that would apply

to the reduced model.

First, we study qualitatively the border region for several patterns in both the stabilized and transient sections, in Figure A.7. Overall, the edges of the stabilized patterns in the full multi-pattern model remain straight and vertical.

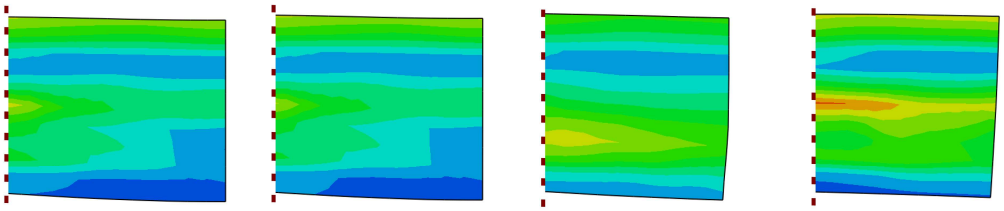

(a) (b) (c) (d)

Figure A.7: The border region for several patterns in stabilized and non-stabilized sections showing the straight vertical boundaries for patterns closer to the center of the workpiece in the case $f = 0.25$. (a) Pattern 1, (b) Pattern 14, (c) Pattern 19 and (d) Pattern 21.

Then we study the displacement of each edge by considering the (accumulated) horizontal displacement of the point P_i located at the top-right corner of the pattern M_i (see Figure A.1), denoted by $u_1(P_i)$ and represented in Figure A.8a. In the stabilized region, this accumulated displacement is linear, which emphasizes that the relative stretching of each pattern is constant when stabilization occurs. In addition, the macroscopic stretching of each pattern, related to the quantity

$$\frac{u_1(P_i) - u_1(P_{i-1})}{L}, \tag{A.5}$$

is represented in Figure A.8b. Interestingly, this quantity reaches very small values in the stabilized region, and is almost constant for a given friction coefficient.

A.3 reduced single-pattern model

The analysis of full multi-pattern model has shown that there exists a stabilization behavior in the workpiece and the mechanical fields in each pattern inside the stabilization zone are asymptotically the same. Furthermore, the minimum number of patterns required to reach stabilization can be important which implies that a full-order model with a large number of patterns is usually necessary to provide accurate results in the stabilized patterns.

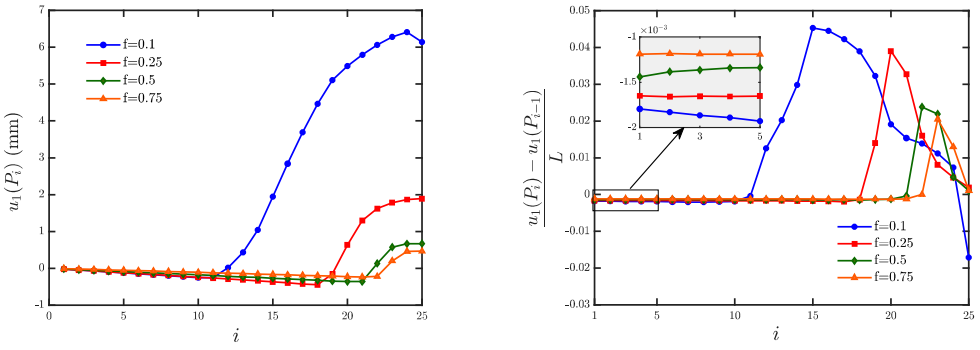

(a) (b)

Figure A.8: Study of the displacement field in the full-order model for different values of the friction. (a) Longitudinal displacement u_1 of the point P_i and (b) Macroscopic stretching of each pattern showing very small values near the center of the sheet.

Based on these observations and the necessity to reduce the computation time, we explore the possibilities to develop a reduced model based on a *single pattern* describing the behavior of the stabilization region, termed as *reduced single-pattern model* (see Figure A.9). To this end, appropriate boundary conditions should be applied to this single pattern so that the model would be able to reproduce both strain and stress distributions of the full multi-pattern model in the stabilized section. In this section, different approximate boundary conditions applied to a single pattern are introduced and the distributions of the mechanical fields are compared with the reference solution of the full multi-pattern (stabilized) model

A.3.1 Description of the approximate boundary conditions considered

Similar to the full multi-pattern model, the reduced single-pattern model is composed of four steps: (S1) corrugation, (S1R) stress redistribution after corrugation, (S2) straightening and (S2R) stress redistribution after straightening. The particularity of the reduced single-pattern model is that the free boundary condition no longer applies and appropriate boundary conditions must be considered, in order to mimic the kinematics of the stabilized patterns of the multi-pattern model. This choice will be crucial because it will considerably affect the distribution of mechanical fields during the process.

Based on the results of Section A.2.3, several boundary conditions may thus be proposed to mimic the kinematic of the patterns in the stabilized section:

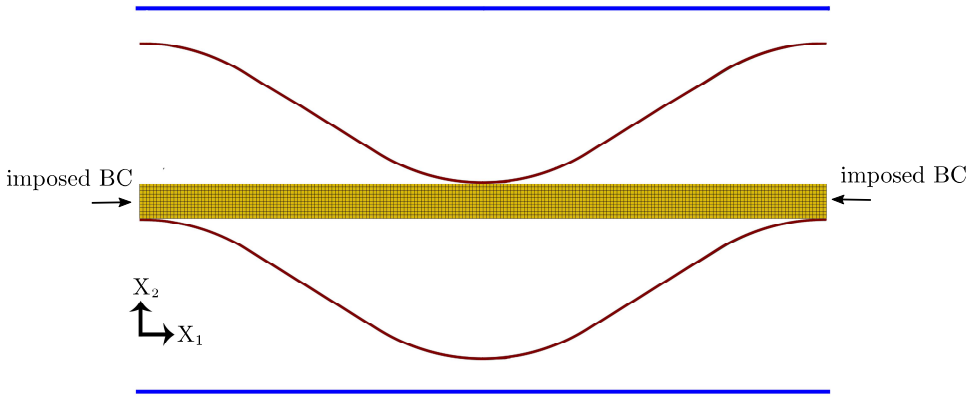

Figure A.9: Finite element model for the reduced single-pattern RCS. Several *imposed BC* at the vertical edges of the workpiece are investigated in order to reproduce at best the stabilized patterns of the full multi-pattern model: symmetric BC, symmetric-free BC and symmetric-periodic BC.

- *Symmetric boundary conditions (model BC-S).* Since the stretching of the stabilized patterns is almost negligible (see Figure A.8), it can be assumed that the lateral edges of the pattern remain fixed in the x_1-direction so that the imposed boundary condition is $u_1(x_1 \pm L/2) = 0$. This condition is imposed for the 4 steps of the process (S1, S1R, S2 and S2R).

- *Symmetric-Free boundary conditions (model BC-SF).* Although the stretching of the stabilized patterns is almost negligible, it can have consequences upon the residual stress. Thus it is proposed to keep the previous symmetric boundary conditions but to split the stress redistribution steps (S1R and S2R) in two new steps S1R-A and S1R-B, S2R-A and S2R-B. The boundary conditions of the first part of the stress redistribution steps (S1R-A and S2R-A) will be symmetric as before but that of the second part (S1R-B and S2R-B) will be free. This should allow more stress redistribution within the pattern.

- *Symmetric-Periodic boundary conditions (model BC-SP).* The previous symmetric-free boundary conditions do not constrain the shape of the pattern edge. However, as shown in Figure A.7, the edges of the stabilized patterns in the full-order model remain straight and vertical. Thus, the second part of the stress redistribution steps in the symmetric-free boundary conditions is modified to enforce the edges to remain straight and vertical, which is termed as *periodic*. In practice, this is achieved by creating a free reference point and restricting the displacement u_1 of all the edge nodes to this reference point, using an equation interaction in Abaqus.

A summary of the three cases considered is given in Table A.1. Each case defines an approximate reduced model, whose relevance will be studied by comparison with the results of the full multi-pattern model.

Table A.1: Summary of the boundary conditions considered in the reduced-order model.

	Corrugation			Straightening		
	S1	S1R-A	S1R-B	S2	S2R-A	S2R-B
BC-S	Symmetric	Symmetric	–	Symmetric	Symmetric	–
BC-SF	Symmetric	Symmetric	Free	Symmetric	Symmetric	Free
BC-SP	Symmetric	Symmetric	Periodic	Symmetric	Symmetric	Periodic

A.3.2 Comparison of the boundary conditions

Preliminary comparisons between the three reduced single-pattern models (BC-S, BC-SF and BC-SP) and the stabilized patterns of the full multi-pattern model are performed in the case $f = 0.25$.

First, the distribution of the longitudinal stress σ_{11} is represented in Figure A.10 at the end of step S2 (before stress redistribution), for the full multi-pattern and the reduced single-pattern models. In that case the three boundary conditions considered for the reduced single-pattern model (BC-S, BC-SF and BC-SP) give very similar results. This behavior is expected since before stress redistribution the stress is unrelaxed so the stress level is mainly related to the loading and the present boundary conditions which are the same at this step in the three cases considered; the only differences that occur between them are related to the stress redistribution step in step S1R which is treated differently. But since the level of residual stresses after corrugation is moderate, those residual stresses have only a little contribution to the stress level at step S2.

The distribution of the longitudinal stress σ_{11} is then represented in Figure A.11 at the end of step S2R (after stress redistribution), for the full multi-pattern and the reduced single-pattern models. This shows that symmetric boundary conditions (BC-S), which was suitable before stress redistribution, fail to correctly represent the stress redistribution behavior of the material (Figure A.11b). From this figure, it seems that the stress in the specimen is not 'redistributed enough' as the stress level is still influenced by the loading step and in general there is more compressive stress in comparison with the reference full multi-pattern solution. The symmetric-free stress redistribution model (BC-SF) improves the distribution of the von Mises stress (Figure A.11c), but there are still some locations,

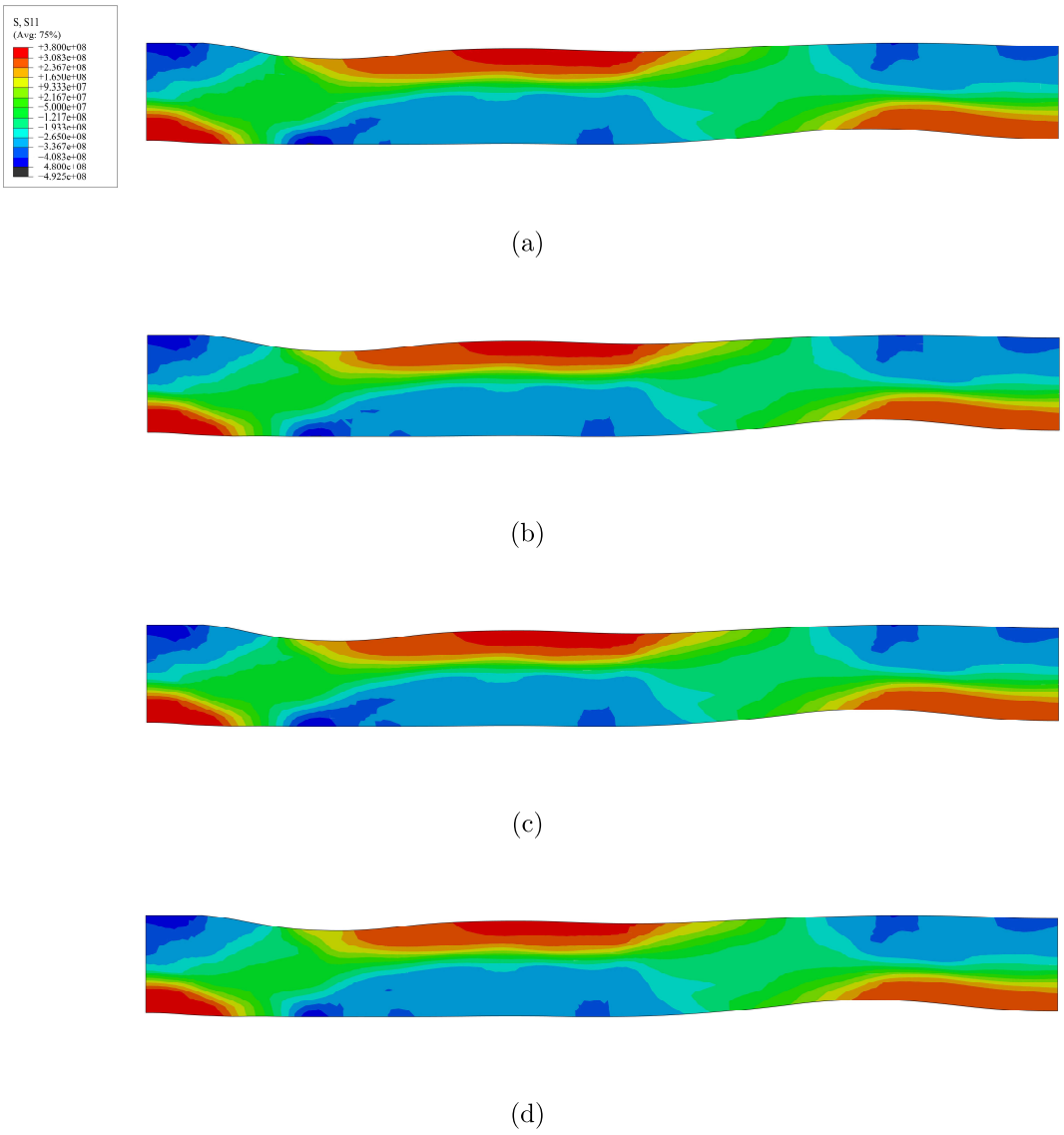

Figure A.10: Distribution of the longitudinal stress σ_{11} at the end of step S2 (before stress redistribution). (a) full multi-pattern model (extracted from pattern M_1), (b) Reduced single-pattern model BC-S (symmetric boundary conditions), (c) Reduced single-pattern model BC-SF (symmetric-free boundary conditions) and (d) Reduced single-pattern BC-SP (symmetric-periodic boundary conditions).

notably near the edges, where the stress is not very well represented by the reduced single-pattern model. Finally, the symmetric-periodic model (BC-SP) improves significantly the predictions as it provides the more accurate distribution of stress (Figure A.11d).

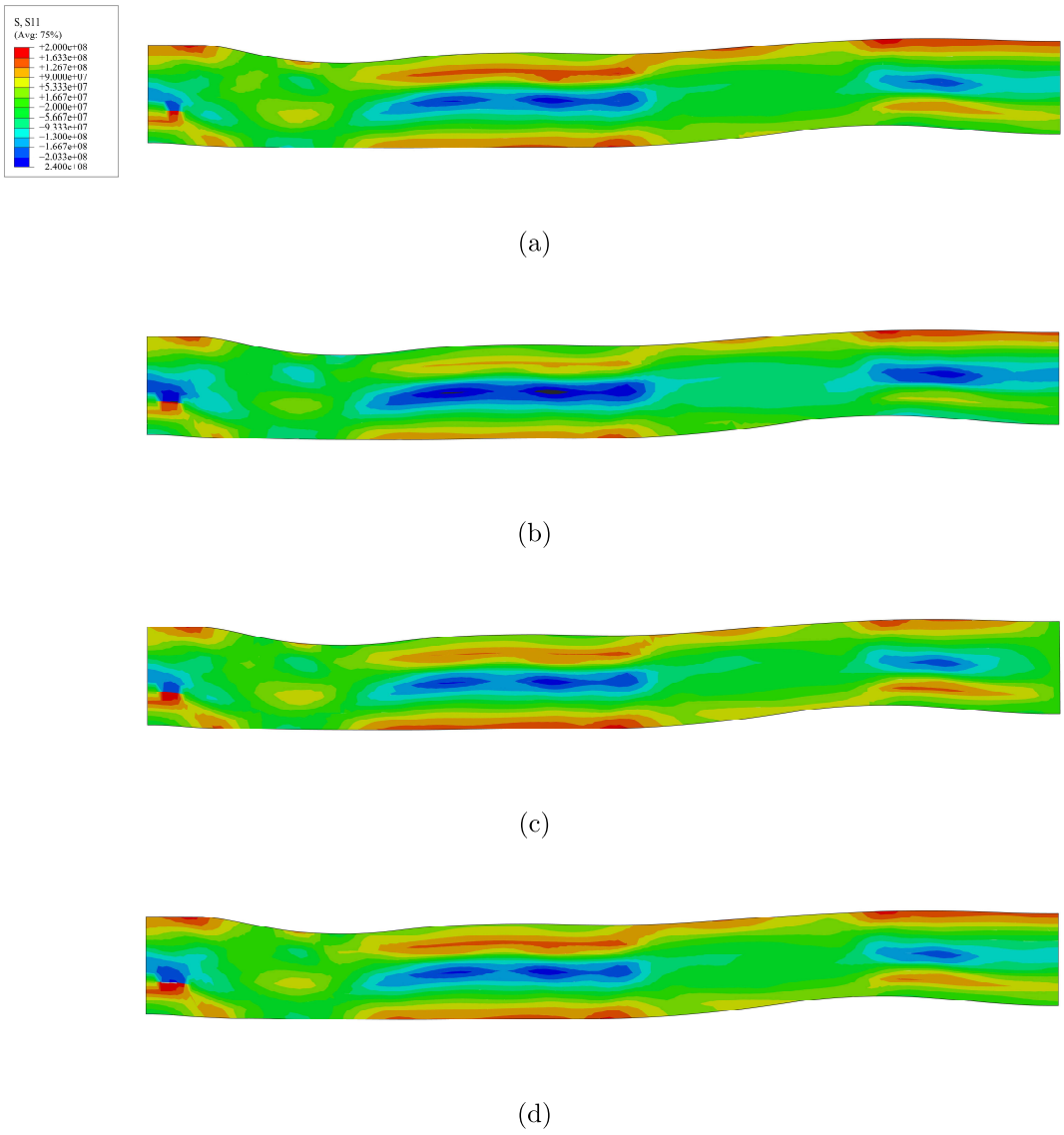

Figure A.11: Distribution of the longitudinal stress σ_{11} at the end of step S2R (after stress redistribution). (a) full multi-pattern model (extracted from pattern M_1), (b) Reduced single-pattern model BC-S (symmetric boundary conditions), (c) Reduced single-pattern model BC-SF (symmetric-free boundary conditions) and (d) Reduced single-pattern BC-SP (symmetric-periodic boundary conditions).

A.3.3 Assessment of the reduced single-pattern model

To further analyze the reduced single-pattern model and to quantify its ability to reproduce the full multi-pattern model, normalized local difference criteria between a pattern in the stabilized section of the full multi-pattern model and the reduced single-pattern model, defined from the equivalent von

Mises stress (denoted by Δ_σ^{RM}) or the accumulated plastic strain (denoted by Δ_ϵ^{RM}), are introduced:

$$\Delta_\sigma^{RM} = \frac{\langle|\sigma_{eq}^{RM} - \sigma_{eq}^{FM}|\rangle_{\Omega_0}}{\langle\sigma_{eq}^{FM}\rangle_{\Omega_0}} \quad , \quad \Delta_\epsilon^{RM} = \frac{\langle|p_{eq}^{RM} - p_{eq}^{FM}|\rangle_{\Omega_0}}{\langle p_{eq}^{FM}\rangle_{\Omega_0}}. \tag{A.6}$$

In equation (A.6), σ_{eq}^{RM} and p_{eq}^{RM} are respectively the equivalent von Mises stress and accumulated plastic strain in the reduced single-pattern model, while σ_{eq}^{FM} and p_{eq}^{FM} are respectively the equivalent von Mises stress and accumulated plastic strain in the first pattern (M_1) of the full multi-pattern model. As explained in Section A.2.2, the volume average (given by equation (A.3)) is taken on the initial configuration in order to avoid the fluctuations due to geometrical changes. These two criteria will permit to assess quantitatively the influence of the boundary conditions considered in the three reduced models.

Several simulations are performed for the three sets of boundary conditions introduced previously (BC-S, BC-SF and BC-SP) using four different friction coefficients. The stress-based criterion Δ_σ^{RM} is provided in Figure A.12 at the end of steps S1R (relaxed after corrugation) and S2R (relaxed after straightening). Irrespective of the boundary condition considered, the criterion Δ_σ^{RM} increases after S2R which is expected since the modelling errors accumulate from step S1R to S2R. In both steps, the criterion Δ_σ^{RM} is lower using BC-SF and BC-SP in comparison with BC-S, which implies that the stress redistribution brought by an extra sub-step improves significantly the results. A maximal error of 26% was found with the symmetric boundary conditions (BC-S), 12.5% with the symmetric-free boundary conditions (BC-SF), and finally 7% with the symmetric-periodic boundary conditions (BC-SP). Furthermore, the lowest values for the criterion Δ_σ^{RM} are always achieved by the symmetric-periodic model (for all values of the friction coefficient) emphasizing that these approximate boundary conditions are the most suitable to reproduce the distribution of residual stresses obtained in the full multi-pattern model. At the end of the process, the relative error using the symmetric-periodic boundary conditions is always below 7%.

In addition, the results obtained from the strain-based criterion Δ_ϵ^{RM} are provided in Figure A.13. For this criterion, the three boundary conditions give almost the same predictions since the accumulated plastic strain is not modified during stress redistribution. Again the error is higher after step S2. The comparison between the stress-based and strain-based criteria shows that the equivalent plastic strain is always more stable as Δ_ϵ^{RM} is lower than Δ_σ^{RM}, which is expected because residual stresses are more sensitive than plastic strain.

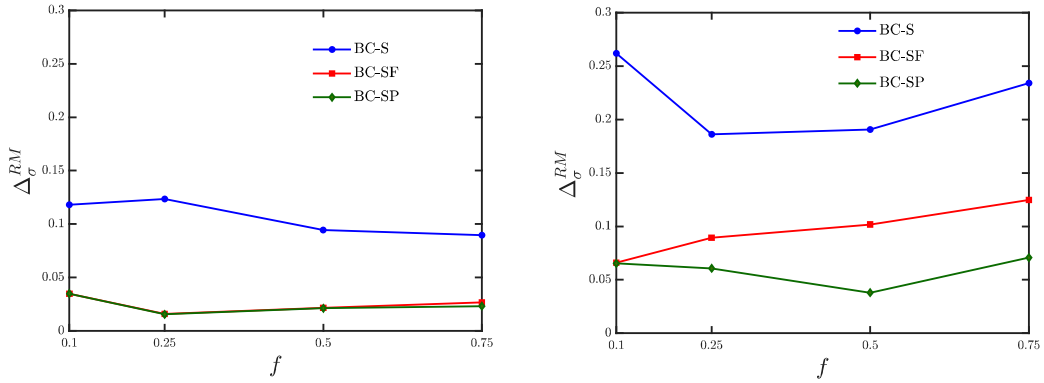

(a) (b)

Figure A.12: Assessment of the reduced single-pattern model using the stress-based normalized criterion Δ_σ^{RM}. (a) At the end of step S1R (relaxed after corrugation) and (b) At the end of step S2R (relaxed after straightening).

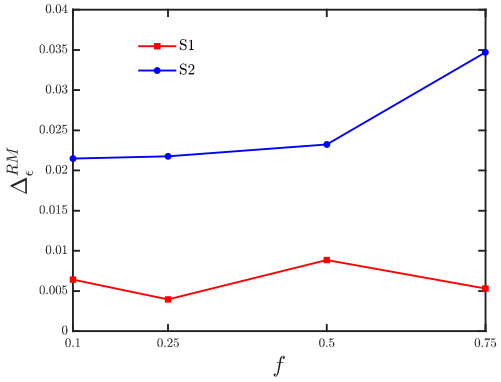

Figure A.13: Assessment of the reduced single-pattern model using the strain-based normalized criterion Δ_ϵ^{RM} as a function of the friction coefficient for both S1 and S2 steps.

A.4 Stability analysis of RCS in 2 direction model

Assessment of the distribution of stress and strain field in RCS process showed the presence of stabilization with respect to the motifs of corrugation die. Moreover, It was established that the stabilization behavior is a function of the friction coefficient. In the case examined in this work, a case of RCS process with repetition of motifs of corrugation die in one direction was analysed. However, other types of RCS process with different motif shapes also exist in literature. Particularly, RCS

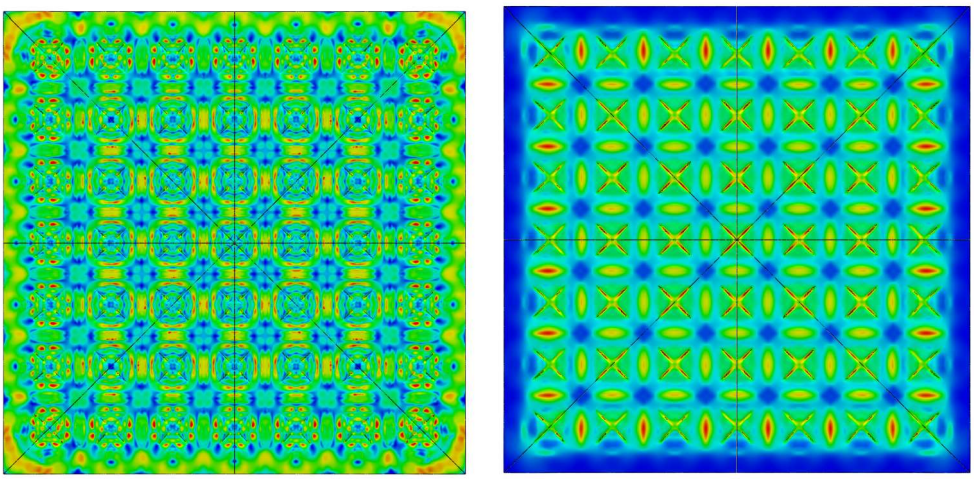

(a) (b)

Figure A.14: Distribution of (a) accumulated plastic strain $PEEQ$ and (b) residual stress σ_{res} after 1 pass of RCS process using multi-pattern model.

process with 3D motifs repeated in 2-directions are used in experiments (see Figure 3.1). In this thesis, we have used this type of RCS process; hence, it is necessary verify the stabilization behavior for RCS process with motifs repited in 2 directions.

Consequently, first the 7x7 multi-motif numerical model of RCS according to the experimental procedure performed in this thesis was created. This model is similar with the one explained in chapter 3 but instead of only one motif, 49 motifs (7 rows and 7 columns) were considered. Use was made of the symmetrical nature of the RCS process and only $1/8^{th}$ of the whole model was created. The 3D model was meshed with C3D8R elements and a mesh size of $0.2mm$ was applied. Friction coefficient $f = 0.25$ was used in the simulations, which is representative of a not lubricated steel-aluminum contact and the same value was also used for RCS simulations in chapter 3. Using 24 Intel Xeon Gold 5220R (2,2GHz) CPUs, the simulations took 16 hours. A distribution of accumulated plastic strain p_{eq} and von Mises equivalent stress σ_{eq} at the end of simulations is given in Figure A.14. Interestingly, we can see the appearance of stabilization zones in both cases, similar to the case of RCS in 1 direction.

Next, the reduced single-pattern numerical of RCS in 2 direction was created to see if the results are consistent with the motifs in the stabilized zone of the multi-pattern model. This numerical model is the same as the one explained in section 3.5 of chapter 3 but the mesh size is similar with

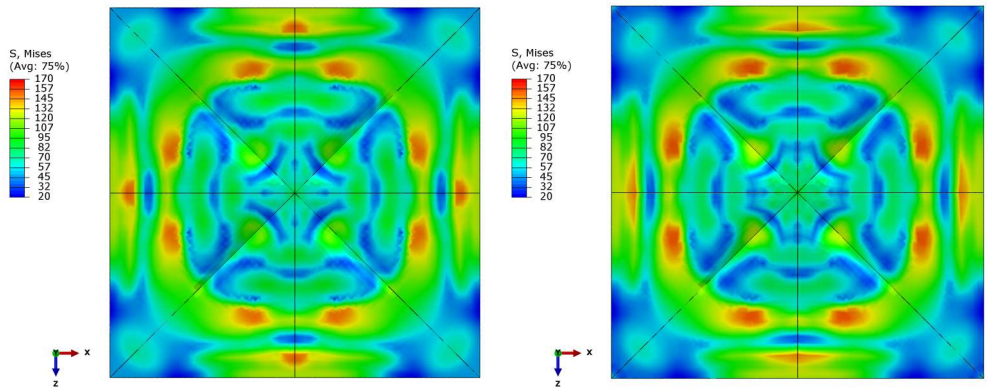

(a) (b)

Figure A.15: Distribution of residual stress σ_{res} after 1 pass of RCS process. The simulation results belong to (a) The central pattern of the multi-pattern model and (b) the reduced single-pattern model (the values are in MPa).

the multi-motif model. According to results of the reduced single-pattern for RCS in 1 direction, symmetric-periodic boundary conditions were applied to this model. The results obtained from the simulation of single-pattern RCS is prestend in Figures A.15 and A.16. In Figure A.15, the distribution of stress in single-pattern model is compared to the motif in the center of multi-pattern model at the end of calculation. Similarly in Figure A.16, the distribution of accumulated plastic strain is compared between the single- and multi-pattern models. The results show great similarity between the two models and shows that the reduced single-pattern model with symmetric-periodic boundary conditions was successfully able to reproduce the results of the stabilized patterns of multi-pattern model.

Furthermore, only using 12 CPUs, the simulation took about 7 minutes to finish (compared with 16 hours for multi-pattern model). These results show that the calculation time was hugely reduced using the reduced single-pattern model in 2 direction RCS (about 140 times). This proves the importance of model reduction in simulation of multi-pattern processing.

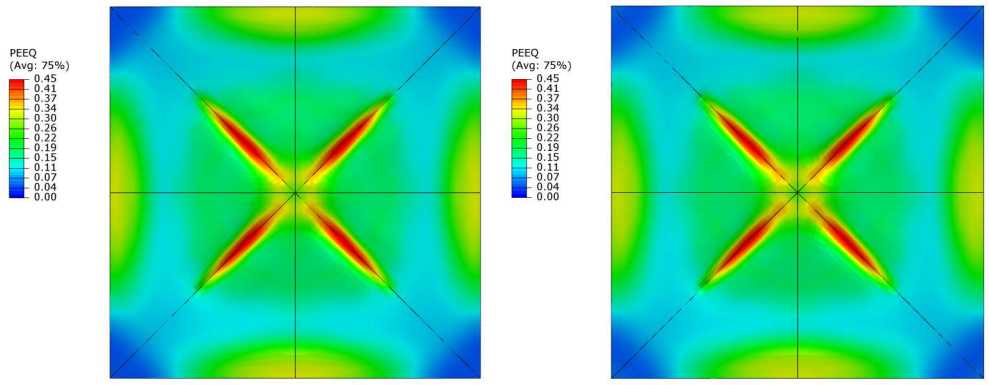

(a) (b)

Figure A.16: Distribution of accumulated plastic strain $PEEQ$ after 1 pass of RCS process. The simulation results belong to (a) The central pattern of the multi-pattern model and (b) the reduced single-pattern model.

Appendix B

Deconvolution of X-ray diffraction measurements

B.1 Introduction

The durability of structural components is considerably influenced by residual stresses. The understanding of residual stresses and their determination are thus necessary during the design and manufacturing of products [126, 128], as undesirable tensile residual stresses can decrease fatigue life and corrosion resistance [89]. The origin of residual stresses is the presence of an incompatible strain field, which can be due to heterogeneous plastic deformation or phase transition. Compressive residual stresses can thus be introduced on purposes to improve durability, using for instance shot peening [77] or laser shock peening [96]. Uncontrolled residual stresses can be introduced unintentionally in most manufacturing processes based on plastic deformation or heat treament, such as in machining [9], welding [69], severe plastic deformation [35] and additive manufacturing [36], among other. The assessment of residual stress distributions is thus of paramount importance for the durability and reliability of engineering components.

X-ray diffraction (XRD) is a high accuracy and non-destructive method to measure residual stresses in crystalline materials [102]. It is based on the measurement of the shift of the Bragg angle which allows the calculation of the change in interatomic lattice spacing, leading to an estimation of the strain in a small volume under the specimen surface; crystalline planes are thus used as strain gauges [72]. Residual stresses can then be deduced from the elastic theory provided that the X-ray elastic constants are known. In metallic alloys, this method allows measurements in outer layers due to the important

absorption of X-ray. Hence, it is generally used to determine (destructively) stress gradients in depth with a very good precision using successive polishing. Alternatively, multi-reflection grazing-incidence techniques allow the determination of depth-dependent stress profiles non-destructively [3, 79].

Nonetheless, an important drawback of X-ray diffraction is the inherent averaging effects of the method which can lead to inaccurate measurement results in the presence of high surface stress gradients [52, 57, 58, 82]. Indeed, X-ray diffraction measurements provide the average lattice strain within the irradiated area, whose size depends on the collimator. Therefore, when the characteristic length of the surface strain gradient is smaller than the irradiated area, the corresponding stresses obtained from XRD is an average of the local heterogeneous stresses. The averaging effect can be decreased by using a small irradiated area, but since the diffracting volume has to contain a sufficient number of crystallites to be statistically representative, it cannot be reduced below some critical value in typical engineering materials containing micron-sized crystallites. Consequently, important averaging effects on the residual stresses measured by XRD are expected in the presence of high lateral stress gradients.

Recently, Morin et al. [82] proposed a method to reconstruct spatially the local residual stress field using several X-ray diffraction measurements performed on a regular grid (e.g. using an automatic robot) and with the use of two collimator sizes (inducing two different irradiated areas). Since the average stress obtained from XRD corresponds to the convolution of the local stress, a linear relationship between the point-wise values of the (unknown) local stress field and that of the average stress determined experimentally can be constructed. The inversion of this linear system leads to the so-called *deconvolution* of the residual stress field. The use of a fine measurement grid together with two datasets for the averages make the linear system overdetermined which improves the reconstruction. Their method has been successfully applied to the reconstruction of line stress profiles in a specimen processed by repetitive corrugation and straightening.

The method developed by Morin et al. [82] was based on several hypotheses, the most restrictive one being that the lateral stress-gradient are supposed to occur in only one direction. Hence, this method restricted by essence to the reconstruction of stress line profiles. Next, a modification of this method is proposed for 2D reconstruction heterogeneous residual stress mapping obtained by X-ray diffraction.

B.2 Averaging effects of X-ray diffraction measurements

The components of the stress tensor that are obtained from XRD measurements result from a convolution of the local stress tensor components over the *irradiated area*[1]. This area is generally of circular or rectangle shape in practical laboratory facilities. In the following, we will make several assumptions which will allow the derivation of a deconvolution method that can be used for practical applications: (i) the irradiated area is square-shaped and (ii) the averaging over the irradiated area is uniform (penumbra effects are disregarded).

Therefore, X-ray diffraction is assumed to consist in the (homogeneous) convolution of the local stress over the irradiated square-shape area, which corresponds to a 2D moving average. Let us consider one component of the stress tensor, or a linear combination of several components (since the convolution applies to each component separately), which is denoted by $\sigma(x, y)$ for convenience, where x and y denotes the spatial coordinates. If the size of irradiated area is denoted by $2a \times 2a$, the moving average $\Sigma^a(x, y)$ of the stress σ is then given by the formula

$$\Sigma^a(x, y) = \frac{1}{4a^2} \int_{x-a}^{x+a} \int_{y-a}^{y+a} \sigma(x_1, x_2) \mathrm{d}x_1 \mathrm{d}x_2. \tag{B.1}$$

The problem we are addressing is the reconstruction of the local stress field $\sigma(x, y)$ in a 2D domain from the knowledge of its average $\Sigma^a(x, y)$.

B.3 Principles of 2D residual stress mapping reconstruction

The 2D domain considered is a square domain of size $[0, L] \times [0, L]$. The determination of residual stress mapping requires the measurement of the moving average $\Sigma(x, y)$ on a regular grid (see Figure B.1); the domain $[0, L] \times [0, L]$ is discretized onto a uniform grid with spatial scale $\Delta x = \Delta y = L/(N-1)$, where the total number of points is $N \times N$. We use the following notation: $x_i = (i-1)\Delta x$, $y_j = (j-1)\Delta x$, $\sigma_{ij} = \sigma(x_i, y_j)$, with $i = 1, ..., N$ and $j = 1, ..., N$. We denote by $\boldsymbol{\sigma}$ the $N \times N$ matrix that contains the values σ_{ij}.

For simplicity, we assume that the half-width of the irradiated zone is of the form

$$a = k_a \Delta x, \tag{B.2}$$

[1]The effect of in-depth gradients is often negligible in XRD measurements due to the absorption of X-ray in metallic alloys.

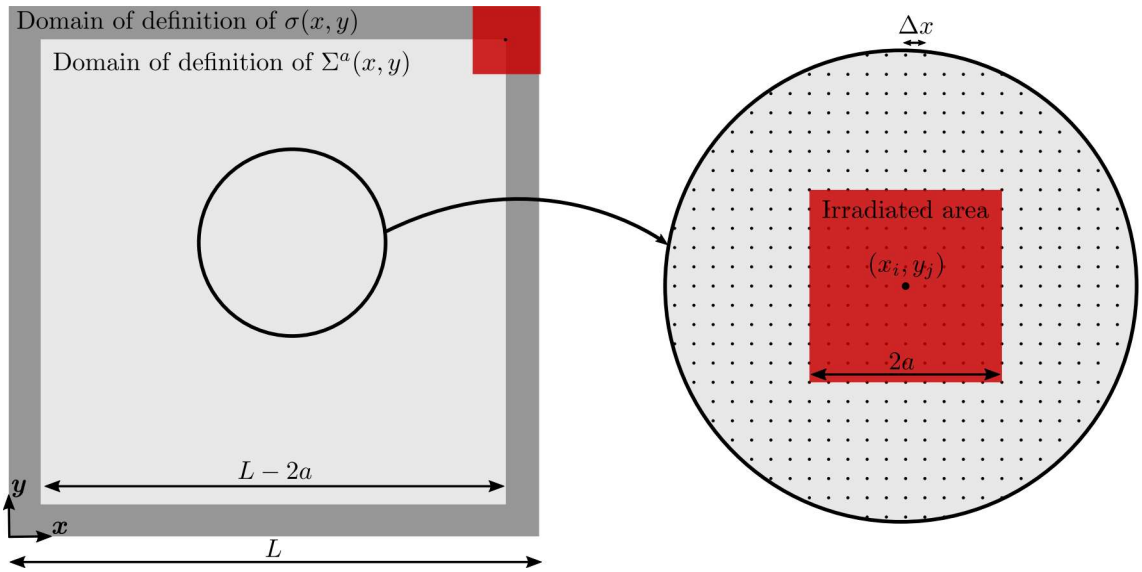

Figure B.1: Description of the geometry considered for 2D XRD mapping with a square irradiated area.

where k_a is a positive integer. From the definition of the moving average $\Sigma^a(x,y)$, it is readily seen that it is only defined in the domain $[a, L-a] \times [a, L-a]$. Therefore, on the discretized grid, it reads $\Sigma^a_{ij} = \Sigma^a(x_i, y_j)$ with $i = k_a + 1, ..., N - k_a$. The matrix $\mathbf{\Sigma}^a$ which contains these values is thus of size $(N - 2k_a) \times (N - 2k_a)$.

Then, the integral defined by equation (B.1) is approximately calculated using a trapezoidal rule:

$$\begin{aligned}\Sigma^a_{ij} =& \frac{1}{16k_a^2}\left(\sigma_{i-k_a,j-k_a} + \sigma_{i-k_a,j+k_a} + \sigma_{i+k_a,j-k_a} + \sigma_{i+k_a,j+k_a}\right) \\ &+ \frac{1}{8k_a^2}\left(\sum_{l=i-k_a+1}^{i+k_a-1}\left(\sigma_{l,j-k_a} + \sigma_{l,j+k_a}\right) + \sum_{m=j-k_a+1}^{j+k_a-1}\left(\sigma_{i-k_a,m} + \sigma_{i+k_a,m}\right)\right) \\ &+ \frac{1}{4k_a^2}\sum_{l=i-k_a+1}^{i+k_a-1}\sum_{m=j-k_a+1}^{j+k_a-1}\sigma_{lm}. \end{aligned} \tag{B.3}$$

In order to establish a linear relation between $\mathbf{\Sigma}^a$ and $\boldsymbol{\sigma}$, we introduce a vector representation of these matrices, respectively denoted by $\widehat{\mathbf{\Sigma}}^a$ and $\widehat{\boldsymbol{\sigma}}$ and defined as

$$\widehat{\sigma}_{(i-1)N+j} = \sigma_{ij}, \quad \forall i = 1, ..., N \quad \text{and} \quad j = 1, ..., N, \tag{B.4}$$

$$\widehat{\Sigma}^a_{(i-1)(N-k_a)+j} = \Sigma^a_{ij}, \quad \forall i = 1, ..., N - 2k_a \quad \text{and} \quad j = 1, ..., N - 2k_a. \tag{B.5}$$

Using this vector representation, the linear relation between $\mathbf{\Sigma}^a$ and $\boldsymbol{\sigma}$, defined by equation (B.3), reads

$$\widehat{\mathbf{\Sigma}}^a = \mathbf{R}^a \cdot \widehat{\boldsymbol{\sigma}} \tag{B.6}$$

where $\mathbf{R}^a$ is a matrix of size $(N-2k_a)^2 \times N^2$ which can be constructed from equation (B.3). For illustrative purposes, the non-zero components of the line number $(i-1)(N-k_a)+j$ of $\mathbf{R}^a$, associated with the calculation of the average Σ^a_{ij}, are given by

$$R_{(i-1)(N-k_a)+j,l} = \begin{cases} \dfrac{1}{16{k_a}^2} & \text{if } \; l = (i \pm k_a - 1)(N-k_a) + j \pm k_a \\ \dfrac{1}{8{k_a}^2} & \text{if } \; l = \begin{cases} mN + j \pm k_a \\ (i \pm k_a - 1)(N-k_a) + n \end{cases} \\ \dfrac{1}{4{k_a}^2} & \text{if } \; l = mN + n \\ 0 & \text{otherwise,} \end{cases} \tag{B.7}$$

where m and n take the values

$$m = i - k_a + 1, ..., i + k_a - 1, \qquad n = j - k_a + 1, ..., j + k_a - 1. \tag{B.8}$$

The linear system defined by equation (B.6) is underdetermined because there are fewer equations ($(N-2k_a)^2$) than unknowns (N^2); the rank of $\mathbf{R}^a$ is necessarily lower than N^2. Therefore, only an approximate solution of the system can be found, for instance by minimizing the residual sum-of-square. In that case the solution of the minimization problem leads to

$$\widehat{\boldsymbol{\sigma}} = (\mathbf{R}^a)^+ \cdot \widehat{\mathbf{\Sigma}}^a, \tag{B.9}$$

where $(\mathbf{R}^a)^+$ is the classical Moore-Penrose right pseudoinverse matrix of $\mathbf{R}^a$ defined as

$$(\mathbf{R}^a)^+ = (\mathbf{R}^a)^T \cdot \left(\mathbf{R}^a \cdot (\mathbf{R}^a)^T\right)^{-1}. \tag{B.10}$$

B.4 Improvements of the method

As explained in [82], the reconstructed stress field $\widehat{\boldsymbol{\sigma}}$ provided by equation (B.9) is expected to be inaccurate due to the underdetermined nature of the system as well as the presence of experimental noise on $\mathbf{\Sigma}^a$. In order to improve the prediction of the residual stress field, it is proposed to (i) construct a smooth estimate $\widetilde{\mathbf{\Sigma}}^a$ and (ii) use several sets of measurements with different collimators (inducing different diffraction areas).

First, the smooth estimate $\widetilde{\mathbf{\Sigma}}^a$ is constructed using the robust spline-based smoother developed by Garcia [38], based on the minimization of a functionnal that balances the fidelity to the data, through the residual sum-of-squares (RSS), and the smoothness of the estimate through a penalty term (that depends on the second derivative of the function). The advantage of this approach is that the smooth estimate is unique using the classical method of generalized cross-validation (GCV) which provides the best smoothing parameter avoiding over- or under-smoothing.

Then, several sets of measurements using different collimators are considered. This permits to increase the number of equations involved in the linear system and ultimately this will improve the accuracy of the reconstructed residual stress field. For illustrative purposes, we consider two sets of measures associated with two collimators but the extension to an arbitrary number of sets ($n \geq 2$) is straightforward. The irradiated areas have respectively a width denoted by $2a_1 = 2k_1\Delta x$ and $2a_2 = 2k_2\Delta x$, and the associated moving averages $\Sigma^{a_i}(x, y)$ of the stress σ are then given by the formula

$$\Sigma^{a_i}(x, y) = \frac{1}{4a_i^2} \int_{x-a_i}^{x+a_i} \int_{y-a_i}^{y+a_i} \sigma(x_1, x_2) \mathrm{d}x_1 \mathrm{d}x_2, \quad i = [1, 2]. \tag{B.11}$$

After smoothing, this leads to the linear relations

$$\widehat{\widetilde{\mathbf{\Sigma}}}^{a_1} = \mathbf{R}^{a_1} \cdot \widehat{\boldsymbol{\sigma}}, \quad \widehat{\widetilde{\mathbf{\Sigma}}}^{a_2} = \mathbf{R}^{a_2} \cdot \widehat{\boldsymbol{\sigma}}, \tag{B.12}$$

where the matrices $\mathbf{R}^{a_1}$ and $\mathbf{R}^{a_2}$ are constructed using (B.7). We denote by $\widehat{\widetilde{\mathbf{\Sigma}}}$ the vector (of length $((N - 2k_{a_1})^2 + (N - 2k_{a_2})^2)$ which concatenates the vectors $\widehat{\widetilde{\mathbf{\Sigma}}}^{a_1}$ and $\widehat{\widetilde{\mathbf{\Sigma}}}^{a_2}$, and by $\mathbf{R}$ the matrix (of size $[(N - 2k_{a_1})^2 + (N - 2k_{a_2})^2] \times N^2$) which concatenates the matrices $\mathbf{R}^{a_1}$ and $\mathbf{R}^{a_2}$:

$$\widehat{\widetilde{\mathbf{\Sigma}}} = \begin{bmatrix} \widehat{\widetilde{\mathbf{\Sigma}}}^{a_1} \\ \widehat{\widetilde{\mathbf{\Sigma}}}^{a_2} \end{bmatrix}, \quad \mathbf{R} = \begin{bmatrix} \mathbf{R}^{a_1} \\ \mathbf{R}^{a_2} \end{bmatrix}. \tag{B.13}$$

Using equations (B.12) and (B.13), the linear system constructed from the two sets of measurements simply reads

$$\widehat{\widetilde{\mathbf{\Sigma}}} = \mathbf{R} \cdot \widehat{\boldsymbol{\sigma}}. \tag{B.14}$$

Two cases need to be distinguished to find the solution $\widehat{\boldsymbol{\sigma}}$:

- If the system is underdetermined (i.e. the rank of $\mathbf{R}$ is lower than N^2), the approximate solution is given, as in Section B.3, by

$$\widehat{\boldsymbol{\sigma}} = \mathbf{R}^+ \cdot \widehat{\widetilde{\mathbf{\Sigma}}}, \tag{B.15}$$

where $\mathbf{R}^+$ is the classical Moore-Penrose right pseudoinverse matrix of $\mathbf{R}$ defined as

$$\mathbf{R}^+ = \mathbf{R}^T \left(\mathbf{R}\mathbf{R}^T\right)^{-1}. \tag{B.16}$$

- If the system is overdetermined (i.e. the rank of $\mathbf{R}$ is equal to N^2), the approximate solution is given by

$$\widehat{\boldsymbol{\sigma}} = \mathbf{R}^+ \cdot \widehat{\widehat{\boldsymbol{\Sigma}}}, \tag{B.17}$$

where $\mathbf{R}^+$ is the classical Moore-Penrose left pseudoinverse matrix of $\mathbf{R}$ defined as

$$\mathbf{R}^+ = \left(\mathbf{R}^T\mathbf{R}\right)^{-1} \mathbf{R}^T. \tag{B.18}$$

In practice the pseudo-inverse $\mathbf{R}^+$ is calculated numerically using efficient algorithms based on using its singular-value decomposition (SVD). In both cases (underdetermined or overdetermined system), the method will provide a unique reconstructed stress field from several sets of measurements.

Appendix C

Principles of XRD measurements for a fast mapping of the bi-axial surface stress

The principles of XRD measurements is to determine the interatomic spacing d of a family of diffracting planes using Bragg's law. If we denote by d_0 the free-stress interatomic lattice spacing, the strain is given by

$$\varepsilon_{\Phi\Psi} = \frac{d_{\Phi\Psi} - d_0}{d_0}, \tag{C.1}$$

where Φ and Ψ are the angles associated with the X-ray direction. In the case of an isotropic elastic material, it is straightforward to note that

$$\begin{aligned}\varepsilon_{\Phi\Psi} = &\frac{1+\nu}{E}\left(\sigma_{11}\cos^2(\Phi) + \sigma_{12}\sin(2\Phi) + \sigma_{22}\sin^2(\Phi) - \sigma_{33}\right)\sin^2(\Psi)\\ &+ \frac{1+\nu}{E}\sigma_{33} - \frac{\nu}{E}\left(\sigma_{11} + \sigma_{22} + \sigma_{33}\right)\\ &+ \frac{1+\nu}{E}\left(\sigma_{13}\cos(\Phi) + \sigma_{23}\sin(\Phi)\right)\sin(2\Psi).\end{aligned} \tag{C.2}$$

In the particular case $\Phi = 0°$ and $\Psi = 0°$, we have $\varepsilon_{\Phi=0°,\Psi=0°} = \varepsilon_{33}$, and therefore it is readily seen from equation (C.2) that

$$\varepsilon_{33} = \varepsilon_{\Phi=0°,\Psi=0°} = -\frac{\nu}{E}\left(\sigma_{11} + \sigma_{22}\right) + \frac{\sigma_{33}}{E}. \tag{C.3}$$

Since the XRD measurements are performed on the surface of normal $\boldsymbol{e}_3$, the normal stress σ_{33} is null. Using equations (C.1) and (C.3), the bi-axial stress σ_h finally reads

$$\sigma_h = \sigma_{11} + \sigma_{22} = -\frac{E}{\nu}\frac{d_{\Phi=0°,\Psi=0°} - d_0}{d_0}. \tag{C.4}$$

Consequently the determination of the interatomic spacing $d_{\Phi=0^\circ,\Psi=0^\circ}$ allows a fast mapping of the bi-axial stress σ_h since only one X-ray direction is required (with $\Phi = \Psi = 0^\circ$). In practice, the free-stress interatomic lattice spacing d_0 is also required; it is determined in several points of the specimen (by calculating the full stress tensor using for instance 13 angles Ψ).

Arts et Métiers Sciences et Technologies

Pouya TAJDARY

Numerical simulation of damage in nanostructured materials obtained by severe plastic deformation

HESAM UNIVERSITÉ

Résumé : Les matériaux nanostructurés obtenus notamment par déformation plastique sévère (SPD) constituent une classe émergente de matériaux avancés qui offrent de nouvelles possibilités en termes de propriétés fonctionnelles et structurelles en combinant résistance et ductilité élevées. La simulation du processus SPD est assez difficile car cela implique des déformations plastiques importantes et des non-linéarités liées aux conditions de contact. En plus, de nombreux modèles d'endommagement physiques et phénoménologiques ont été développés mais aucun n'a été implémenté dans un cas sévère tel que les processus SPD. Dans cette thèse, nous essayons d'implémenter des modèles microstructuraux récents basés sur l'évolution de densités de dislocations dans les processus SPD et en implémentant des lois d'évolution de l'endommagement pendant la simulation de ces processus. Un cadre de calcul sera développé afin de prédire l'évolution de la microstructure et de l'endommagement pendant les procédés SPD. Cela permet d'améliorer la compréhension du compromis résistance-ductilité dans les procédés SPD et d'optimiser les conditions de traitement afin de minimiser l'endommagement et d'améliorer les propriétés du matériau traité.

Mots clés : Déformation plastique sévère, Endommagement ductile, Modélisation numérique, Densité des dislocations

Abstract : Nanostructured materials obtained notably through severe plastic deformation (SPD) are an emerging class of advanced materials that bring new possibilities in terms of functional and structural properties by combining high strength and ductility. Simulation of SPD process is quite challenging as it involves excessive plastic deformation and nonlinearity due to contact conditions. Additionally, many physical and phenomenological damage models have been developed but none have been implemented in a severe case such of SPD processes. In this thesis, we try to implement recent microstructural models based on dislocation density evolution in SPD processes and by implementing damage evolution laws during the simulation of these processes. A computational framework will be developed in order to predict the evolution of microstructure and damage during SPD. This permits to improve the understanding of strength-ductility trade-off in SPD and optimize the processing conditions in order to minimize the damage and enhance the properties of the processed material.

Keywords : Severe Plastic Deformation, Ductile damage, Numerical Modeling, Dislocation density